Numerical modelling of stellar winds for supernova progenitors

Stefanus Petrus van den Heever, BSc (Hons.)

Numerical modelling of stellar winds for supernova progenitors

Stefanus Petrus van den Heever, BSc (Hons.)

Dissertation submitted in partial fulfilment of the requirements for the degree Master of Science in Physics at the Potchefstroom Campus of the North-West University

Supervisor: Prof. S. E. S. Ferreira

Potchefstroom

March 2011

South Africa

If we knew what it was we were doing, it would not be called research, would it?
- Albert Einstein

To Elré - My fiancée, companion and friend.

Abstract

A two-dimensional hydrodynamic numerical model is extended and applied to simulate the interaction between stellar winds and the interstellar medium (ISM). In particular, the stellar wind evolution of O- and B-type stars is calculated. First, the evolution of a stellar wind into the ambient interstellar medium and also a more dense molecular cloud are considered for the case of no relative motion between the star and the interstellar medium. This interaction results in a cavity being blown into the ISM. Of importance in this work is the boundary radius (astropause) of the stellar wind and also the location where the outflow speed decreases from supersonic to subsonic speeds, called the termination shock. Different parameters like ISM density, outflow speed and mass-loss rate were varied to study the effect these have on the computed astropause (AP) and termination shock (TS) radii. The evolution of these structures is presented up to a simulation time of 1 My. However, stars are not stationary relative to the ISM, and the evolution of stellar winds into the interstellar medium including relative motion is also considered. It is shown that the positions of the TS and AP are dependent on the mass-loss rate and stellar wind outflow speed of the star and the interstellar medium density and relative speed. When these massive stars reach the end of their life, they end their life in a supernova explosion. The explosion results in a blast wave moving outward, called the forward shock (FS) and a reverse shock (RS) also forms which moves inward. Previous work done by *Ferreira and de Jager* (2008) to simulate supernova remnant (SNR) evolution, was only done for the case of evolution into the undisturbed ISM (no cavity). In this work, the evolution of SNR is simulated taking also into account the pre-existing cavity blown out by the stellar winds of these massive stars. The results of this study showed that the evolution of the SNR is definitely influenced by the presence of a stellar wind cavity even if the cavity is only a few pc in extent.

Keywords: `stellar winds, interstellar medium, O- and B-type stars, termination shock, astropause, supernova remnant, molecular cloud`

Opsomming

'n Twee-dimensionele hirdodinamiese numeriese model is aangepas en uitgebrei om die interaksie tussen stellêre winde en die interstellêre medium (ISM) te simuleer. Spesifiek is die stellêre winde van O- en B-tipe sterre bereken. Eerstens word die evolusie van die stellêre winde in beide die interstellêre medium asook in digte molekulêre wolke ondersoek vir die geval waar daar geen relatiewe beweging tussen die ster en die interstellêre medium is nie. Hierdie interaksie het tot gevolg dat daar 'n lae-digtheid holte in die ISM ontstaan. Van belang in hierdie werk is die grensradius (astropouse) van die stellêre wind asook die posisie waar die uitvloeispoed verander van supersoniese na subsoniese waardes, genaamd die terminasieskok. Verskillende parameters soos ISM-digtheid, uitvloeispoed en massaverlies-tempo is verander om die effek wat hierdie parameters het op die berekende astropouse (AP) en terminasieskok (TS)-radiusse te bestudeer. Die evolusie van hierdie strukture is aangebied tot en met 'n simulasietydperk van een miljoen jaar. Sterre is egter nie altyd stationêr in die ISM nie, en dus word die evolusie van stellêre winde in die interstellêre medium met inagneming van relatiewe beweging ook aangebied. Daar word getoon dat die posisie van die TS en AP afhanklik is van die massaverlies en stellêre wind uitvloeispoed van die ster asook die interstellêre medium digtheid en relatiewe spoed. Wanneer hierdie massiewe sterre die einde van hulle lewe bereik gaan dit gepaard met 'n supernova-ontploffing. Hierdie het 'n ontploffingsgolf tot gevolg wat uitwaarts beweeg, die sogenaamde vorentoe skok (FS) en 'n omgekeerde skok (RS) vorm ook wat inwaarts beweeg. Vorige werk gedoen deur Ferreira en de Jager (2008) wat die evolusie van 'n supernova-res (SNR) gesimuleer het, is gedoen net vir die geval van evolusie in die ongestoorde ISM (geen holte). In hierdie werk word die evolusie van die SNR gesimuleer waar 'n bestaande holte in ag geneem word wat uitgewaai is deur die stellêre winde van hierdie massiewe sterre. Die resultate van hierdie studie het getoon dat die evolusie van die SNR defnitief beinvloed word deur die teenwoordigheid van 'n stellêre wind-holte, selfs indien die holte klein is.

Sleutelwoorde: `stellêre winde, interstellêre medium, O en B-tipe sterre, terminasieskok, astropouse, supernova-res, molekulêre wolk`

1

[1]Let wel dat die Engelse afkortings deurgaans gebruik word vir konsekwentheid.

Acronyms and Abbreviations

Listed below are the acronyms and abbreviations used in the text. For the purposes of clarity, any such usages are written out in full when they first appear in each chapter.

2D	Two Dimensional
3D	Three Dimensional
AP	Astropause
AS	Astrosheath
AU	Astronomical Unit
CNM	Cold Neutral Medium
FS	Forward Shock
GMC	Giant Molecular Cloud
HD	Hydrodynamic
HIM	Hot Ionized Medium
HMC	Hot Molecular Core
IR	Infrared
ISM	Interstellar Medium
MHD	Magneto-hydrodynamic
MC	Molecular Cloud
pc	parsec
PUI	Pick-Up Ion
RS	Reverse Shock
RSG	Red Super Giant
SNR	Supernova Remnant
SW	Solar wind / Stellar Wind
TS	Termination Shock
UCHII	Ultra Compact HII
UV	Ultraviolet
WC	Wolf-Rayet Carbon main fusion element
WIM	Warm Ionized Medium
WN	Wolf-Rayet Nitrogen main fusion element
WNM	Warm Neutral Medium
WR	Wolf-Rayet

Contents

Chapter 1

Introduction

The interaction of stellar winds with their surrounding interstellar medium (ISM) forms a cavity in the ISM. This cavity (bubble) around stars is called the influence sphere (astrosphere) of a star. It gives valuable information about the evolution of the stellar winds encapsulated in these bubbles. Of importance is the impact these bubbles have on the ISM during their evolution. These cavities may also have an influence on the evolution of supernova remnants (SNRs). The evolution of a star depends on its initial mass, whether its a solar-like star (with mass $\sim 1M_{\odot}$) or massive star with mass in excess of 20 $M_{\odot}$. Different mass corresponds to different mass-loss rates ($\dot{M}$) and different outflow speeds (v) resulting in different sizes of cavities.

Not being able to observe *in situ* what physically happens with the stellar wind of a star, numerical models were created using hydrodynamic (HD) and magneto-hydrodynamic (MHD) equations to simulate the interaction of stellar winds with the surrounding ISM. One of the most studied is that of the Sun's atmosphere, the "heliosphere", which is the influence sphere of the Sun. As a very thoroughly studied example of an "astrosphere", the heliosphere, is discussed first. For this purpose a brief overview is given from previous work done, in particular by *Snyman* (2007).

The aim of this work is to continue on the work done by *Snyman* (2007) using a similar model, but to apply this to different stellar winds, especially those from O- and B-type stars. A brief overview of the heliosphere, as an example, will show a history in developing state of the art numerical models to describe observations by different spacecraft and detailed studies to understand these observations. Once results obtained from a numerical model are compatible with observations, they can be applied with confidence in other areas.

1.1 The heliosphere

The heliosphere (the influence sphere of the Sun) is driven by the interaction of the solar wind, which is a highly ionized plasma of Solar origin expanding away from the Sun at supersonic speeds, and the Local Interstellar Medium (LISM). The solar wind blows a low density bubble

in the surrounding LISM. This interaction produces one or possibly two shock fronts, the inner called the termination shock (TS), and the outer called the bowshock of the interstellar medium (see e.g. *Scherer and Ferreira*, 2005). The latter depends on whether the inflow of the interstellar plasma is sub- or supersonic.

By the early 1970s the hydrodynamic treatment of expanding stellar winds (such as the solar wind) was well established (e.g. *Parker*, 1961; *Holzer*, 1972; *Axford et al.*, 1963). See also review by *Holzer and Axford* (1970). These studies of the solar wind-LISM interaction formulated that it consisted of several parts that had to be solved self-consistently: The first interaction that needed to be calculated was that of the ionized particles in the solar wind and LISM. After that the effect of neutral particles in the LISM on this interaction had to be taken into account. Due to the ionized nature of the solar wind and LISM, both these plasmas carry magnetic fields. Additional to the various mutual interactions between ionized and neutral particles, a solution to the electrodynamic equations describing the interaction between the magnetic fields and the plasma, in which it is embedded, had to be calculated self-consistently.

As computational resources increased, more detailed solutions to the solar wind-LISM interaction could be calculated. Initially, most of the numerical calculations neglected the magnetic field in the solar wind-LISM interaction. This led *Baranov and Malama* (1993) to formulate a model that treated the interaction between ionized particles (particles that have a negative or positive charge) in the solar wind and LISM hydrodynamically. The interaction with the neutral particle (a particle with no charge) population in the LISM was treated kinetically. Later work by *Pauls et al.* (1995) simplified the formulation of *Baranov and Malama* (1993) by treating the neutral component in the LISM hydrodynamically.

While this approach limits the state of the neutral species, it successfully captured the major characteristics of the heliosphere. Subsequent hydrodynamic formulations of the solar wind-LISM interaction were used in different studies (e.g. *Pauls and Zank*, 1996; *Zank et al.*, 1996; *Izmodenov*, 1997; *Pauls and Zank*, 1997; *Kausch*, 1998; *Holzer*, 1989; *Suess*, 1990; *Scherer and Fahr*, 2003; **?**; *Borrmann and Fichtner*, 2005; *Fahr et al.*, 2000; *Scherer and Ferreira*, 2005; *Ferreira and Scherer*, 2006). Recently, more sophisticated models including the heliospheric magnetic field were developed (e.g. *Florinski et al.*, 2003; *Pogorelov et al.*, 2006; *Opher et al.*, 2006) also including cosmic ray intensities (e.g. *Florinski and Jokipii*, 2003; *Ferreira and Scherer*, 2004, 2006; *Langner and Potgieter*, 2005; *Potgieter and Langner*, 2005; *Ball et al.*, 2005) found in this region.

Previous work done locally at the North-West University and by collaborators (e.g *Scherer and Ferreira*, 2005; *Ferreira and Scherer*, 2006; *Snyman*, 2007) utilized a hybrid (hydrodynamic and cosmic ray transport) numerical model to compute the interaction of the solar wind, the LISM, neutral hydrogen, and pickup ions (PUIs) to calculate the heliospheric interface. The model used by these authors is 2D (two dimensional) axisymmetric. In addition to their model, they added the calculation of the heliospheric magnetic field in the kinematic approximation (See *Pogorelov et al.*, 2004; *Opher et al.*, 2006, for examples of fully three-dimensional MHD computations). Another important fluid affecting the heliospheric geometry and included in their

hydrodynamic description is the PUIs. These ions, originating from the interaction of neutral H with the surrounding plasma, are of considerable importance because they remove both momentum and energy from the solar wind flow. The solar wind gets decelerated, therefore reducing the ram pressure and subsequently the size of the heliosphere.

This model will be used in this study to first calculate stellar wind evolution and later SNR evolution in the cavities created by the stellar wind evolution. However, before applying and extending this model it will first be illustrated how this approach successfully calculates the heliosphere as an example of a stellar wind (astrosphere). Within the heliosphere, various spacecraft like Voyager 1 and 2 and Ulysses contribute to our better understanding of astrospheres by providing *in situ* observations that models can use as input and test results against.

1.2 Properties of the solar wind

In this section, properties of the solar wind, which is responsible for the heliosphere, are briefly provided. The solar wind originates from the solar corona, where the outward force on the particles due to the magnetic field outweighs the gravity of the Sun. From there it travels radially outward, passing the Earth at a distance of one Astronomical Unit (1 AU). The following table provides some physical quantities of the state of the solar wind at the distance of 1 AU from the Sun.

Table 1.1: Properties of the solar wind.

	Solar Wind
Density (ρ)	$5 - 7$ (cm^{-3})
Speed (slow)	400 (km.s^{-1})
Speed (fast)	800 (km.s^{-1})
Temperature (slow)	$0,7 - 1,5$ (10^5) (K)
Temperature (fast)	8 (10^5) (K)

These properties are for the case of solar minimum conditions where there is a distinct transition between the speed of the solar wind at the polar regions (fast) and the speed at the equatorial regions (slow). The fast solar wind has a speed of $\sim$ 800 km s^{-1} (See e.g. *Krieger et al.*, 1973; *Zirker*, 1977; *McComas et al.*, 2006, and references theirin) and the speed of the slow wind is $\sim$ 400 km s^{-1} (e.g. *McComas et al.*, 2000, 2006). The speed of the solar wind for solar maximum conditions is in the range of 400 km s^{-1} (e.g. *Schwenn*, 1983; *Marsch*, 1991) and is also highly variable. To give an approximate representation of how the heliosphere looks like, Figure 1.1 shows the different shock structures that forms due to the interaction of the solar wind with the surrounding ISM.

The *in situ* observations by different spacecraft, that are provided in Table 1.1 are not available for other stars where one is limited to inferred values from telescope measurements.

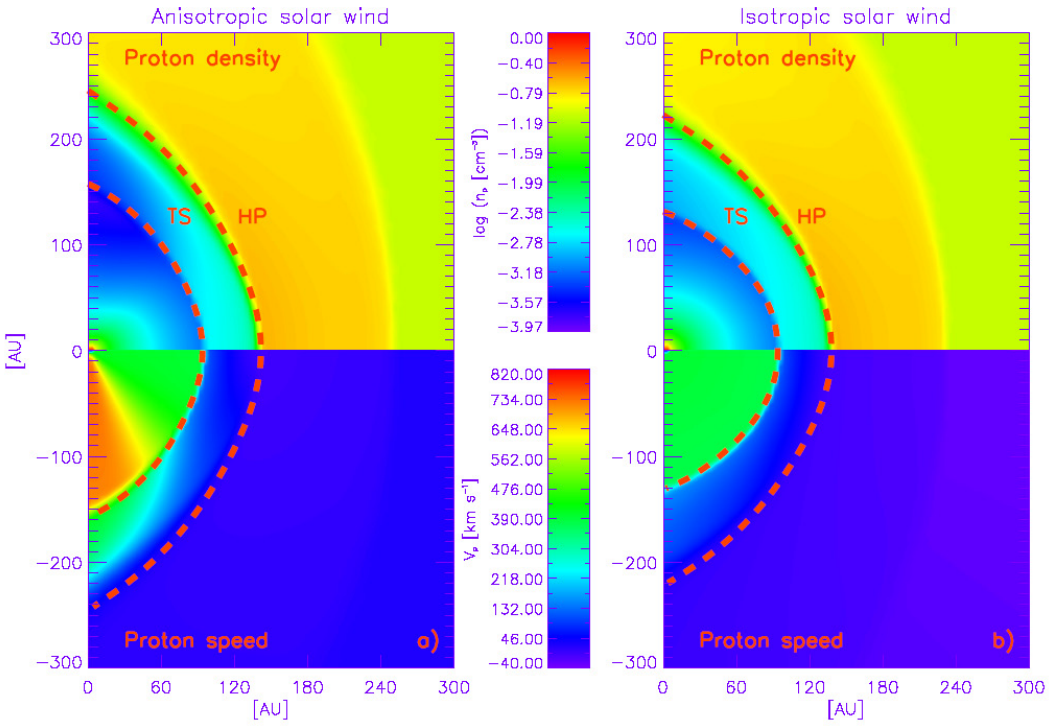

Figure 1.1: Shows an example of the heliosphere in terms of density (top panel) and speed (bottom panel) of each panel. The left panel corresponds to solar minimum with a anisotropic solar wind speed. The right panel corresponds to solar maximum with an isotropic solar wind speed.

1.3 Testing the numerical model

Figure 1.2 shows averaged values of both the number density and solar wind speed in the time interval from January 1990 to December 2008 as measured by Voyager 2 (data from http://cohoweb.gsfc.nasa.gov.). Shown in the top panel of Figure 1.2 is the radial distance of the Voyager 2 spacecraft from the Earth, increasing in distance as a function of time. The middle panel shows the density of the solar wind as function of time, and the bottom panel shows the solar wind speed as function of time. Evident from the middle panel of Figure 1.2 is that the density of the solar wind decreases with increasing distance from the Sun, as $\rho \propto \frac{1}{r^2}$, with ρ the density and r radial distance. From the middle and bottom panels follows that at the end of 2007, there is an increase in the density and a sudden decrease in the speed of the solar wind protons. This is in direct accordance with what should happen to the physical properties of the solar wind if it were to travel across a shock.

As a test to establish the accuracy of the numerical model, *Snyman* (2007) used observational data from the Voyager spacecraft, as shown in Figure 1.2, to show how the model of *Fahr et al.* (2000) and *Scherer and Ferreira* (2005) can be used to predict at what time Voyager 2 would cross the termination shock. Starting from 1 January 1990, the data (density and speed of the solar wind) were binned into 26-day intervals (26 days being the rotational period of the Sun) and

then used as boundary conditions in the model.

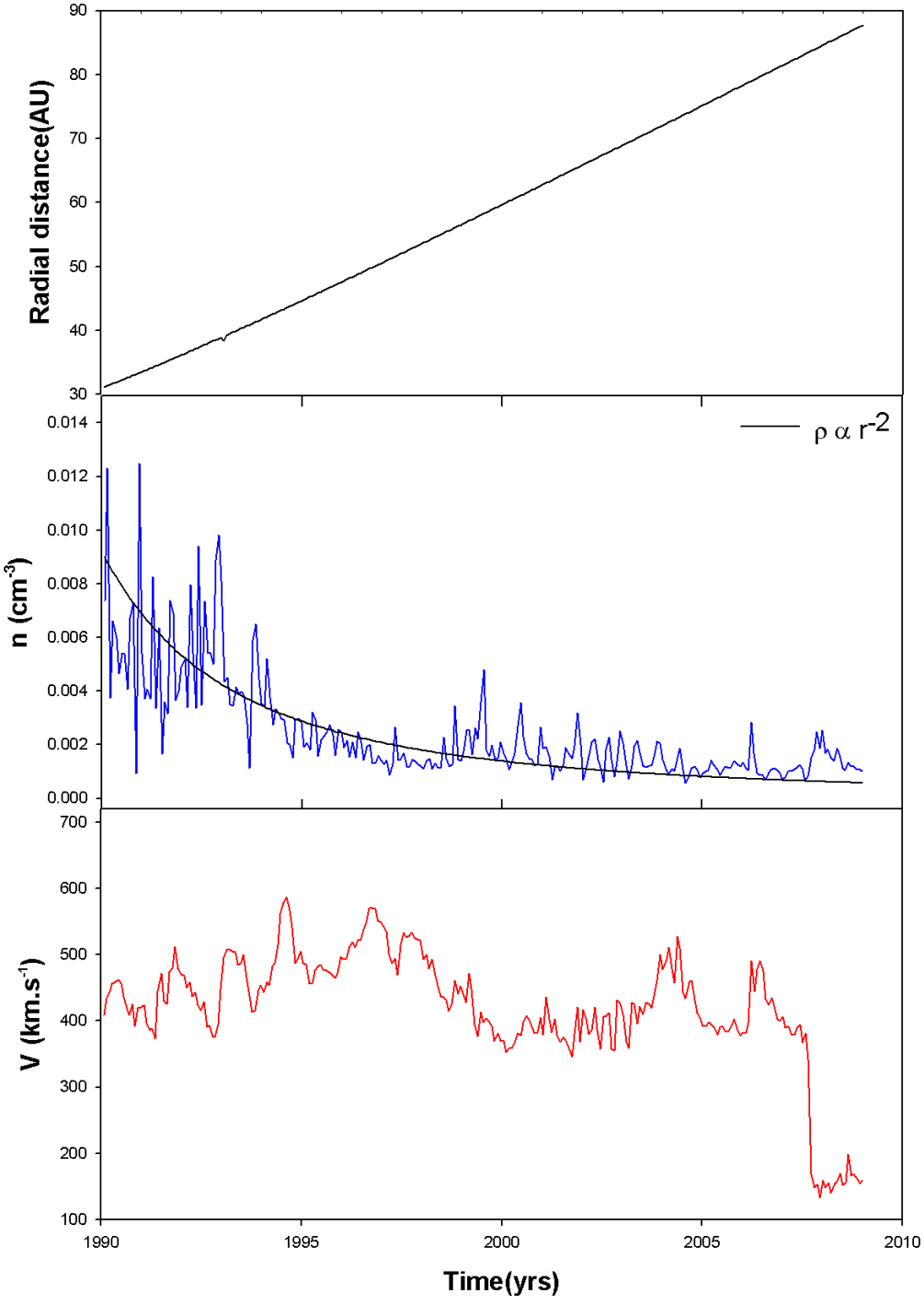

Figure 1.2: Top panel: The radial distance of the Voyager 2 spacecraft. Middle panel: Solid blue line is the 26-day averaged number density measured by Voyager 2 and the solid black line the $\rho \propto \frac{1}{r^2}$ dependence. Bottom panel: The solid red line is the averaged proton velocity measured by Voyager 2. Data provided by http://cohoweb.gsfc.nasa.gov.

However, the solar wind and LISM states, within the context of hydrodynamical models, are

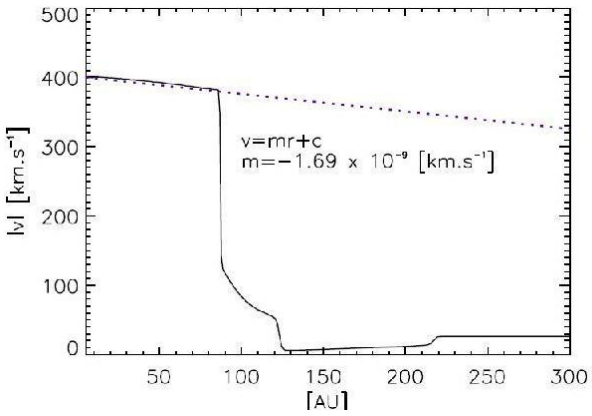

Figure 1.3: The radial proton speed along a radial path in the nose (solid black line) direction of the heliosphere. The decrease in the speed between the Sun and TS is approximately linear, as shown by the dotted line above. From *Snyman* (2007).

specified at appropriate boundaries. The location of the spacecraft and the observations do not necessarily correspond to these boundaries. This means that observations describing the state of the solar wind that were observed at a certain point in space and time need to be extrapolated to 1 AU (corresponding to the inner boundary of the numerical model) and adjusted in time. It was calculated by *Snyman* (2007) that the solar wind density $\rho \propto \frac{1}{r^2}$ between the Sun and the TS as shown by the middle panel of Figure 1.2 for example. Therefore, if a density n is observed at position r the r^{-2} proportionality implies that

$$nr^2 = n_{1AU} r_{1AU}^2 = constant, \tag{1.1}$$

where n_{1AU} is the density at 1 AU and r_{1AU} = 1 AU. From Equation 1.1 the density n at 1 AU can be calculated. *Snyman* (2007) also shown that the solar wind speed decreases between the Sun and TS due to the interaction between protons and hydrogen atoms. The decrease in solar wind speed was shown to be approximately linear in r (as shown in Figure 1.3), implying that

$$v \approx mr + c \qquad for \qquad 0 \leq r < r_{TS} \tag{1.2}$$

where v is the proton speed (outflow speed) and

$$m = -1.69 \times 10^{-9} s^{-1}. \tag{1.3}$$

From Equation 1.2, c can be calculated using m from Equation 1.3 and the observed speed at position r. This gives a value of c = 400 km s^{-1} at the inner boundary where r = 0 as shown by Figure **??**. The speed measured by a spacecraft can be extrapolated back to 1 AU using Equation 1.2. If it is assumed that the state of the LISM is constant over the timescale involved, then the value of m in Equation 1.2 (corresponding to the slope of the speed profile in the figure)

remains approximately the same irrespective of the solar wind activity. By extrapolating the observed solar wind density and speed values back to 1 AU, the time at which these observations are made, is changed. Therefore, the time at which these observations of the solar wind state are made must also be adjusted.

Therefore, observing the state of a certain sample of the solar wind particles at a point in time and space by a spacecraft and extrapolating this state back to 1 AU should be similar to an observation of the same sample of protons at 1 AU at an earlier time. By integrating Equation 1.2 over time (where t_1 denotes the time at which the observation is made by the spacecraft and t_0 is the time at 1 AU) yields

$$t_1 - t_0 = \frac{1}{m} \ln \left| \frac{mr_1 + c}{mr_0 + c} \right|, \tag{1.4}$$

where r_1 is the radial position at which the observation is made at time t_1 and r_0 corresponds to 1 AU. Making use of Equation 1.1, Equation 1.2 and Equation 1.4, the solar wind observations from Voyager 2 were extrapolated back to 1 AU by *Snyman* (2007) with the time adjusted accordingly. This was then used as a time dependent boundary condition describing the solar wind state at 1 AU in a hydrodynamical model of the solar wind-LISM interaction. The result of this is a record of the approximate state of the heliosphere for the past $\sim$ 20 years, for the condition that the solar wind speed is constant. This condition is valid for both V1 and V2 due to their latitude, which puts them inside the slow solar wind in solar minimum conditions.

Figure 1.4 (from *Snyman*, 2007) shows extrapolated (back to 1 AU) data for a variety of different spacecrafts as discussed above. The actual daily observations from Helios 1 and 2, Pioneer 10 and 11 as well as the Voyager 2 and Ulysses spacecraft (depending on whether that spacecraft was active during that time interval) were used for this purpose. The top panel shows the speed, the middle panel the particle density and the bottom panel shows the dynamic pressure of the extrapolated (back to 1 AU) data for the time interval 1970 to 2007. The red line is the averaged upper value for a 26-day time interval, the blue line is the lower value for a particular 26-day averaged time interval, and the black line is the mean value of a particular 26-day averaged time interval taken from each spacecraft. The data is shown in Figure 1.3 and provides an appropriate time dependent description of the state of the solar wind at 1 AU, which was used as an inner boundary condition in a hydrodynamical model of the solar wind-LISM interaction.

Figure 1.5 shows the results of *Snyman* (2007) where the computed termination shock distance as a function of time together with the trajectory of both the Voyager 1 and Voyager 2 spacecraft. *Snyman* (2007) used this figure to predict when the Voyager 2 spacecraft would cross the TS. Both crossings were calculated using this time dependent model with the Voyager 1 crossing already known. From Figure 1.4 follows that the model, as used by *Snyman* (2007) to simulate this scenario, resulted in an accurate presentation of the position of the termination shock, because Voyager 1 crossed it in December 2004 at $\sim$ 94 AU (see e.g *Richardson et al.*, 2008;

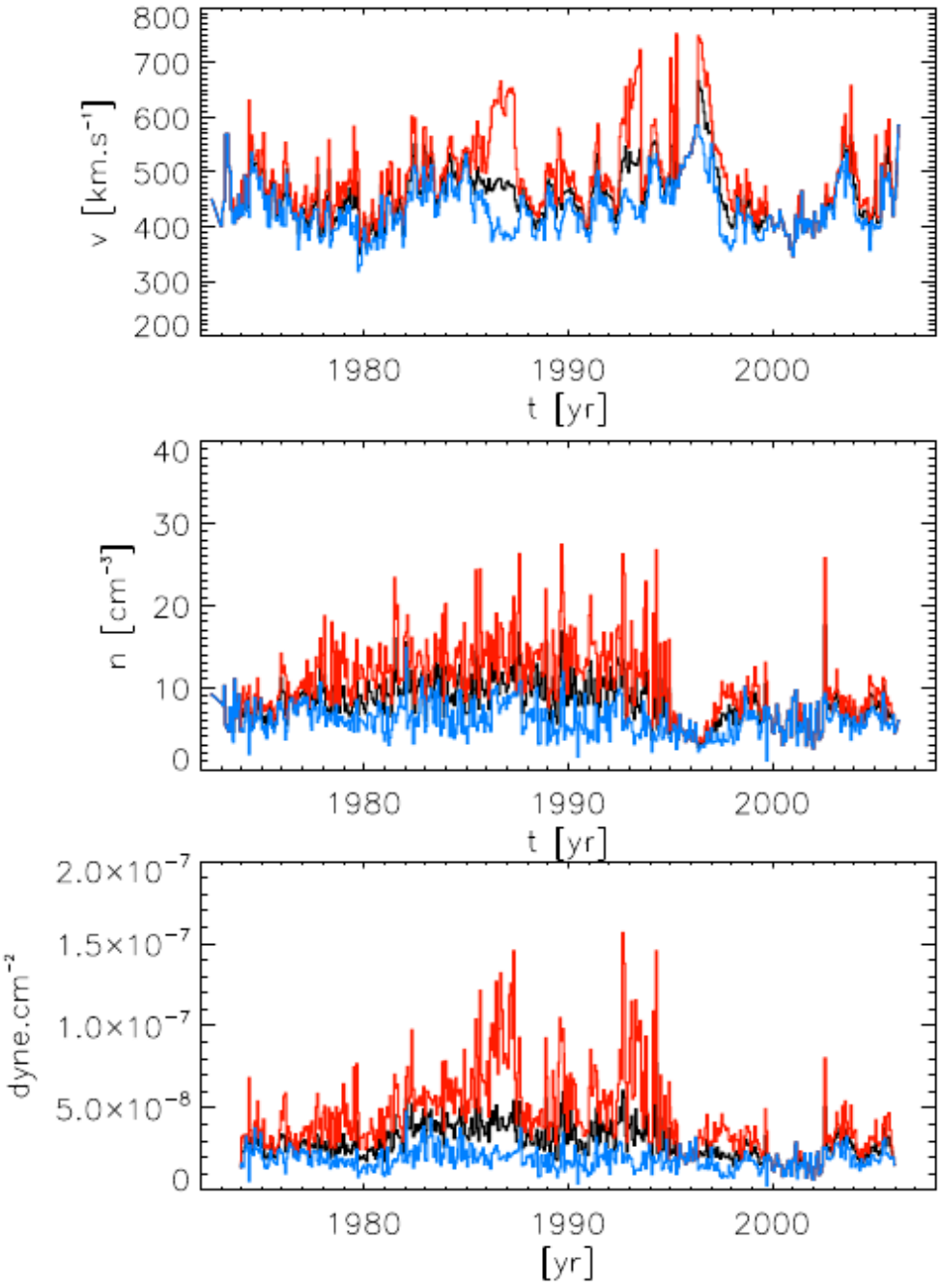

Figure 1.4: Upper (solid red line), lower (solid blue line) and mean values (solid black line) of 26-day averaged values of the solar wind speed (top), density (middle) and subsequent dynamic pressure (bottom). The actual daily observations from the Helios 1 and 2, Pioneer 10 and 11 as well as the Voyager 2 and Ulysses spacecraft are extrapolated back to 1 AU using Equations 1.1, 1.2 and 1.4 and averaged over 26-day intervals. From *Snyman* (2007).

Stone et al., 2005) and Voyager 2 crossed it at $\sim$ 84 AU in August 2007 (see e.g *Stone*, 2008).

The success of the *Snyman* (2007) approach to simulate, for example, the TS position realistically leads to confidence in this model and it is now applied to simulate astrospheres (stellar winds) of other stars.

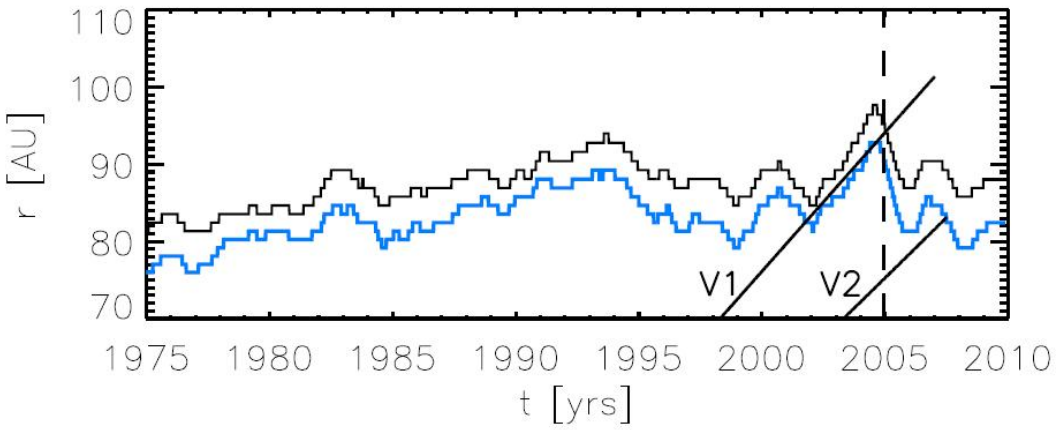

Figure 1.5: The calculated radial position of the termination shock at 34.1 deg latitude (solid black line) and −27 deg latitude (solid blue line). The figure shows the termination shock position calculated from the mean values shown in Figure 1.3. Also shown are the radial positions of both Voyager 1 and Voyager 2 (V1 and V2) in time. The vertical dashed line indicates the time at which Voyager 1 crossed the termination shock. From *Snyman* (2007).

1.4 Aim of this work

- The aim of this work is to extend an existing hydrodynamic model to calculate stellar wind and supernova remnant evolution. This model uses a finite volume method to calculate the heliosphere, but must be adapted to simulate stellar evolution by extending it to handle the much larger cavities resulting from the stellar winds of O- and B-type stars. This model was first developed by *Kausch* (1998) (see also *Fahr et al.*, 2000) and adapted by e.g. *Scherer and Ferreira* (2005) and implemented locally at the NWU by *Snyman* (2007).
- This model is then applied to calculate stellar winds in different ISM conditions. These calculations then present a dynamic evolution of stellar winds from high mass stars. The conditions mentioned previously include a range of ISM densities, stellar mass-loss rates (See e.g. *de Loore et al.*, 1977; *Chiosi and Nasi*, 1974) and stellar wind speeds (see *Bernabeu et al.*, 1989).
- Lastly, this model is applied to first calculate a cavity resulting from a stellar wind, and then the evolution of an SNR in such a cavity. The effect of such a cavity on SNR evolution can then be investigated.

1.5 Overview of the chapters to come

- In Chapter **2**, background is given on the topic of the Interstellar Medium (ISM) and interstellar magnetic field. A discussion is also given on the different clouds and composition of these clouds from where main-sequence stars form. The evolutionary track of these massive main-sequence stars will also be discussed. Thereafter, a discussion will follow on the topic of the stellar winds of these massive main-sequence stars.

- In Chapter **3**, the appropriate equations and numerical technique used to simulate the evolution of these stellar winds are given. The method are based on the finite volume method.
- In Chapter **4**, model results will be shown and discussed. The focus of this chapter is to model the evolution of different stellar winds over time for the case where there is no relative motion between the ISM and the star. In particular the focus is on the Astropause (AP) and termination shock (TS) distance as a function of time and how the time evolution of these structures is influenced by different parameters.
- In Chapter **5**, relative motion between the star and ISM is taken into account and the influence of this parameter on the structure of stellar wind cavities is shown.
- In Chapter **6**, the stellar wind profiles, obtained from Chapter **4**, will be used as input to simulate supernova explosions inside these stellar wind cavities. This is done to see whether these stellar wind cavities, created by the stellar winds, have a significant influence on supernova evolution.
- In Chapter **7**, the main results obtained from the previous chapters will be discussed and conclusions summarized.

Chapter 2

The interstellar medium, molecular clouds, star formation and stellar evolution

2.1 Introduction

The structure and energetics of the interstellar medium (ISM) in galaxies are sculptured by the mechanical energy and momentum inputs from winds and supernova remnants (SNRs) from massive stars. As will be shown in later chapters, the ISM density influences the evolution of stellar winds and therefore a discussion on the ISM (see *McKee and Ostriker*, 1977) is necessary.

The aim of this chapter is to provide a brief overview and some discussions on the topic of the interstellar medium, star formation and stellar evolution. This includes descriptions of the three-component ISM model by *McKee and Ostriker* (1977) and molecular clouds (MCs) which are one of the phases of the ISM. Emphasis is on the physical properties inside these clouds such as the density, temperature and the individual masses of these structures. Knowing these parameters is important for simulations. This chapter also includes a discussion on the different modes of stellar formation, whether it is a cluster, single massive stars or a binary system (see e.g *Lada and Lada*, 2003).

Because the focus of this project is to simulate the evolution of stellar winds of massive stars, a brief discussion of early stellar evolution of massive stars inside hot molecular cores (HMCs) is also given. This is the phase of stellar evolution where the stellar object is still deeply embedded inside its natal molecular core while still accreting material. As part of early star formation, the radiation from the star is also discussed. Subsequently the evolution of the H II (ionized hydrogen molecules) regions around massive stars is discussed. When the radiation pressure caused by the radiation from the star begins to dominate the gravitational force of the material of the stellar envelope, the star then starts to blow away charged particles from its surface, known as its stellar wind. Lastly the stellar wind is discussed.

2.2 The interstellar medium and the interstellar magnetic field

The stars, including massive O- and B-type (O-type stars have dominant lines of absorption and sometimes emission for He II lines and neutral helium lines and prominent hydrogen Balmer lines, while the spectra of B-type stars have neutral helium and moderate hydrogen lines and ionized metal lines) stars in our galaxy are embedded in the ISM, which consists of ordinary matter (including electrons and neutral or ionized elements), relativistic charged particles known as cosmic rays, and magnetic fields, all of which are coupled together by electromagnetic forces. The ISM in galaxies is believed to consist of highly inhomogeneous structures and a wide variety of physical and chemical states (*Myers*, 1978) as well as a variety of temperatures. The extent of these structures can be a couple of astronomical units (AU) to thousands of AU. These structures, among others, also consist of ionized molecular clouds, gaseous nebulae, bubbles and super bubbles, all giving the ISM its characteristic inhomogeneity.

The total mass of the ISM is a very small fraction of the mass of the Galaxy, approximately 0.5%. The ISM is mainly constituted by gas ($\sim 99\%$ of the total mass) and the rest by submicron-sized dust grains intermixed with gas. The composition of the above-mentioned ISM gas (both neutral and ionized) by mass is 70% hydrogen, 28% helium and about 2% heavy elements such as C, N, O, Mg, Si, S, and Fe (*Lequeux and Ryter*, 2005).

The ISM density is closely related to the structure of the ISM, as well as the temperature and the magnetic fields, and in turn these also contribute to the overall structural behaviour. The ISM is not evenly distributed, but condenses in clouds that give rise to a bubble-like structure. The ISM is spread very thinly, with an average density of about 10^{-24} g cm^3 (*Ferrière*, 2001). However, there is huge variability about this average.

The densest parts, which include maser (microwave amplification by stimulated emission radiation) regions, contain 10^{-14} g hydrogen molecules per cm^3 and they are also the coldest, with temperatures close to absolute zero. The hottest material has temperatures of 10^8K and densities of 10^{-26} g cm^3 or less (see Figure 2.1). From this description of the ISM, we can assume that the ISM consists of different phases according to different density and temperature regimes, discussed next.

McKee and Ostriker (1977) suggested that the ISM is dominated by a pervasive hot ionized intercloud medium (HIM). They also presented a model where the ISM is regulated by Supernova (SN) explosions. Their model consists of three essential phases shown in Figure 2.1 and discussed below.

Figure 2.1 shows a hot low-density ionized medium (HIM), which is moderately inhomogeneous due to blast waves from prior SN explosions, and which surrounds the other phases. This phase has an average atomic density $n_{HIM} \approx 10^{-26}$ g cm^{-3} and a temperature $T_{HIM} \approx 10^{5.7}$ K. Embedded in this hot medium are cold, neutral, relatively dense clouds, called the cold

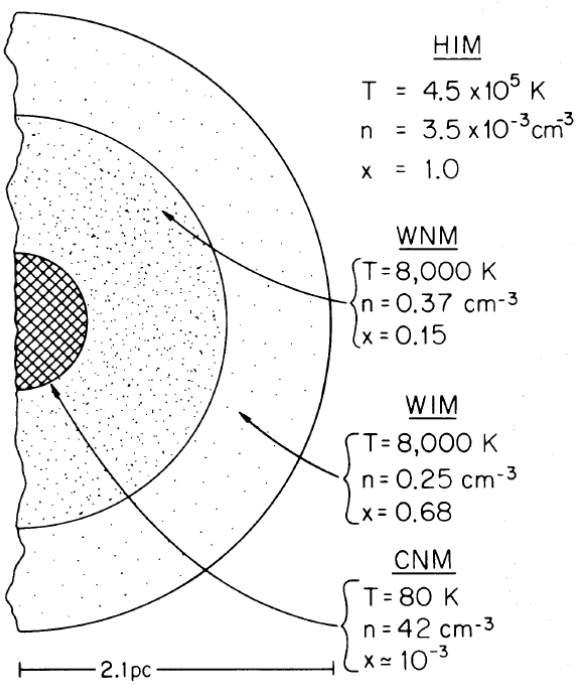

Figure 2.1: A cross section of a characteristic small cloud. The crosshatched region shows the cold neutral medium (CNM). The next layer is the warm neutral medium (WNM) with the warm ionized medium (WIM) surrounding it, all of which is surrounded by the hot ionized intercloud medium (HIM). Values for the hydrogen density n, temperature T, and ionization $x = n_e/n$ are also indicated for each of these regions. From *McKee and Ostriker* (1977).

neutral medium (CNM), which has an internal density and temperature of $n_{CNM} \approx 10^{-23}$ g cm^{-3} and $T_{CNM} \approx 10^{1.9}$ K respectively. Surrounding this CNM phase, are two regions of the warm medium that occupy a much larger volume, with a temperature of ~ 8000 K and lower densities. These two regions differ from each other by fractional ionization that occurs in them. The regions are known as the warm neutral medium (WNM) and the warm ionized medium (WIM). These regions both have more or less the same density $n_{WNM} \approx n_{WIM} \approx 10^{-25}$ g cm^{-3}. The WNM has a fractional ionization of 0.1, and the WIM has a fractional ionization of 0.7 (*McKee and Ostriker*, 1977), meaning that the WNM is only 10% ionized, whereas the WIM is 70% ionized. All these various phases of interstellar matter coexist in a rough pressure equilibrium. These clouds expand and contract mainly due to their energy balance. They expand when they absorb more energy from the surroundings than they emit, and contract in the opposite case (*Pirronello et al.*, 2007).

Figures 2.1, 2.2 and 2.3 from *McKee and Ostriker* (1977) show illustrations of the ISM phases at different scales. Although these are rather crude and oversimplified illustrations, they enable us to get a general idea of the physical extent of the ISM. These are discussed next.

Figure 2.2 (from *McKee and Ostriker*, 1977) shows the small-scale structure of the ISM in a region of 30×30 pc. Each of the circular bubbles represents a small cloud as presented in Figure 2.1. It also shows how these small clouds are misformed and compressed as an SN blast wave moves over them. However, the large-scale structures as shown in Figure 2.3 (from *McKee and Ostriker*,

1977) can significantly alter the morphology of SN remnants if there exists a density gradient in the surrounding ISM in which the SNR expands (see also *Ferreira and de Jager*, 2008). The large bubbles represent SNRs and the small bubbles are the small clouds mentioned earlier.

Now the focus shifts to the interstellar magnetic field. The interstellar magnetic field is very important in the physics of the interstellar matter, because at large scales the magnetic pressure adds to the kinetic non-thermal pressure of the interstellar gas to balance gravitational attraction. The presence of interstellar dust can be inferred by linear polarization that is due to the alignment of the grains in the galactic magnetic field (*Davis and Greenstein*, 1951).

Polarization like this gives evidence of the elongated nature of the dust grins as well as the presence of an interstellar magnetic field. The presence of an interstellar magnetic field in our Galaxy was first revealed by the observational discovery of linear polarized starlight (see e.g *Hall*, 1949). *Davis and Greenstein* (1951) also concluded that the local interstellar magnetic field is parallel to the Galactic plane. *Mathewson and Ford* (1970) were the first to put together a large-scale polarization database that consisted of ∼7000 stars distributed over both celestial hemispheres. Using their database, *Mathewson and Ford* (1970) indicated that the local magnetic field is nearly azimuthal, pointing towards a galactic longitude of $\sim 80^\circ$ (i.e. it has an inclination angle of 10°). However, by re-evaluation of the polarization data of *Mathewson and Ford* (1970), it was found that the inclination angle of the local magnetic field is $\sim 7.2^\circ$ (*Heiles*, 1996). Data from optical observations yielded an inclination angle of $\sim 12^\circ$ for the local magnetic field (*Georgelin and Georgelin*, 1976) and from radio data it is inferred as $\sim 13^\circ$ (*Beuermann et al.*, 1985).

This method only enables the determination of the direction of the magnetic field. However, to determine the strength of the magnetic field one of the following three methods has to be used: (1) analysis of the Zeeman splitting of the 21 cm HI-line, (2) the Faraday rotation of linearly po-

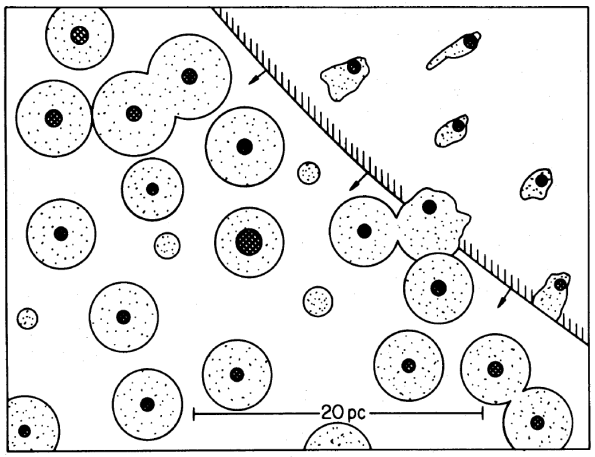

Figure 2.2: A close-up view of the small-scale structure of the ISM. A cross section of a representative 30 x 30 pc is shown where the subsequent regions are approximately proportional to their filling factors. In this figure an SN blast wave is expanding into the region from the upper right corner. From *McKee and Ostriker* (1977).

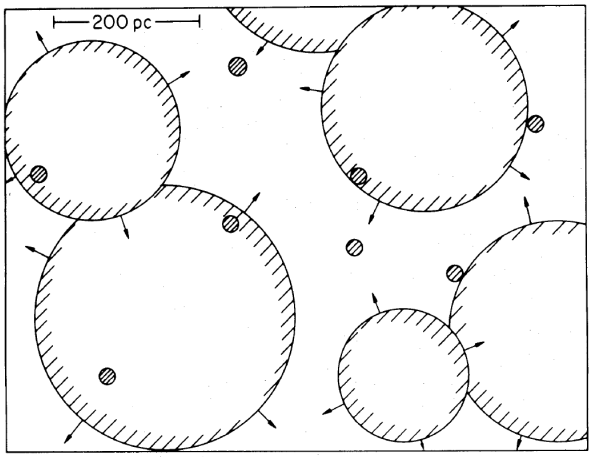

Figure 2.3: A large-scale view of the structure of the ISM. This figure shows a region of 600 x 800 pc. Altogether about 9000 clouds would occur in a region of this size. From *McKee and Ostriker* (1977).

larized radio signals or (3) the radio synchrotron emissions from relativistic electrons (*Ferrière*, 2001). The Zeeman effect is the splitting of a spectral line due to the presence of a magnetic field. However, this only happens for magnetic field strengths in the order of 0.4 Tesla. If the magnetic field differs from this strength, line broadening occurs. For fields with strength < 0.4 Tesla, the strength can then be deduced by the measuring of the polarization of the region of an absorption or emission line that is far removed from the line's peak. The amplitude of the Zeeman splitting , $\Delta\nu \propto B$, thus to measure $\Delta\nu$ would be enough to obtain B in the region of interest.

However, for the case of the 21 cm HI line, $\Delta\nu$ is too small and cannot be measured in practice. *Verschuur* (1969) was the first to overcome this problem by measuring the difference between the two circularly polarized components of the 21 cm radiation, yielding the line-of-sight magnetic field component $B_{||}$. From a compilation of Zeeman splitting observations, *Troland and Heiles* (1986) found that the interstellar magnetic field has typical strengths of a few μG in regions with a gas density n between 10^{-24} g cm^{-3} and 10^{-22} g cm^3, displaying a tendency for B to increase with increasing n. The Zeeman splitting tends to occur mainly toward cold neutral clouds, whereas Faraday-rotation occurs in the direction of ionized regions.

The sources that are used for Faraday-rotation measurements, which is the rotation of the polarization-plane of an electromagnetic wave as it passes through a region containing free electrons and a magnetic field, are either pulsars or extragalactic radio continuum sources. *Rand and Lyne* (1994) determined that the local uniform magnetic field strength is 1.4 μG by analyzing polarized light from various pulsars in our Galaxy. Synchrotron radiation (also known as magneto bremsstrahlung) is the radiation emitted by a charged particle (usually an electron) moving in a magnetic field at a velocity very close to that of light. *Beuermann et al.* (1985) obtained a local magnetic field strength of $B \sim 5.0$ μG by modelling the emissivity of Galactic synchrotron radiation. *Beck* (1986) also dtermined that the magnetic field strength is in the

order of a few μG by using all three methods.

The values discussed above, for the strength of the interstellar magnetic field, are all in the order of a few μG, which shows that all of these techniques are appropriate for determining the strength of the magnetic fields in the ISM. Furthermore, *Men et al.* (2008) put observational constraints on these three methods.

2.3 Molecular clouds

As mentioned earlier, MCs are one of the phases of the ISM. However, MCs differ from the rest of the ISM because they are the sites of star formation where the gas contained inside of them is the coldest and densest of anywhere else in the Universe (*Lopez et al.*, 2010). It is believed that all present day star formation takes place inside of MCs (*Blitz*, 1991). It is also stated by *Blitz and Williams* (1999) that the MC's association with star formation is so strong that it can generally be assumed that one will always be able to find molecular gas in the vicinity of young stars and vice versa. Due to the temperature of the MCs, most of the material (consisting of H_2) is in molecular form. Temperatures range from 10-50 K with particle densities higher than 10^2 cm^{-3}.

MCs have a variety of different structures and are difficult to classify in detail. They were broadly classified by *Carroll and Ostlie* (2007) in the following way (also summarized by *De Villiers*, 2009):

- **Diffuse MCs/translucent MCs**

  These are clouds where hydrogen gas is primarily in atomic form. Conditions in these clouds are typical of diffuse H I clouds (low number density, neutral hydrogen gas), but with somewhat higher masses and temperatures of $\sim$ 15-50 K, number density of $n \sim 2 \times 10^2$ cm^{-3} (meaning 2×10^2 particles per cubic centimeter), masses of $\sim 3 - 100 M_\odot$, sizes of several parsecs across, and they also tend to be irregularly shaped.

- **Giant Molecular Clouds (GMCs)**

  Such clouds are enormous and they are composed of dust and gas with a clumpy structure. Inside there are also regions with densities greater than the mean density. They have typical temperatures of $\sim$ 15-20 K and number densities in the order of $\sim 10^2$ cm^{-3}, and masses of $\sim 10^5 M_\odot$. They also have typical sizes of $\sim$ 50 pc across. A very well-known example of such a GMC is the *Horsehead nebula*.

- **Dark cloud complexes**

  They are complex structures that have diameters in the order of $\sim$ 10 pc and temperatures of $\sim$ 10 K. They have masses in the order of $\sim 10^4 M_\odot$ and number densities of $n \sim 5 \times 10^2$ cm^{-3}.

- **Clumps**

  These structures are smaller, individual parts inside dark cloud complexes with diameters of a couple of parsec and with number densities in the order of $n \sim 10^3$ cm^{-3}. Their temperature is in the range of $\sim$ 10 K and contains $\sim 30 M_\odot$ of mass.

- **Dense cores**

  These structures are even smaller with characteristic diameters of $\sim$ 0.1 pc, and contain mass in the order of $\sim 10 M_\odot$. They have number densities of $n \sim 10^4$ cm^{-3} and temperatures of $\sim$ 10 K.

- **Hot Molecular Cores (HMCs)**

  These structures are even smaller than dense cores with sizes ranging from $\sim$ 0.05-0.10 pc, temperatures of $\sim$ 100-300 K and masses that can reach up to 3000 $M_\odot$. They also have very large number densities in the order of $n \sim 10^7 - 10^9$ cm^{-3}.

- **Bok globules**

  Such clouds have almost a spherical shape and are located outside of larger molecular complexes. They have typical sizes of less then $\sim$ 1 pc and low masses in the order of $\sim 1000 M_\odot$, relatively large number densities of $n > 10^4$ cm^{-3} and low temperatures around $\sim$ 10 K.

Giant molecular clouds (GMCs) are sites of active star formation, and contain mass in the order of 10^4 - 10^5 $M_\odot$ and are generally confined to the spiral arms of galaxies (*Blitz and Williams*, 1999). *Williams et al.* (2000) also describe the internal structure of these GMCs as follows (where these structures are included in the summary above):

- *Clumps* (clumps as mentioned above in the summary of *Carroll and Ostlie* (2007)) are coherent regions in longitude-latitude-velocity space that are generally identified from spectral line maps of molecular emission, and exhibit the same physical properties.
- *Star-forming clumps* (dense cores as mentioned above) are the massive clumps out of which stellar clusters form.
- *Cores* (hot molecular cores as mentioned above) are the regions out of which single stars (or multiple star systems like binaries) are formed.

To show the structure of these clouds, a schematic representation is given in Figure 2.4, which shows the hierarchy of structures within molecular clouds. These structures include clumps and hot molecular cores, as mentioned above.

In the case of *star-forming clumps*, it is believed that they are the birth place of star clusters, called embedded clusters. These clumps evolve into dense cores due to the supersonic and

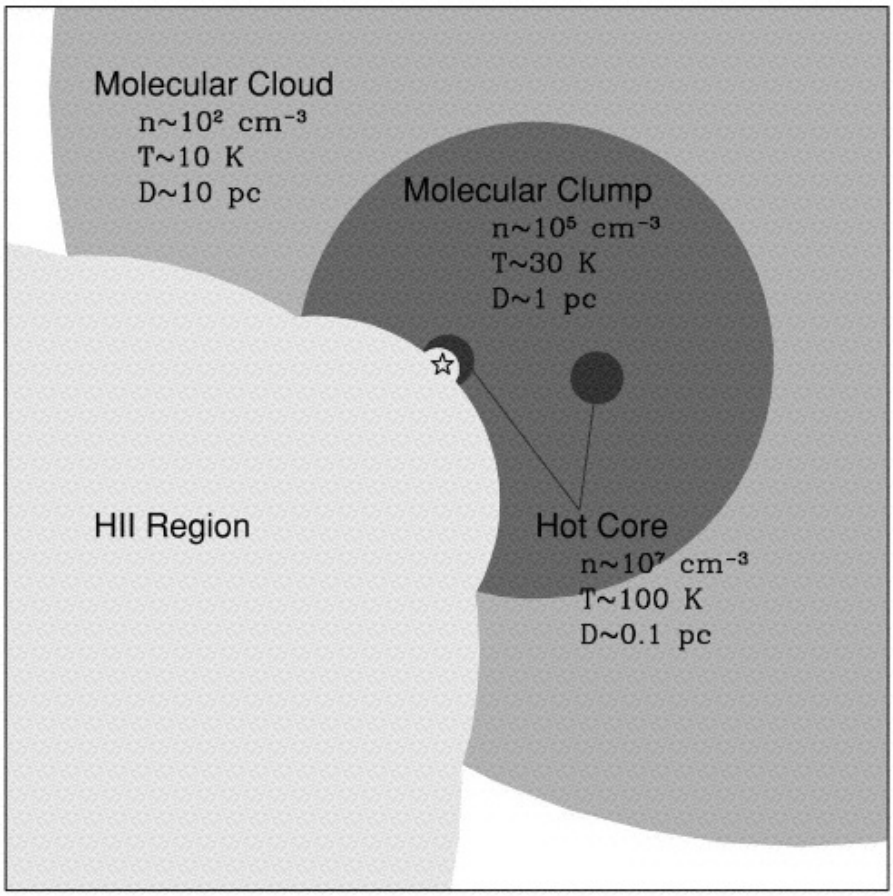

Figure 2.4: A schematic representation showing the hierarchy of structures within molecular clouds. Inside the clouds there are clumps, and within the clumps there are cores. A massive star is forming inside a hot molecular core. From *Kim and Koo* (2001).

turbulent velocity fields inside GMCs (*Lada and Lada*, 2003), which cause collisions that, under the right conditions, can become gravitationally unstable, forming these dense cores and decoupling. The largest and most massive of these fragments are the potential sites of cluster formation. The physical properties of these dense cores associated with embedded clusters are that they are the most massive (100-1000 $M_{\odot}$) and dense ($H_2 \sim 10^4 - 10^5$ cm^{-3}) cores within the clumps. These clusters (group of stars of more than ten) exhibit the same physical types (*De Villiers*, 2009).

Shown in Figure 2.5 is a schematic representation of the evolution of such a cluster of stars. The stars of this cluster (OB association) were formed in a *dense core*, on the edge of an MC. The top panel of Figure 2.5 shows the evolution of a cluster of stars after a period of 1 My, where the stars are still embedded in a dense core inside the GMC. The middle panel shows the evolution of the stars after a period of 3 My, at which time they photo ionized the GMC and formed a super (H II) bubble around them. The bottom panel shows the evolution after a period of 9 My; at this time the stars become part of the general population of stars.

It is believed that HMCs inside MCs are the birth places of massive single stars, or binary

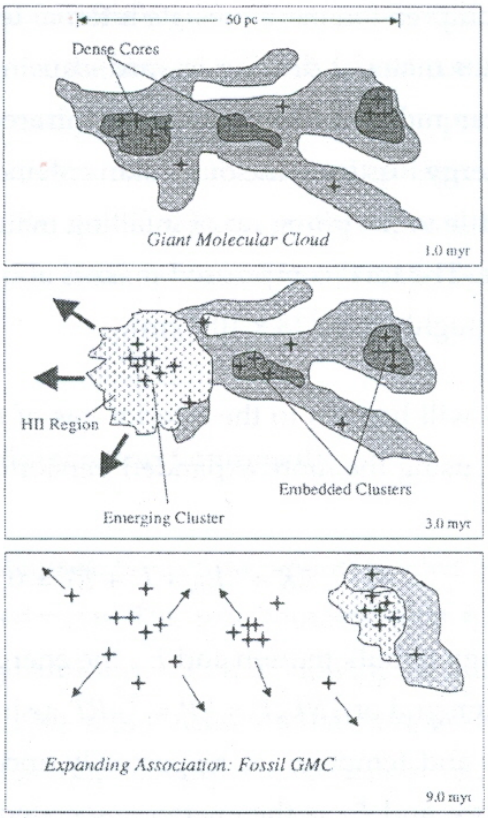

Figure 2.5: A schematic diagram illustrating the evolution of an OB association. From *Lada et al.* (1998).

systems (*Ho and Haschick*, 1981), where the binary counterpart can be either a low-mass star or a smaller massive star. Shown in Figure 2.4 is a schematic presentation of such an HMC embedded inside a molecular cloud. These HMCs exhibit extraordinary densities $\sim 10^6 - 10^9$ cm^{-3} (see e.g. *Osorio et al.*, 1999; *van der Tak*, 2004; *Nomura and Millar*, 2004; *Carroll and Ostlie*, 2007), and have temperatures of up to $\sim$ 300 K (for a temperature of $\sim$ 300 K it is believed that the star is already present). Due to the high column densities, the massive stars embedded within these HMCs are totally obscured from view, because all the light at near-infrared (near-IR) and optical wavelengths (*Hoare et al.*, 2007) is absorbed by the gas and dust.

2.4 Star formation and H II regions

Just as clusters are formed in dense cores by gravitational instabilities, massive stars are formed inside of HMCs. When HMCs start to collapse, a proto-stellar object is formed at the center called a proto-star (*González-Avilés et al.*, 2005). The collapse of this HMC is regulated by the Jeans criterion $M_c \geq M_J$, which states that if M_c, the mass of the cloud, is larger than M_J, the

Jeans mass, the cloud will collapse (*Carroll and Ostlie*, 2007). The Jeans mass is given by:

$$M_J \approx (\frac{5kT}{G\mu m_H})^{3/2}(\frac{3}{4\pi\rho_0})^{1/2}. \tag{2.1}$$

Here, G is the universal gravitational constant, μ is the mean molecular weight, m_H is the mass of one hydrogen atom, k is the Boltzmann constant, ρ_0 is the initial mass density, and T is the temperature. From this, follows that M_J is dependent on the temperature T of the cloud. However the temperature dependence is derived from the thermal energy (E_{th}) dependence as given by the Virial theorem (written in terms of energy), Which states that

$$2E_{th} + U = 0, \tag{2.2}$$

where U is the gravitational potential energy. Equation 2.2 states that thermal energy opposes gravitational collapse, thus if $M_c > M_J$ the thermal energy E_{th} would not be enough to keep the molecular cloud in equilibrium, and gravitational collapse can take place. However, the Jeans mass is also sensitive to rotation and magnetic fields.

In the following section, a brief discussion will also be given on the topic of the formation of massive stars from HMCs. The mass of the star depends on the properties of the accretion from the infalling envelope, as will be discussed next.

2.4.1 Early star formation of massive stars

After the gravitational collapse of the cloud core, the proto-stellar object begins to accrete gas from the envelope due to gravity, where this accretion is assumed to be spherically symmetric. When the proto-stellar object reaches a mass of $\sim 15\ M_\odot$, the star's hydrogen fusion is ignited in the core (see e.g. *Kratter et al.*, 2008). At approximately this mass the star reaches the zero-age main sequence (ZAMS). This causes the initiation of radiation (UV radiation) from the core. The accretion rate can be in the order of $\sim 10^{-4} - 10^{-3} M_\odot$ y^{-1} onto the star (*Osorio et al.*, 1999), where the star in this phase also has a high mass accretion flow of $\sim\ 10^{-4} M_\odot$ yr^{-1}. At the start of UV radiation from the core, the radiation causes a force to be exerted on the infalling envelope called radiation pressure. This pressure force works in the opposite direction of the inward gravitational force of the envelope.

As the stellar core accretes material, its luminosity (L) of the stellar core increases, as does the radiation pressure. This happens because as more mass is accreted, there is more material that can produce radiation, which increases the luminosity and the radiation pressure. However, the ratio of radiative force compared to the gravitational force will only exceed unity once the luminosity-to-mass-ratio reaches a value of $\sim\ 2500\ L_\odot/M_\odot$. Because of the opacity (κ_o with units cm^2/g) of the dusty envelope surrounding the proto star, this value is reached at a proto-stellar mass of $\sim 20\ M_\odot$ (*Krumholz et al.*, 2009), meaning that spherically symmetric accretion from the infalling envelope is supposed to halt at stellar masses near a value of ~ 20 M$_\odot$ due

to radiation. For higher stellar masses to form, it is believed that if rotation is included an accretion disk will form, partially shielding the gas from radiation (see e.g. *Krumholz et al.*, 2009, and references therein).

When the luminosity-to-mass ratio becomes greater than $\sim 2500\ L_{\odot}/M_{\odot}$, the radiation pressure starts to dominate the gravitational force. This leads to the outflow of gas along the polar axes (so-called bipolar outflows), inflating radiation-filled bubbles on both sides of the accretion disk (*Krumholz et al.*, 2009). This is the general set of events that leads to the formation of more massive stars.

2.4.2 Formation of H II regions

As mentioned before, at the ZAMS stage of evolution, UV radiation is initiated. This radiation begins to ionize the surrounding molecular gas by a process called photoionization. It is only the most massive stars that produce radiation near or beyond the Lyman limit. Radiation with these energies is able to ionize molecular hydrogen (H I) into H II (see e.g. *Lopez et al.*, 2010; *González-Avilés et al.*, 2005; *Hoare et al.*, 2007; *Krumholz and Matzner*, 2009), creating a radio free-free emission H II region around massive stars.

In the early stages of stellar evolution (t $\leq 5 \times 10^4$ years), when the stars are still deeply embedded inside their natal cloud (HMCs) with high densities, the H II region that forms is in most cases classified as an Ultra-compact H II (UCHII) region (See e.g. *Klessen et al.*, 2010; *Hoare et al.*, 2007). As the radiation from the star ionizes the surrounding gas, the ionized gas region becomes larger. The stellar winds that arise from the stellar surface push away the ionized gas from the star. This causes the UCHII region to expand to distances of ~ 0.1 pc, the edge of the HMC. This happens in $\sim 6 \times 10^4$ years (*González-Avilés et al.*, 2005). From there the HII region starts to evolve into the surrounding molecular clump in which the HMC was embedded. As these H II regions evolve, they become more and more diffuse, and near the end of the life of these massive stars, the H II regions around these stars are so large that they are called "giant H II" regions.

2.5 Stellar evolution

There are three important stages of stellar evolution, namely before, during and after the main sequence. The first phase (pre-main-sequence) follows the formation of the star from a cloud of interstellar material, through its gravitational contraction and subsequent heating, to the main sequence. The second phase, where the star spends most of its lifetime, is called the main-sequence (hydrogen burning) phase of the stellar evolution. The third phase (post-main-sequence) follows as an increasingly rapid evolution that begins when hydrogen burning has been exhausted in the stellar core (*Bowers and Deeming*, 1984).

The third stage can differ in the case of massive stars, depending on their initial mass M. The following diagram shows the evolutionary tracks of massive stars with an initial mass of more than 10 $M_\odot$ (see *Carroll and Ostlie*, 2007):

- 10 $M_\odot < M < 20M_\odot : O \rightarrow RSG \rightarrow BSG \rightarrow SN$
- 20 $M_\odot < M < 25M_\odot : O \rightarrow RSG \rightarrow WN \rightarrow SN$
- 25 $M_\odot < M < 40M_\odot : O \rightarrow RSG \rightarrow WN \rightarrow WC \rightarrow SN$
- 40 $M_\odot < M < 85M_\odot : O \rightarrow Of \rightarrow WN \rightarrow WC \rightarrow SN$
- $M > 85M_\odot : O \rightarrow Of \rightarrow LBV \rightarrow WN \rightarrow WC \rightarrow SN$

The different abbreviations are as follows, Red Super Giant (RSG), Blue Super Giant (BSG), Luminous Blue Variable (LBV), and the WN and WC are phases of Wolf Rayet stars where either nitrogen or carbon is the dominant fusion element, also Of stars are O super giants with pronounced emission lines, and SN is Supernova.

During this third phase, the star continually battles the force of gravitation, which will try to collapse the star. The star can halt this collapse temporarily during various stages, by fusion of nuclear material, and so maintaining a high enough internal temperature gradient necessary for support of the outer layers. Eventually the nuclear fusion material will be depleted, and the star will collapse further until the next nuclear fusion material can be ignited, or the collapse is halted by degeneracy, or some violent event. When there are no options left, the star will eventually dynamically collapse, causing an explosion. The result of this collapse is determined by its original mass, resulting in a white dwarf, supernova, neutron star or even a black hole (*Bowers and Deeming*, 1984).

2.6 Stellar winds and wind-blown bubbles

In the nuclear fusion phases of a star, it releases energetic particles from its surface. This phenomenon of blowing high velocity energetic particles away from the surface of a star is called Stellar Winds (SW). It was first seen by studying the orientation of comet tails, which always point away from the star, e.g. *Böhm-Vitense* (1989) (see also *Biermann*, 1951). In the late 1970s there were three existing stellar wind theories, namely: (a) Coronal models, (b) Radiative models, and (c) Hybrid models (as discussed by *Cassinelli*, 1979).

In the case of the coronal model (for stars that exhibit the existence of convection zones), the outer atmosphere expands as a wind because of the gas pressure gradient. This process is assumed to be similar to that producing the solar wind, but the solar wind of the Sun is created due to the magnetized nature of the corona that heats the plasma even more, causing the gas pressure to increase.

The second model is a Radiative model for very luminous stars. In early-type stars, transfer of photon momentum to the gas occurs through the opacity of the many strong resonance lines in the UV range. Radiative acceleration of the matter in the outer atmosphere can occur if there is sufficient opacity at wavelengths near flux maximum, and massive early-type stars are the only ones that can produce sufficient radiation in the Lyman range (flux maximum). The radiative force on the infrared continuous opacity of the grains can drive the dust and surrounding gas outward.

The third model uses a combination of both the coronal model and the radiative model to explain the formation of a stellar wind. *Cassinelli* (1979) suggested that the flow is initiated by gas pressure gradients in the corona and then accelerated to large velocities by the line acceleration mechanism.

For early-type very luminous stars, the stellar winds are driven by radiation pressure (radiative model). For the stellar winds of these very luminous stars, the theoretical work assumes steady, radial, spherically symmetric flow. With these assumptions taken into account, the fluid flow equations that express the conservation of mass, momentum, and energy of the gas can be written as

$$\dot{M} = 4\pi\rho v r^2 = const \tag{2.3}$$

$$v\frac{dv}{dr} + \frac{1}{\rho}\frac{dp}{dr} + \frac{GM}{r^2} + g_R = 0 \tag{2.4}$$

$$v\frac{de}{dr} + pv\frac{d}{dr}(\frac{1}{\rho}) = -(\frac{1}{\rho})(\nabla\cdot\mathbf{q}) = \frac{1}{\rho}(Q_A + Q_R - \nabla\cdot\mathbf{q}_c), \tag{2.5}$$

where ρ is the mass density, v is the radial speed, p is the gas pressure, e is the internal energy per unit mass, g_R is the radiation acceleration produced by radiation pressure. The heat added to the gas is represented by the divergence of the energy flux $\mathbf{q}$, and Q_A is the energy deposited per volume by acoustic or mechanical energy, Q_R is the rate of deposition of radiative energy, and $\mathbf{q}_c$ is the conductive flux (*Cassinelli*, 1979). These fluid equations, and a thorough discussion of the radiative terms, are derived by *Mihalas* (1978). *Holzer and Axford* (1970) also formulate these equations taking into account the mechanical energy deposition, and mass deposition.

The previous set of equations determines the hydrodynamic state of the stellar envelope (stellar surface). While the luminosity of the envelope is less then the Eddington luminosity (L_{Ed}) the star is in hydrostatic equilibrium. However, when the luminosity (L) of the envelope exceeds this luminosity, it is no longer in hydrostatic equilibrium, and must be accelerated outward. At this time, the radiation acceleration force also becomes greater than the gravitational force. The Eddington luminosity is:

$$L_{Ed} = \frac{4\pi c G M_\odot}{\overline{\kappa}}(\frac{M}{M_\odot})\frac{ergs}{sec}, \tag{2.6}$$

with, c the speed of light, G the universal gravitational constant, $\overline{\kappa}$ the mean opacity of the stellar envelope, and $M_{\odot}$ the mass of the star.

As mentioned before, when a star reaches a mass of $\sim 15\ M_{\odot}$ the UV radiation from the core is initiated. This causes the surrounding ISM material to become photo ionized, forming an H II region around the star. At the time the star reaches a mass of $\sim 20\ M_{\odot}$, the stellar material starts to escape from the stellar surface. This is caused by the radiation acceleration force that opposes gravity. As the star blows away its stellar material at hypersonic speeds relative to the ambient ISM (e.g. ~ 2000 km s^{-1}), a two-shock structure forms, as shown below in Figure 2.6 (*Arthur*, 2007). The first shock sweeps up the ISM material, accelerating, compressing and heating it (denoted by R_c in Figure 2.6), while the second shock, R_{s1}, decelerates the stellar wind, heating and compressing it.

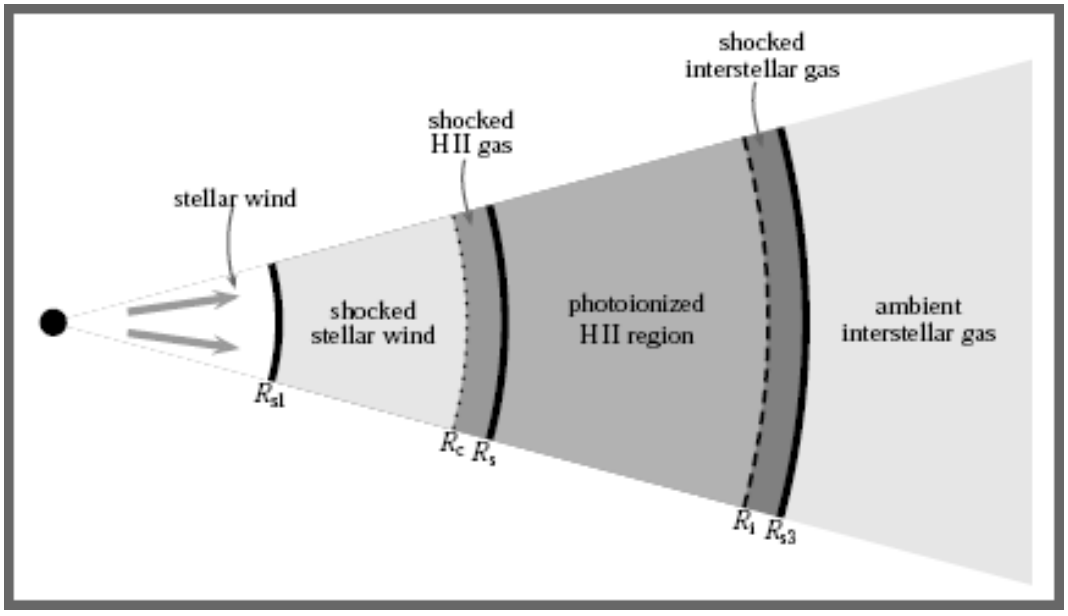

Figure 2.6: Schematic representation of the different regions that form due to a wind-blown bubble around a massive star. R_{s1} is the stellar wind shock (termination shock), R_s is the shock set up in the ambient medium, and R_{s3} is the isothermal shock sent out ahead of the ionization front that borders the H II region, while R_c is the contact discontinuity separating shocked stellar wind material from swept-up ambient medium and R_i marks the ionization front separating neutral and ionized gas. From *Arthur* (2007).

As shown in Figure 2.6, the region between the star and shock R_{s1} (decelerated stellar wind) is the region where the stellar material flows with hypersonic speeds. This flow is spherically symmetric and the density ρ of the stellar material decreases as $\rho \propto \frac{1}{r^2}$. The region between R_{s1} and R_c is known as the shocked stellar wind with a constant density due to incompressible subsonic flow. Lastly, the shock denoted by R_{s3} is the shock formed to separate the ionization front from the ambient ISM medium.

The material behind the shock R_s favours the rapid cooling of the swept-up shell of material, so that the shock becomes thin and dense, (e.g. *Falle*, 1975). The shocked stellar wind can, however, have temperatures $> 10^7$ K and thus does not efficiently cool. The hot, very low

density shocked stellar material pushes the cold, swept-up shell of material away. Because the shocked stellar material remains adiabatic, this is known as an "energy-driven" flow (*Arthur*, 2007).

2.7 Summary

In this chapter the main focus was to provide a background on how and where massive stars are formed. Firstly, a discussion was given of the structure and parameters of the surrounding ISM. This includes a small and large scale view of the ISM, which shows how the structure of the ISM can be sculptured by the energy and kinematic input of the supernova explosions. The density and temperature of these structures were also discussed, and a description of the interstellar magnetic field found in these regions was also given.

Different kinds of molecular clouds and the structures that can be found inside were also discussed. The conditions inside these clouds, such as density, temperature and their size were also mentioned. Secondly, different kinds of star-formation can take place inside these different clouds, whether its a cluster of stars, a binary system or a single massive star. However, in this work, an investigation into the evolution of a single massive star is of interest.

An overview was also offered on how single massive stars form from a hot molecular core (HMC). A proto-stellar object is formed due to gravitational instabilities, and accretes matter from the envelope surrounding it. As the matter accretes onto the proto-star, its mass increases. When the mass of the star reaches a value of $\sim 15\ M_{\odot}$, its radiation is initiated. Then as it reaches the mass of $\sim 20\ M_{\odot}$, the force that the radiation exerts on the stellar material becomes larger than the gravitational force, and the stellar material on the surface of the star cannot be held by the gravitational force anymore, and the stellar envelope must be accelerated outward.

In this work, different stellar wind cavities, corresponding to different mass-loss rates and outflow speeds are calculated. For this purpose, a hydrodynamic model is utilized, which is discussed in the next chapter.

Chapter 3

Numerics

3.1 Introduction

As mentioned in Chapter **1**, the heliospheric model of *Fahr et al.* (2000) and *Scherer and Ferreira* (2005) is used to simulate stellar winds. In this work, the stellar winds of massive stars, with the spectral type O and B, are of interest. The numerical model was originally developed to simulate the interaction of the solar wind and the local interstellar medium (LISM) to calculate the heliosphere (*Kausch*, 1998). The interaction can be described by a system of non-linear, partial differential equations, that most often do not present easily obtainable analytical solutions. To obtain useful results numerical algorithms are used to obtain approximate solutions. The aim of this chapter is to provide a brief overview of the numerical scheme that is used to calculate the results discussed in the following chapters.

This chapter starts out by looking at the most basic form of transport in a fluid, called the one-dimensional advection equation. Also shown in this chapter, is how complicated systems, like stellar winds, can be simplified and reduced to a series of one-dimensional advection equations that are easily solvable. This can be done numerically because any linear, constant coefficient hyperbolic system may be decoupled into a set of independent one-dimensional advection equations (*LeVeque*, 2002). From there it can be shown that for the specified case of the Euler equations, it is possible to approximate the system as being linear with constant coefficients within some localized volume. The numerics are already fully described in *LeVeque* (2002), *Kausch* (1998) and *Snyman* (2007). This chapter only summarizes some of their descriptions.

3.2 The advection equation and linear hyperbolic systems

The study of hydrodynamics of a system begins with considering the conserved quantities inside that system. The three most important quantities are: mass, momentum and energy. This implies that the mass, momentum and energy associated with a certain fluid volume may only change in the case of positive or negative fluxes at the boundary surfaces enclosing the system, or if there are sources present (*Snyman*, 2007; *LeVeque*, 2002). Mathematically, this

may be expressed (using the notation from *LeVeque*, 2002) for some quantity q in one spatial dimension as

$$\frac{d}{dt}\int_{x_1}^{x_2} q(x,t)dx = f(q(x_1,t)) - f(q(x_2,t)), \tag{3.1}$$

where x is the position, t the time and f the flux function dependent on the quantity q at some particular point in space and time. Equation 3.1 thus states the conservation of q in one spatial dimension, where the points x_1 and x_2 are the boundaries of the one-dimensional volume.

If it is assumed that q is continuous everywhere, then Equation 3.1 reduces to

$$\frac{\partial q(x,t)}{\partial t} + \frac{\partial f(q(x,t))}{\partial x} = 0 \tag{3.2}$$

If f is defined by $f = vq$, with v assumed to be constant everywhere and independent of q, Equation 3.2 yields the one-dimensional advection equation

$$q_t + vq_x = 0 \tag{3.3}$$

where the subscripts of Equation 3.3 denote partial differentiation. This equation permits solutions of the form $q(x,t) = \widehat{q}(x - vt)$. Therefore, for any direction for which $x - vt = C$, where C is a constant, the quantity $\widehat{q}(x - vt)$ remains constant. From $x - vt = C$ it follows that the velocity, with which $\widehat{q}(x - vt)$ propagates, is given by

$$\frac{dx}{dt} = v \tag{3.4}$$

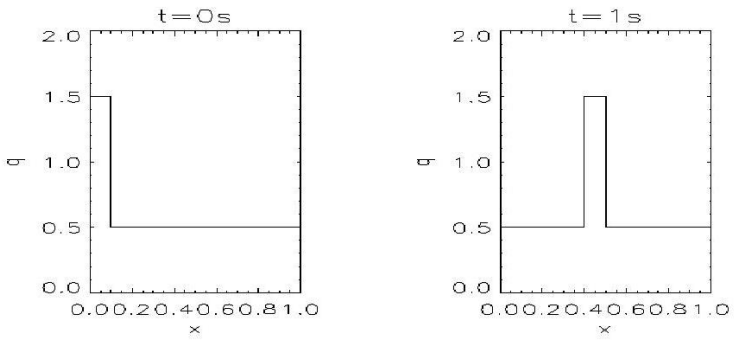

Figure 3.1: The solution to the advection equation. For a specified initial state $q(0,0)$ the state $q(0,t)$ at some later time t is merely the initial state propagated a distance vt from its initial position. From *Snyman* (2007).

In terms of fluid dynamics, this implies that some quantity is transported by the fluid without being changed by the fluid. By knowing the state of the quantity at some time t = 0s, the state of the quantity will still be the same at a later time t = 1s. This means that the whole initial

state just propagated in the direction of velocity v over a distance of Δtv, where Δt is the time between the two instants as illustrated by Figure 3.1.

The advection equation is a useful tool in finding solutions to more complex problems. An example of such a problem is the case of a linear system of m hyperbolic partial differential equations. This system can be decoupled into a set of m independent advection equations. Each of these independent equations has its own solution. By definition a constant coefficient linear system of m equations

$$q_t + Aq_x = 0 \tag{3.5}$$

where

$$q = \begin{bmatrix} q_1 \\ q_2 \\ . \\ . \\ q_m \end{bmatrix} A = \begin{bmatrix} A_{11} & A_{12} & ... & A_{1m} \\ A_{21} & A_{22} & ... & A_{2m} \\ . & . & & . \\ . & . & . & . \\ A_{m1} & A_{m2} & ... & A_{mm} \end{bmatrix} \tag{3.6}$$

is hyperbolic if the $m \times m$ matrix A has real eigenvalues and is diagonalizable. If A is diagonalizable it implies that there exists a matrix R that is invertible, so that $R^{-1}AR$ is a diagonal matrix, where R^{-1} denotes the inverse of R. Real eigenvalues imply that a set of m eigenvectors r^p exists together with m real eigenvalues λ^p (*LeVeque*, 2002) so that

$$Ar^p = \lambda^p r^p \quad for \quad p = 1, 2, ..., m. \tag{3.7}$$

Subsequently, A is diagonalised by

$$R^{-1}AR = \Lambda \tag{3.8}$$

where

$$\Lambda = \begin{bmatrix} \lambda^1 & 0 & ... & 0 \\ 0 & \lambda^2 & ... & 0 \\ . & . & & . \\ . & . & . & . \\ 0 & 0 & ... & \lambda^m \end{bmatrix} \tag{3.9}$$

and R is the $m \times m$ matrix

$$R = \left[r^1 | r^2 | ... | r^m\right] \tag{3.10}$$

with the set of m eigenvectors r^p, $p = 1, 2, ..., m$ being the columns of A. Equation 3.5 can now be decoupled into m advection equations by multiplying with the inverse R^{-1} of R and noting that $RR^{-1} = I$, where I is the identity matrix. When Equation 3.5 is multiplied by the identity matrix I, this yields

$$R^{-1}q_t + R^{-1}ARR^{-1}q_x = 0 \tag{3.11}$$

Setting $\omega = R^{-1}q$, and using Equation 3.8, m independent advection equations

$$\omega_t + \Lambda\omega_x = 0 \tag{3.12}$$

are obtained, if R is not explicitly dependent on either x or t. Furthermore, the p'th equation may be written as

$$\omega_t^p + \lambda^p\omega_x^p = 0 \quad for \quad p = 1, 2, ..., m \tag{3.13}$$

where the p'th flux is given by $f^p = \lambda^p\omega^p$ just like in the case of the advection equation, Equation 3.3.

The decoupling of these linear hyperbolic equations into their independent advection equations gives a hint as to developing methods for non-linear hydrodynamics. If one could define some fluid volume as approximately linear, one might be able to approximately describe the dynamics inside such a volume, by a finite set of advection equations (*LeVeque*, 2002). The key to this approach is the Riemann problem, that will be considered next.

3.3 Finite volume methods for linear systems

In the case of non-linear hyperbolic differential problems, even though initial data may be continuous, shock waves and contact discontinuities may form in some cases at later times. In the event of the formation of one or both of these structures, the equation of conservation, Equation 3.2, cannot hold, since it assumes a continuous state $q(x, t)$ for all x and t. However, the integral form of Equation 3.2 makes no such assumptions regarding continuity. Therefore, in developing numerical methods using finite volumes (based on Equation 3.1), issues of continuity are sidestepped (*LeVeque*, 2002).

The first step one should take to implement, is to subdivide the domain over which the initial data extend into several cells (volumes) and average the data within each cell. For example, in one dimension the i'th cell C_i is centered around x_i with boundaries at $x_i - \frac{1}{2}$ and $x_i + \frac{1}{2}$. In the first order approximation, the state $q(x, t_n)$ at time $t = t_n$ in each cell is averaged according to

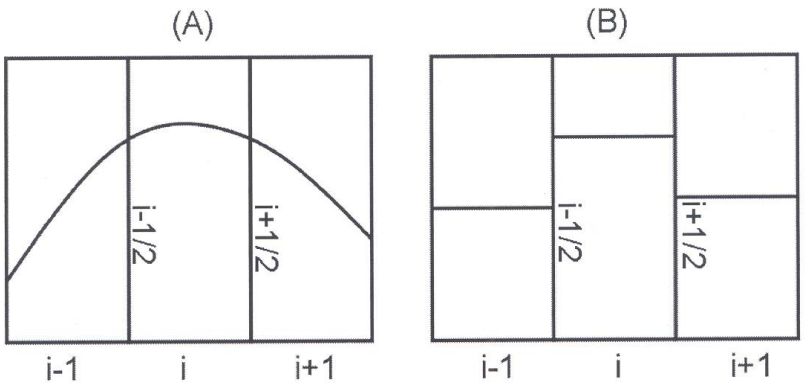

Figure 3.2: Continuous data (A) and volume averaged discrete data (B). From *Snyman* (2007).

$$Q_i^n = \frac{1}{\Delta x} \int_{C_i} q(x, t_n) dx \tag{3.14}$$

where Δx is the cell dimension and integration over the volume C_i implies integration over the range Δx. In the limit $\Delta x \to 0$, $Q_i^n \to q(x_i, t_n)$. The process of cell-averaging is illustrated in Figure 3.2, where some quantity in (A) is averaged according to Equation 3.14 to obtain piecewise constant data (B).

3.4 The one-dimensional Euler equations

The standard form of the one-dimensional Euler equations is expressed as

$$\begin{bmatrix} \rho \\ \rho v \\ E \end{bmatrix}_t + \begin{bmatrix} \rho v \\ \rho v^2 + P \\ (E + P)v \end{bmatrix}_x = 0 \tag{3.15}$$

where ρ is the density, v the bulk velocity, P the pressure and E the energy density associated with the fluid at a point in space and time. Subscripts indicate partial differentiation as before. The system is non-linear because quantities ρ, v, P and E are interdependent. By considering an equation of state that links the previously mentioned quantities, it can be simplified in some way. In this case, the equation of state for an ideal gas is

$$P = R\rho T, \tag{3.16}$$

where R is the universal gas constant divided by the molecular weight of the gas. If one assumes that the internal energy of the fluid is only dependent on the fluid temperature, the relation

$$e = c_v T \tag{3.17}$$

holds where e is the energy per unit mass of the fluid and c_v the specific heat at constant volume. If one also assumes that the particles that make up the fluid only have three translational degrees of freedom (i.e. monatomic), then from the equipartition theorem, the energy is given by

$$e = \frac{3}{2} nkT, \tag{3.18}$$

with $nk = R$. It then follows that

$$c_v = \frac{3}{2} R, \tag{3.19}$$

and by using this in the relation between the specific heats at constant volume and pressure, which is given by

$$c_p - c_v = R, \tag{3.20}$$

it follows that

$$c_p = \frac{5}{2} R. \tag{3.21}$$

The ratio of specific heats is therefore given by

$$\gamma = \frac{c_p}{c_v} = \frac{5}{3}. \tag{3.22}$$

From Equation 3.17 using $T = P/R\rho$ the internal energy is expressed as

$$e = \frac{c_v P}{R\rho} = \frac{P}{(\gamma - 1)\rho}. \tag{3.23}$$

The total energy density of the fluid is given by the sum of the energy per unit mass of each particle and the kinetic energy of the fluid, therefore

$$E = \rho e + \frac{1}{2}\rho v^2 = \frac{P}{\gamma - 1} + \frac{1}{2}\rho v^2. \tag{3.24}$$

The equation of state allows for the expression of the total energy in terms of ρ and P. Using this expression for the total energy, the Euler equations for an ideal gas (from *LeVeque*, 2002) are:

$$\begin{bmatrix} \rho \\ \rho v \\ E \end{bmatrix}_t + \begin{bmatrix} \rho v \\ \rho v^2 + P \\ (\frac{1}{\gamma-1}P + \frac{1}{2}\rho v^2)v \end{bmatrix}_x = 0. \tag{3.25}$$

The Euler equations are now in a form similar to that of Equation 3.5. In general, a non-linear system such as $q(x,t)_t + f(q(x,t))_x$ can be written in the so-called quasi-linear form given by

$$q_t + f'(q)q_x = 0, \tag{3.26}$$

where the notation $\frac{df}{dq} = f'(q)$ is used and $f'(q)$ is called the flux-Jacobian of the system. For

$$q = \begin{bmatrix} \rho \\ \rho v \\ E \end{bmatrix} \tag{3.27}$$

$f'(q)$ is computed as (*LeVeque*, 2002):

$$f'(q) = \begin{bmatrix} 0 & 1 & 0 \\ \frac{1}{2}(\gamma-3)v^2 & (3-\gamma)v & \gamma-1 \\ \frac{1}{2}(\gamma-1)v^3 - vH & H-(\gamma-1)v^2 & \gamma v \end{bmatrix}, \tag{3.28}$$

where $H = \frac{E+P}{\rho}$ is the total specific enthalpy. The eigenvalues of $f'(q)$ are

$$\lambda^1 = v - c, \quad \lambda^2 = v, \quad \lambda^3 = v + c \tag{3.29}$$

where c is the local speed of sound, defined as

$$c = \sqrt{\frac{\gamma P}{\rho}} = \sqrt{(\gamma-1)(H - \frac{1}{2}v^2)}. \tag{3.30}$$

The three eigenvalues in Equation 3.29 correspond to three eigenvectors

$$r^1 = \begin{bmatrix} 1 \\ v-c \\ H-vc \end{bmatrix} \quad r^2 = \begin{bmatrix} 1 \\ v \\ \frac{1}{2}v^2 \end{bmatrix} \quad r^3 = \begin{bmatrix} 1 \\ v+c \\ H+vc \end{bmatrix}. \tag{3.31}$$

Using the eigenvalues and eigenvectors of the flux-Jacobian allows for a numerical solution to the Euler equations based on the finite volume method discussed in the previous section. By subdividing initial data into cell averaged quantities it is ensured that the values of ρ, ρv and E are constant within each cell during a time step Δt. Therefore, the flux within each cell is also constant over the same interval implying that the Euler equations within each cell may be approximated as a constant coefficient, linear system.

3.5 Summary

In this chapter, the numerical method was briefly summarized. By using the one-dimensional advection equation, a numerical method for solving the multi-dimensional Euler equations (summarized in Equation 3.25) can be obtained. The method subdivides the initial state of a specific problem into finite volumes and then calculates the averages inside these volumes to approximate the state of the system within each volume. The system can then be approximated as a constant coefficient linear hyperbolic system. This is achieved by rewriting the Euler-equations as a quasi-linear system (Equation 3.25) and linearizing the resulting flux-Jacobian at the border of each volume (each cell interface). Since an m-dimensional constant coefficient linear hyperbolic system can be described in terms of m independent advection equations the properties of the advection equation can now be used to solve the Euler-equations numerically. This is done by providing fluxes at each cell interface which affects the averaged quantity within each volume (cell).

The method described in this chapter is now applied to the specific problem of the stellar wind and interstellar medium (ISM) interaction, which is the topic of the next chapters.

Chapter 4

Stellar winds I

4.1 Introduction

As mentioned in Chapter **1**, the model used in this work was previously applied to model the heliosphere (e.g. *Scherer and Ferreira*, 2005; *Ferreira et al.*, 2007a; *Snyman*, 2007). It was used to determine the state of the heliosphere under a variety of different conditions of the solar wind and interstellar medium (ISM), taking into account protons, neutral hydrogen and pick-up ions (PUIs) as different fluids. Also included by these authors was the kinematic calculation of the heliospheric magnetic field, and cosmic ray transport within the heliosphere.

In this chapter, this model is now applied to calculate the evolution of a stellar wind in the ambient undisturbed ISM. First it is assumed that this wind is stationary relative to the ISM (see Chapter 5 where a relative motion is included), and for the first attempt only a one-fluid scenario is considered where it is assumed that the effect of neutral hydrogen and PUIs may not be as pronounced due to the large dimensions of some cavities compared to the heliosphere. A detailed parameter study of the stellar wind evolution of O- and B-type stars is done and the results are presented in addition to a comparison with those obtained by *Arthur* (2007).

4.2 Density profiles of stellar winds

Figure 4.1 (from *Arthur*, 2007) shows an example of a computed stellar wind density profile of a 40 $M_{\odot}$ star where $\dot{M}$ = 9.1 $\times$ 10^{-6} $M_{\odot}$ y^{-1}, the mass-loss rate of the star, and v = 890 km s^{-1} is the speed of the stellar wind, which may also be referred to as the outflow speed. This figure shows both the total and the ionized number density profiles. The total number density profile is the density profile of both the ionized and neutral molecules, whereas the ionized density profile is just the ionized molecules. It also shows that the total number density decreases as the distance from the star increases. This is the case for supersonic spherical outflow where the density ρ is inversely proportional to r^2 (just as for the solar wind), meaning that

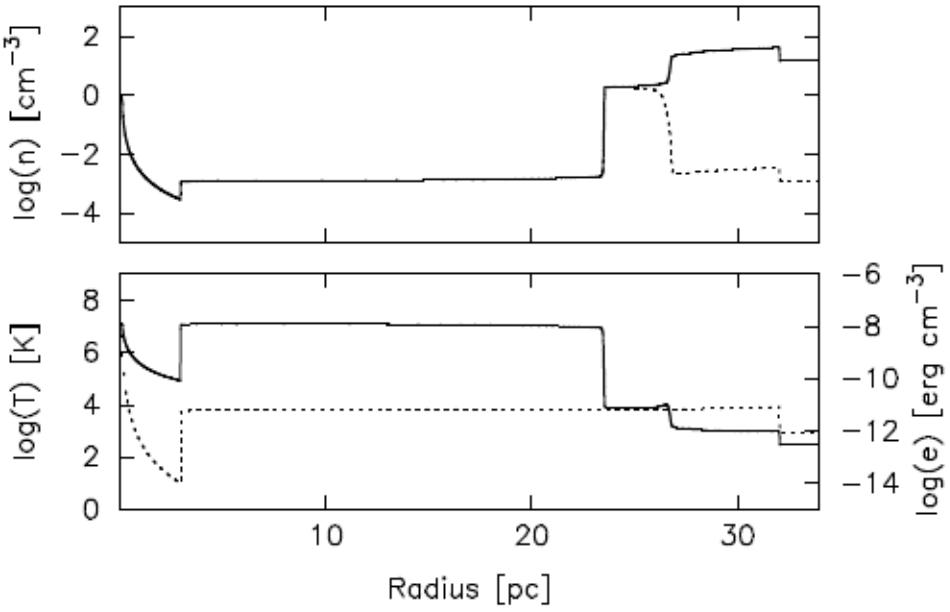

Figure 4.1: The computed density (top) and temperature (bottom) profile of a stellar wind around a 40 $M_\odot$ star near the end of its main-sequence stage (4×10^6 yrs). Top panel: total number density (solid line) and ionized number density (dotted line). Bottom panel: temperature (solid line) of the neutral particles and temperature of the ionized particles (dashed line). Stellar parameters: $\dot{M}$ = 9.1 $\times$ $10^{-7} M_\odot$ yr^{-1} , v = 890 km s^{-1}, ambient density ρ = 12 g cm^{-3} and temperature T = 200 K. From *Arthur* (2007).

$$\rho \propto \frac{1}{r^2}, \tag{4.1}$$

where r is the distance from the star. The density decreases up to a point. At this point, the ram pressure (pressure due to the momentum of the particles) of the stellar material becomes equal to the pressure exerted by the ISM on the stellar material. When this happens, the stellar material is rapidly decelerated, which causes a sudden increase in density and leads to the compression of the stellar material. This compression is known as a shock, which in this work will be called the termination shock (TS) of the stellar wind similar to the expression used for the heliosphere.

As the stellar material gets shocked it flows with subsonic speeds in the post-shock flow. As the shocked material flows outward, pre-shocked stellar material still flows towards the TS at supersonic speeds. This causes the next wave of stellar material to be shocked before the shocked material can flow away. This "pile-up" of stellar material just behind the shock gives rise to incompressible flow and a constant density profile is expected, as shown in Figure 4.1.

If v is the speed of the shocked stellar wind material, then from the continuity equation

$$\frac{\partial \rho}{\partial t} + \rho(\nabla \cdot \vec{v}) = 0. \tag{4.2}$$

If the density, ρ, does not change with time

$$\frac{\partial \rho}{\partial t} = 0, \tag{4.3}$$

meaning that ρ is constant, which then implies $\nabla \cdot \vec{v} = 0$. This is the condition for incompressible flow. This region of the stellar wind, where $\nabla \cdot \vec{v} \approx 0$, is known as the Astrosheath (AS), and material here may be reffered to as post-shocked, with pre-shocked material referring to that inside the shock moving with supersonic speeds.

Note that for the supersonic flow $\nabla \cdot \vec{v} > 0$, meaning the material is adiabatically expanding. At the shock $\nabla \cdot \vec{v} < 0$, which may lead to acceleration of particles (e.g. cosmic rays) to higher energies via diffusive shock acceleration (e.g. *Axford et al.*, 1977; *Bell*, 1978a,b; *Blandford and Ostriker*, 1978). Note that in a multi-fluid description, different fluids may interact, e.g. compression due to charge exchange between ionized and neutral particles (e.g. *Fahr et al.*, 2000). This may result in $\nabla \cdot \vec{v} < 0$ in the AS and adiabatic heating may occur in this region (e.g. *Ferreira et al.*, 2007b).

Figure 4.1 shows a second (from the origin outward) increase in density at $\sim$ 25 pc. This is known as the Astropause (AP), and it is the transition between the ISM and the stellar material. These two species of material do not mix because they have the same pressure on both sides of the AP. Another jump in the density profile is visible further out, which is a bow-shock and may occur if the relative motion is supersonic. However, in this work only the AP and the TS distance is studied and presented. This is to understand the evolution of these structures and the sensitivity of their radii on different parameters like outflow speed, mass-loss rate and ISM density.

4.2.1 Density profiles for stellar wind evolution into the ambient ISM

The heliospheric model used by (e.g. *Scherer and Ferreira*, 2005; *Ferreira and Scherer*, 2006) and *Snyman* (2007) has an inner boundary at the vicinity of Earth. Here the density and the speed of the solar wind are accurately known from *in situ* observations done by spacecraft orbiting the Earth and also those in the inner heliosphere, such as the Ulysses spacecraft. For the case of stellar winds, as calculated in this work, the grid steps need to be much larger compared to the case where the heliosphere is calculated and the inner boundary is therefore assumed at a much larger radial distance, of 0.05 pc and the outer boundary at a distance of 100 pc. There are 2000 gripsteps thus each gripstep has a value of 0.05 pc. This is because the scale of stellar winds simulated in this work is in the order of pc, compared to the heliopshere where it is in the order of AU. The density of the stellar wind at the inner boundary is calculated from knowing the mass-loss rate of the star and assuming $\rho \propto \frac{1}{r^2}$ to relate values at the inner boundary to those at the surface of the star.

The mass-loss rate of O- and B-type stars that is used in this model is in the order of 10^{-5}-10^{-6} $M_\odot$ y^{-1}. These values are inside the range of mass-loss rates given by *Chiosi and Nasi* (1974), *de Loore et al.* (1977) and *Lozinskaya* (1982). From *Bernabeu et al.* (1989) it follows that these massive

stars with high mass-loss rates (compared to the Sun) also have very high stellar wind speeds (compared to the solar wind) in the order of $\sim$ 1000 - 3000 km s^{-1}. Note that for the Sun the mass-loss rate is $\sim 10^{-14}$ M$_\odot$ y^{-1} and the solar wind speed $\sim$ 400 km s^{-1}.

Table 4.1: Parameters assumed in the model to calculate the stellar wind - ISM interaction in the ambient ISM

Model	$\dot{M}$ ($M_\odot$ y^{-1})	v (km s^{-1})	ρ_{ISM} (g cm^{-3})
1	10^{-5}	1000	10^{-24}
2	10^{-5}	2000	10^{-24}
3	10^{-5}	3000	10^{-24}
4	10^{-5}	1000	10^{-25}
5	10^{-5}	2000	10^{-25}
6	10^{-5}	3000	10^{-25}
7	10^{-5}	1000	10^{-23}
8	10^{-5}	2000	10^{-23}
9	10^{-5}	3000	10^{-23}
10	5×10^{-6}	1000	10^{-24}
11	5×10^{-6}	2000	10^{-24}
12	5×10^{-6}	3000	10^{-24}
13	5×10^{-6}	1000	10^{-25}
14	5×10^{-6}	2000	10^{-25}
15	5×10^{-6}	3000	10^{-25}
16	5×10^{-6}	1000	10^{-23}
17	5×10^{-6}	2000	10^{-23}
18	5×10^{-6}	3000	10^{-23}
19	10^{-6}	1000	10^{-24}
20	10^{-6}	2000	10^{-24}
21	10^{-6}	3000	10^{-24}
22	10^{-6}	1000	10^{-25}
23	10^{-6}	2000	10^{-25}
24	10^{-6}	3000	10^{-25}
25	10^{-6}	1000	10^{-23}
26	10^{-6}	2000	10^{-23}
27	10^{-6}	3000	10^{-23}

Table 4.1 shows different scenarios of parameters as assumed in the model and used in this work to calculate the interaction of a stellar wind with the ISM. Shown in column 1 are the different scenarios indicated as models 1-27. Column 2 lists the different mass-loss rates ($\dot{M}$) in units M$_\odot$ y^{-1}, column 3 gives the outflow speed v in units of km s^{-1} and in column 4 the ISM density ρ_{ISM} in units of g cm^{-3} is given. As shown in Table 4.1, the first nine scenarios correspond to a mass-loss rate of 10^{-5} M$_\odot$ y^{-1} assumed in the model, the second set of nine scenarios corresponds to a mass-loss rate of 5×10^{-6} M$_\odot$ y^{-1} and the third set of nine scenarios corresponds to a mass-loss rate of 10^{-6} M$_\odot$ y^{-1} assumed in the model.

Next, radial density profiles similar to Figure 4.1 are presented at different times and for each of the 27 scenarios shown in Table 4.1. Figure 4.2 shows these computed density profiles corresponding to a mass-loss rate of 10^{-5} M$_\odot$ y^{-1} (models 1-9) assumed in the model. Figure 4.3 corresponds to a mass-loss rate of 5×10^{-6} M$_\odot$ y^{-1} (models 10-18) and for Figure 4.4 a mass-loss rate of 10^{-6} M$_\odot$ y^{-1} (models 19-27) is assumed in the model with ρ_{ISM} and v varied as shown in Table 4.1.

Starting with a mass-loss rate of 10^{-5} $M_\odot$ y^{-1}, Figure 4.2 shows the computed density profiles of the first nine stellar wind scenarios from Table 4.1. The columns denote different ISM densities (ρ_{ISM}) and the rows denote different stellar wind speeds assumed in the model. The left column corresponds to ρ_{ISM} = 10^{-24} g cm^{-3}, the middle column to ρ_{ISM} = 10^{-25} g cm^{-3} and the right column to ρ_{ISM} = 10^{-23} g cm^{-3}. Note that these are not in increasing/decreasing order. The first (top) row corresponds to outflow speeds of v = 1000 km s $^{-1}$, the second (middle) row to v = 2000 km s^{-1} and third (bottom) row to v = 3000 km s^{-1}. Therefore, the outflow speed increases from top to bottom.

Shown in Figure 4.2 is that the computed density profiles have the same structure as appears in Figure 4.1, meaning the proportionality of $\rho \propto \frac{1}{r^2}$ for the supersonic flow, a shock with a sudden increase in density in the order of a factor ~ 4 and then a constant density for the post-shocked flow. This constant density suddenly increases at the AP, the transition region where the ISM and shocked stellar wind is separated.

Different lines in Figure 4.2 show different simulation times at 50, 150, 300, 500, 700 and 900 $\times 10^3$ y respectively, meaning years after the simulation started with a wind blowing from the inner boundary in the model out into the undisturbed ISM. Clearly visible is how the AP expands into the ISM as time increases. Next, the different scenarios are discussed and comparisons are made.

From the middle row (panels b, e and h) of Figure 4.2 it follows that the ISM density plays an important role in the structure and evolution of the stellar wind. Panel (b) shows the computed density profile for ρ_{ISM} = 10^{-24} g cm^{-3}, panel (e) for ρ_{ISM} = 10^{-25} g cm^{-3} and panel (h) for ρ_{ISM} = 10^{-23} g cm^{-3} assumed in the model. All have a stellar wind outflow speed of 2000 km s^{-1} and mass-loss rate of 10^{-5} $M_\odot$ y^{-1}. Shown here is that increasing (or decreasing) the ISM density, the distance at which the TS and AP are formed, decreases (or increases). This is due to the increase (or decrease) of the pressure of the ISM.

For the middle column (panels d, e and f) of Figure 4.2 it follows that increasing (or decreasing) the stellar wind speed from 1000 km s^{-1} (panel d) to 2000 km s^{-1} (panel e) to 3000 km s^{-1} (panel f) (keeping both the ISM density and the stellar mass-loss rate constant) also increases (or decreases) the distance to the TS and AP, due to the increase (or decrease) of the stellar wind momentum. This is more quantitatively discussed next.

By comparing the different panels in Figure 4.2 to each other it follows that changing the stellar wind speed, v, from 1000 km s^{-1} (panel d) to 3000 km s^{-1} (panel f), a factor of 3 increase leads to an increase in the cavity blown out by the stellar wind, e.g. from $\sim$ 24 pc to $\sim$ 76 pc respectively after a simulation time of 500 $\times$ 10^3 y . This corresponds to an increase of a factor $\sim$ 3.0. As for the shock, this distance increases from $\sim$ 6 pc to $\sim$ 21 pc, corresponding to an increase of a factor $\sim$ 3.5 when v is tripled. As for both the shock and the AP after a simulation time of 900 $\times$ 10^3 y, the shock increases from $\sim$ 6 pc to $\sim$ 43 pc, corresponding to an increase of a factor $\sim$ 7.2. However, the AP runs out of the grid, which is limited to 100 pc.

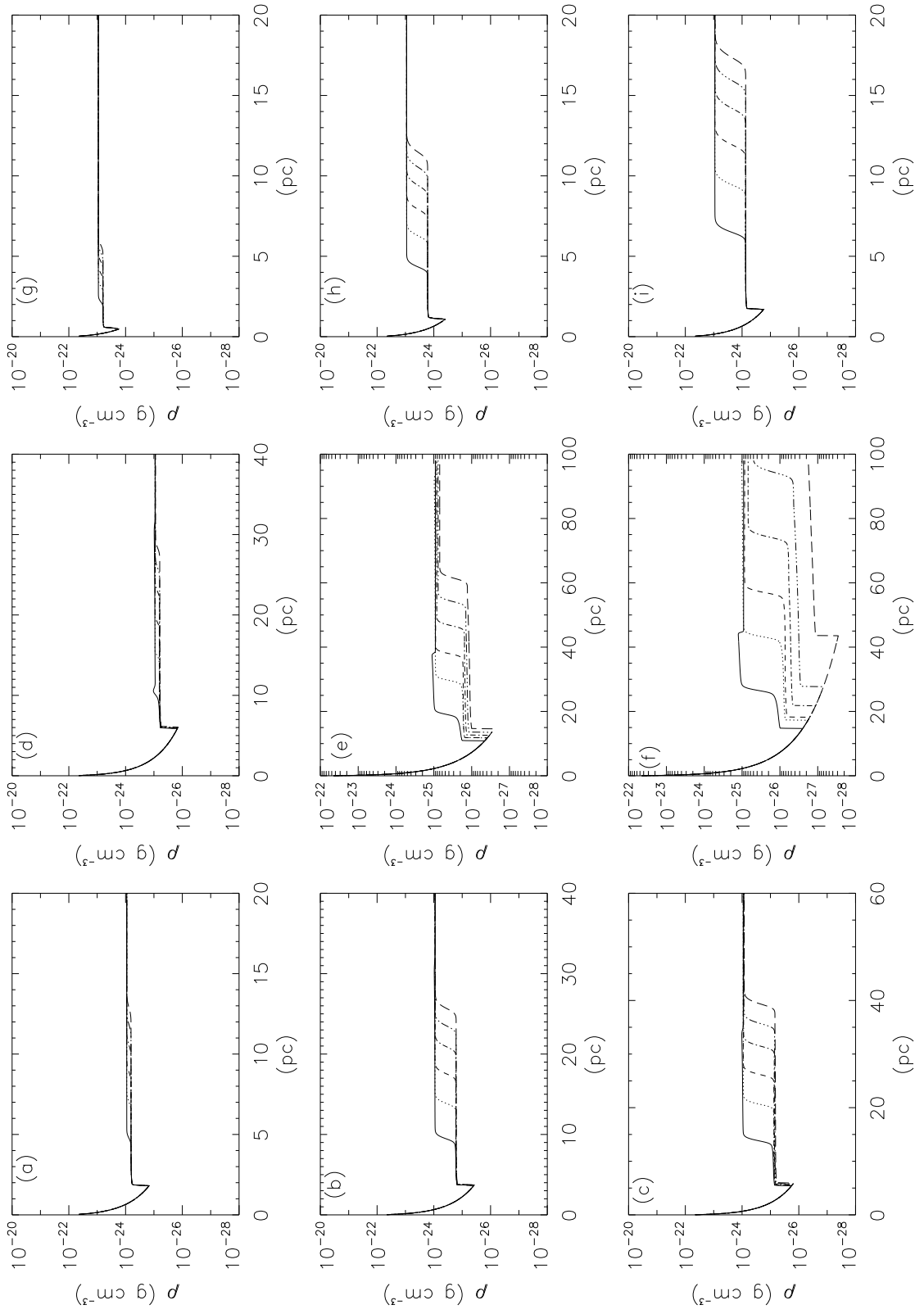

Figure 4.2: The computed density profiles (where the density is on a log scale) of a stellar wind for 9 different configurations. The stellar mass-loss rate is assumed constant (with a rate of 10^{-5} $M_{\odot}$ yr^{-1}), while the ISM density ρ_{ISM} and stellar wind speed v are varied. In column 1, results are shown corresponding to ρ_{ISM} 10^{-24} g cm^{-3}, in column 2 $\rho_{ISM} = 10^{-25}$ g cm^{-3} and in column 3 $\rho_{ISM} = 10^{-23}$ g cm^{-3}. In row 1, the stellar wind speed is assumed constant with a value v = 1000 km s^{-1}, row 2 v = 2000 km s^{-1} is assumed and for row 3 v = 3000 km s^{-1}. Also shown in each of these panels are 6 different time steps in the stellar wind evolution, namely 50, 150, 300, 500, 700 and 900 $\times 10^3$ y as the different lines respectively. Each panel is identified by the letter in the top left corner. Letters (a-i) correspond to models 1-9 in Table 4.1.

From row (2) it follows that changing ρ_{ISM} from ρ_{ISM} = 10^{-23} g cm^{-3} (panel h) to ρ_{ISM} = 10^{-25} g cm^{-3} (panel e) leads to an increase in the cavity blown out by the stellar wind with a speed of 2000 km s^{-1}, e.g. from $\sim$ 10 pc to $\sim$ 48 pc respectively after a simulation time of 500 $\times$ 10^3 y. This corresponds to an increase of a factor of $\sim$ 4.8. In the case of the shock, for the same simulation time, it increased from $\sim$ 1.2 pc to $\sim$ 12 pc corresponding to an increase of a factor of $\sim$ 10. For a simulation time of a 900 $\times$ 10^3 y, the AP increased from $\sim$ 13 pc to $\sim$ 65 pc, corresponding to an increase of a factor of $\sim$ 5, while the shock increased from $\sim$ 1.2 pc to $\sim$ 14 pc, corresponding to an increase of a factor of $\sim$ 12 when ρ_{ISM} was decreased by a factor of a 100.

Figure 4.3 shows the same computed profiles as in Figure 4.2 however, in Figure 4.3 the stellar mass-loss rate is changed from 10^{-5} M$_\odot$ yr^{-1} to 5 $\times$ 10^{-6} M$_\odot$ yr^{-1}. Column 1 (left) again corresponds to ρ_{ISM} = 10^{-24} g cm^{-3} in the model, column 2 (middle) to ρ_{ISM} = 10^{-25} g cm^{-3} and column 3 (right) to ρ_{ISM} = 10^{-23} g cm^{-3} assumed in the model. As for the rows, the first row again corresponds to calculations assuming a stellar wind speed v = 1000 km s^{-1}, the second row to v = 2000 km s^{-1} and the third row to v = 3000 km s^{-1}.

Shown here is that for this mass-loss rate (5 $\times$ 10^{-6} M$_\odot$ yr^{-1}), changing the stellar wind speed from 1000 km s^{-1} (panel d) to 3000 km s^{-1} (panel f) (while keeping ρ_{ISM} = 10^{-25} g cm^{-3} constant) also leads to an increase in the computed cavity blown out by the stellar wind. The AP distance increased from $\sim$ 18 pc to $\sim$ 58 pc after a simulation time of 500 $\times$ 10^3 y. This corresponds to an increase of a factor $\sim$ 3.2 when v is tripled. The shock distance increased from $\sim$ 4 pc to $\sim$ 13 pc, corresponding to an increase of a factor of $\sim$ 3.3. These factor increases are very similar to Figure 4.2 where the mass-loss rate was higher. For a simulation time of 900 $\times$ 10^3 y, the AP increased from $\sim$ 20 pc to $\sim$ 84 pc, corresponding to an increase of a factor of $\sim$ 4.2. The shock increased from $\sim$ 4 pc to $\sim$ 16 pc, corresponding to an increase of a factor of $\sim$ 4.0 when v is tripled.

From row (2) it follows that changing ρ_{ISM} from ρ_{ISM} = 10^{-23} g cm^{-3} (panel h) to ρ_{ISM} = 10^{-25} g cm^{-3} (panel e) again leads to an increase in the cavity blown out by the stellar wind with a speed of 2000 km s^{-1}, e.g. from $\sim$ 8 pc to $\sim$ 37 pc after a simulation time of 500 $\times$ 10^3 y for the AP. This corresponds to an increase of a factor of $\sim$ 4.7. As for the shock after the same simulation time, it increased from $\sim$ 0.8 pc to $\sim$ 8 pc, corresponding to an increase of a factor of $\sim$ 10. The AP, after a simulation time of 900 $\times$ 10^3 y, increased from $\sim$ 10 pc to $\sim$ 48 pc, corresponding to an increase of a factor of $\sim$ 4.8, and as for the shock, it increased from $\sim$ 0.8 pc to $\sim$ 8 pc, corresponding to an increase of a factor of $\sim$ 10 when ρ_{ISM} was decreased by a factor of 100.

Figure 4.4 also shows computed density profiles (as Figure 4.2 and Figure 4.3), but in this case the stellar mass-loss rate is lowered further to 10^{-6} M$_\odot$ y^{-1}. Again the left column shows the profiles for ρ_{ISM} = 10^{-24} g cm^{-3}, the middle column corresponds to ρ_{ISM} = 10^{-25} g cm^{-3} and the right column corresponds to ρ_{ISM} = 10^{-23} g cm^{-3}. The rows correspond to different stellar wind speeds, where for the first row a stellar wind speed of 1000 km s^{-1} is assumed, for the

second a speed of 2000 km s^{-1} and for the third row a speed of 3000 km s^{-1} is assumed in the model.

From Figure 4.4 it also follows that changing the stellar wind speed from 1000 km s^{-1} (panel d) to 3000 km s^{-1} (panel f) (keeping ρ_{ISM} = 10^{-25} g cm^{-3}) also leads to an increase in the cavity blown out by the stellar wind, from $\sim$ 11 pc to $\sim$ 34 pc after a simulation time of 500 $\times$ 10^3 y for the AP. This corresponds to an increase of a factor of $\sim$ 3.0. The shock increased from $\sim$ 2 pc to $\sim$ 6 pc, corresponding to an increase of a factor of $\sim$ 3.0 when v is tripled. For a simulation time of 900 $\times$ 10^3 y, the shock increased from $\sim$ 2 pc to $\sim$ 6 pc, corresponding to an increase of a factor of $\sim$ 3.0. The same applies for the AP increasing from $\sim$ 14 pc to $\sim$ 42 pc, corresponding to an increase of a factor of $\sim$ 3.0.

From row (2) it follows that decreasing the ρ_{ISM} from ρ_{ISM} = 10^{-23} g cm^{-3} (panel h) to ρ_{ISM} = 10^{-25} g cm^{-3} (panel e) leads to an increase in the cavity blown out by the stellar wind with a speed of 2000 km s^{-1}. The AP distance increases from $\sim$ 4.8 pc to $\sim$ 22 pc after a simulation time of 500 $\times$ 10^3 y when ρ_{ISM} was decreased by a factor of 100. This corresponds to an increase of a factor of $\sim$ 4.6. As for the shock after the same simulation time, it increases from $\sim$ 0.2 pc to $\sim$ 2 pc, corresponding to an increase of a factor of $\sim$ 10. The AP, after a simulation time of 900 $\times$ 10^3 y, increased from $\sim$ 5.6 pc to $\sim$ 26 pc, corresponding to an increase of a factor of $\sim$ 4.6. As for the shock, it increases from $\sim$ 0.2 pc to $\sim$ 2 pc, corresponding to an increase of a factor of $\sim$ 10 when ρ_{ISM} was lowered.

From the quantitative analysis above, where both the ISM density and mass-loss rate were kept fixed, the factor increase of both the TS and the AP radii corresponding to a tripling of the stellar wind speed from 1000 km s^{-1} to 3000 km s^{-1} (after a simulation time of 500 $\times$ 10^3 y) is a factor of $\sim$ 3.0 - 3.5. For the second investigation, the stellar wind speed and mass-loss rate were kept fixed. The factor increase of the AP for a decrease of ρ_{ISM} from ρ_{ISM} = 10^{-23} g cm^{-3} to ρ_{ISM} = 10^{-25} g cm^{-3}(after both simulation times of 500 $\times$ 10^3 y and 900 $\times$ 10^3 y) is a factor of $\sim$ 4.8 - 5.0. As for the TS distance, for the same change in ISM density, the factor increase stays constant around a factor of $\sim$ 10-12.

Above, the shock and AP distances were compared when both the ISM density and mass-loss rates were kept fixed, and the stellar wind speed was changed, or by keeping the speed fixed and varying the ISM density. Now, by keeping both the ISM density and stellar wind speed fixed, the TS and AP evolution is investigated by changing the mass-loss rate of the star, from 10^{-5} $M_\odot$ yr^{-1} to 5 $\times$ 10^{-6} $M_\odot$ yr^{-1} to 10^{-6} $M_\odot$ yr^{-1}. For this purpose, only one scenario is considered. This scenario being for an ISM density of 10^{-25} g cm^{-3} and a stellar wind speed of 2000 km s^{-1}, corresponding to panel (e) shown in Figures 4.2, 4.3 and 4.4 respectively.

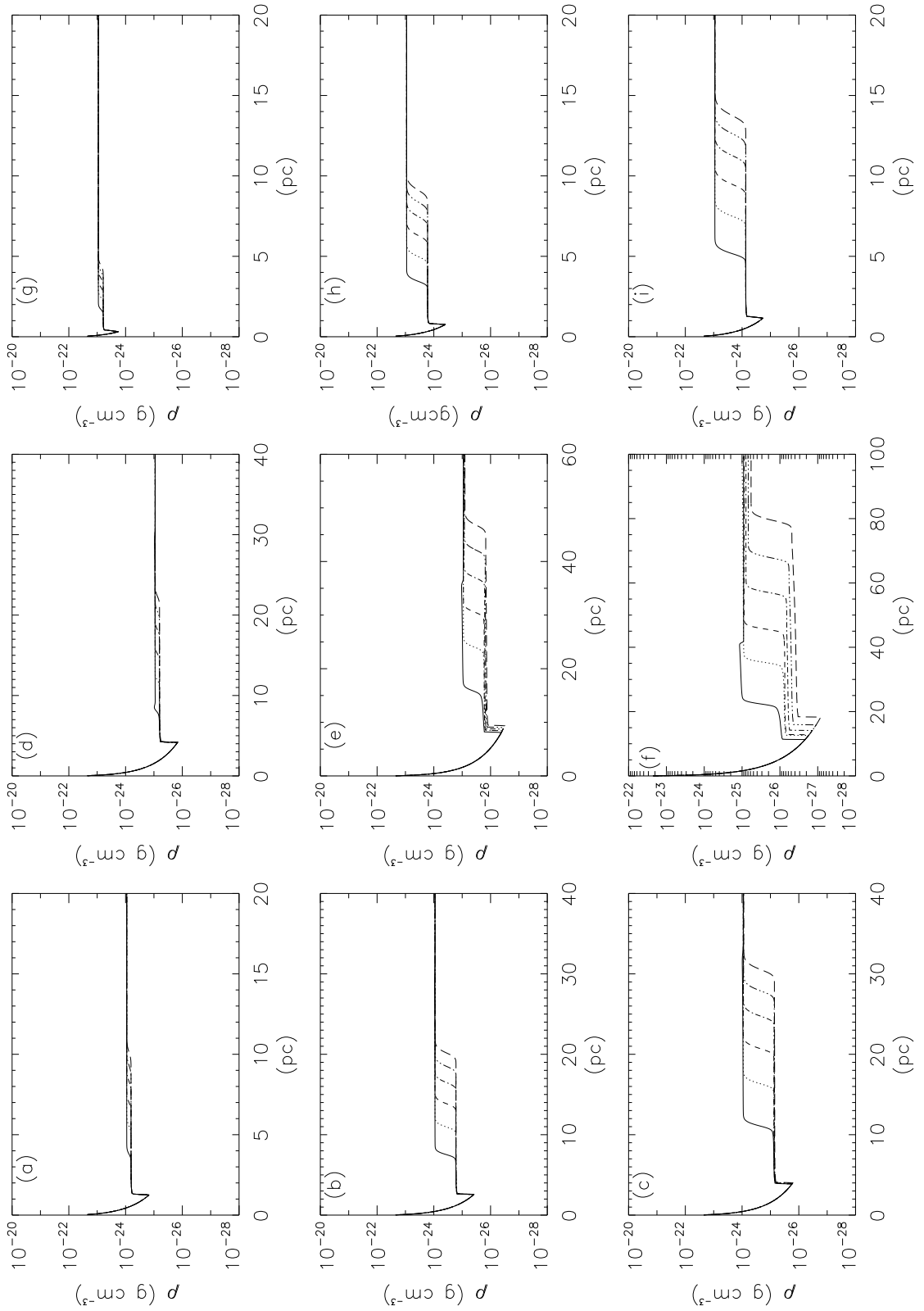

Figure 4.3: Same as Figure 4.2, but with a mass-loss rate of 5×10^{-6} $M_{\odot}$ y^{-1}. Letters (a-i) correspond to models 10-18 in Table 4.1.

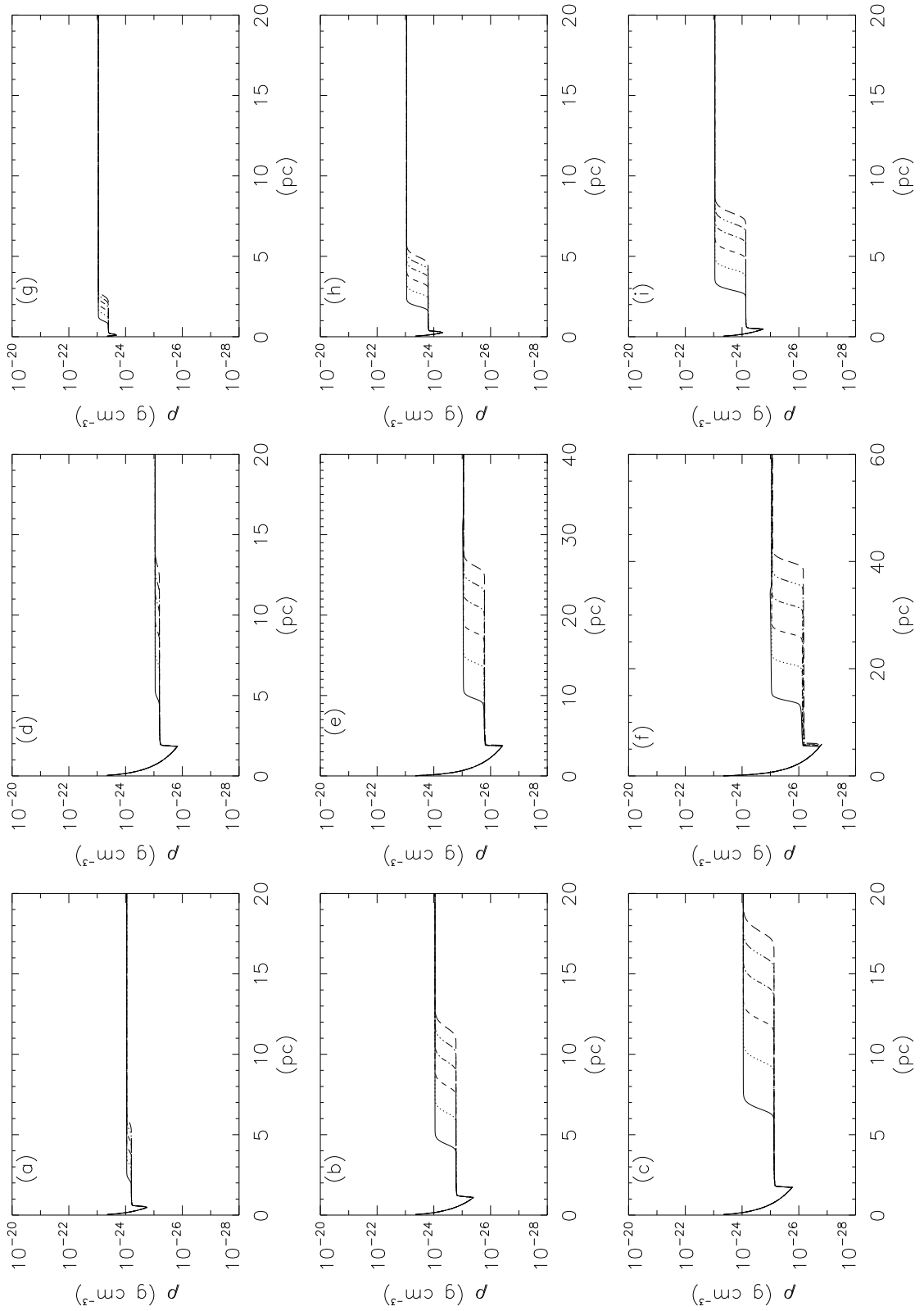

Figure 4.4: Same as Figure 4.2, but with a mass-loss rate of 10^{-6} $M_{\odot}$ y^{-1}. Letters (a-i) correspond to models 19-27 in Table 4.1.

From this comparison it follows that the TS changes from ~ 4 pc in Figure 4.4 to ~ 9 pc in Figure 4.3 to ~ 13 pc in Figure 4.2 for a simulation time of 500×10^3 y. Therefore, by increasing the mass-loss rate from 10^{-6} $M_\odot$ yr^{-1} (Figure 4.4) to 10^{-5} $M_\odot$ yr^{-1} (Figure 4.2), the TS increases by a factor of ~ 3.3. The AP distance also changes from ~ 23 pc in Figure 4.4 to ~ 48 pc in Figure 4.2 for the same simulation time. This corresponds to an increase of a factor of ~ 2.1 (between Figure 4.4 and Figure 4.2). For a simulation time of 900×10^3 y, the TS increases from ~ 4 pc in Figure 4.4 to ~ 10 pc in Figure 4.3 to ~ 14 pc in Figure 4.2, which corresponds to an increase of a factor of ~ 3.5 (between Figure 4.4 and Figure 4.2). For the same simulation time, the AP increases from ~ 28 pc in Figure 4.4 to ~ 66 pc in Figure 4.2, corresponding to an increase of a factor of ~ 2.3.

4.2.2 Density profiles for stellar wind evolution of an embedded star

Table 4.2: Parameter for stellar wind-ISM interaction in a more dense ambient ISM

Model	$\dot{M}$ ($M_\odot$ y^{-1})	v (km.s^{-1})	ρ_{ISM}(g cm^{-3})
1	10^{-5}	2000	10^{-22}
2	10^{-5}	3000	10^{-22}
3	10^{-5}	2000	10^{-21}
4	10^{-5}	3000	10^{-21}
5	5×10^{-5}	2000	10^{-22}
6	5×10^{-5}	3000	10^{-22}
7	5×10^{-5}	2000	10^{-21}
8	5×10^{-5}	3000	10^{-21}

The previous section considered the case of stellar wind evolution directly into the undisturbed ISM with typical densities in the order of $\rho_{ISM} = 10^{-25}$ g cm^{-3} to $\rho_{ISM} = 10^{-23}$ g cm^{-3}. In this section, the evolution is considered where the star is still deeply embedded within a molecular cloud (MC). For this case, the ambient undisturbed density is increased to $\rho_{ISM} = 10^{-22}$ g cm^{-3} and $\rho_{ISM} = 10^{-21}$ g cm^{-3} respectively. The following figures show results obtained from simulations with parameters as shown in Table 4.2. The mass-loss rate is kept fixed at 10^{-5} $M_\odot$ yr^{-1} and both the stellar wind speed and ISM density are changed for models 1-4. For models 5-8, the mass-loss rate is 5×10^{-6} $M_\odot$ yr^{-1} and again the speed and density are varied as indicated.

Just as for the case of the lower ISM density simulations, the density profiles for the case of evolution within an MC show the same structure which includes a TS and AP. However, due to the higher density of these clouds, these structures form much closer to the star compared to the case of evolution into a lower density ambient ISM as in the previous section.

Figure 4.5 and Figure 4.6 show the computed density profiles for the case where $\rho_{ISM} = 10^{-22}$ g cm^{-3} (left column) and $\rho_{ISM} = 10^{-21}$ g cm^{-3} (right column). Figure 4.5 corresponds to simulations with a mass-loss rate of 10^{-5} $M_\odot$ y^{-1} and Figure 4.6 to simulations with a mass-loss rate of 5×10^{-6} $M_\odot$ y^{-1}. In these figures, the top panels correspond to a stellar wind speed of 2000 km s^{-1} and the bottom panels to a stellar wind speed of 3000 km s^{-1}.

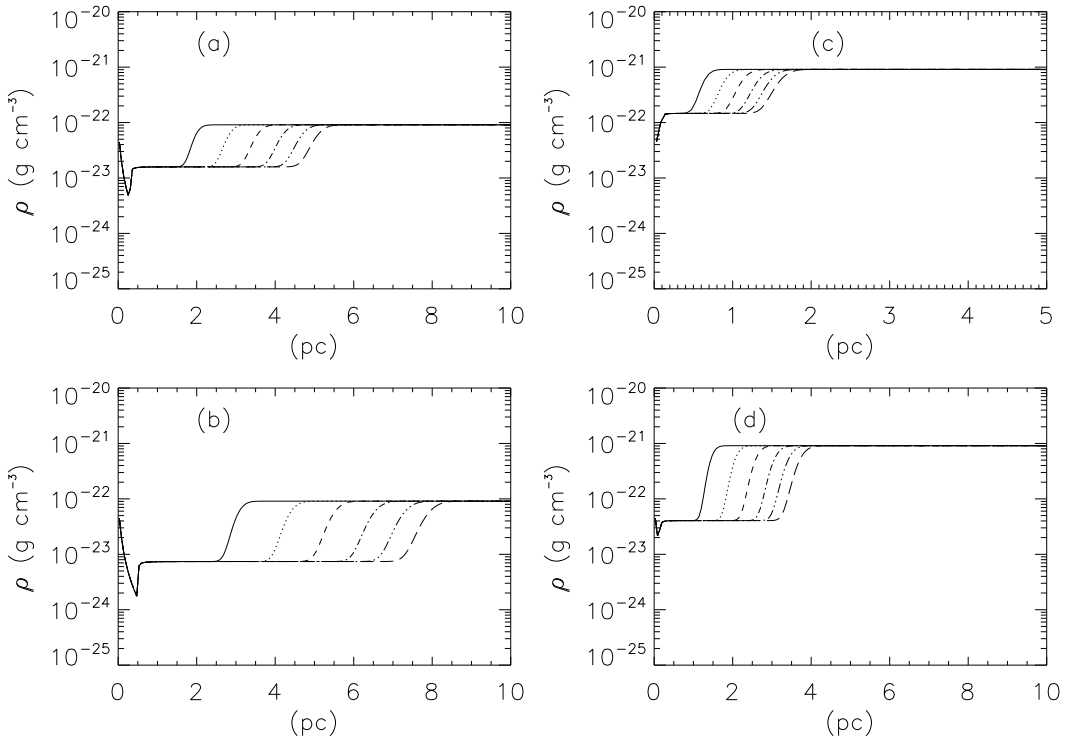

Figure 4.5: Computed density profiles for stellar winds with a mass-loss rate of 10^{-5} $M_{\odot}$ y^{-1}. The model parameters are given as models 1-4 in Table 4.2. The left panels show results when ρ_{ISM} = 10^{-22} g cm^{-3}, and the right panels show results when ρ_{ISM} = 10^{-21} g cm^{-3} as assumed in the model. Also, the top panels are for a stellar wind speed v = 2000 km s^{-1} and the bottom panels correspond to a stellar wind speed v = 3000 km s^{-1} in the model.

As stated previously, it also follows from Figure 4.5 and Figure 4.6 that the AP moves outward (inward) as the stellar wind speed is increased (decreased). The same happens for the ambient ISM density, whereas the ambient ISM density increases (decreases), both the TS and AP distances decrease (increase). Lastly, as the mass-loss rate is increased (decreased), the boundary moves outward (inward).

Comparing the left panels in Figure 4.5 to each other, where panel (a) corresponds to an assumed stellar wind speed of 2000 km s^{-1} and panel (b) to a speed of 3000 km s^{-1} in the model (both with ρ_{ISM} = 10^{-22} g cm^{-3}), it follows that by increasing the stellar wind speed the AP radius increases from $\sim$ 4.4 pc to $\sim$ 6.8 pc for a simulation time of 500 $\times$ 10^3 y. This corresponds to an increase of a factor of $\sim$ 1.5. As for the TS, its radius increases from $\sim$ 0.3 pc to $\sim$ 0.6 pc, for the same simulation time, corresponding to an increase of a factor of $\sim$ 2.0. The same follows for the AP after a simulation time of 900 $\times$ 10^3 y, where the AP radius increases from $\sim$ 5.4 pc to $\sim$ 8.6 pc, corresponding to an increase of a factor of $\sim$ 1.6. As for the TS after a simulation time of 900 $\times$ 10^3 y, it increases from $\sim$ 0.3 pc to $\sim$ 0.6 pc, corresponding to an increase of a factor of $\sim$ 2.0 when the stellar wind speed is increased from 2000 km s^{-1} to 3000 km s^{-1}.

Comparing the bottom two panels in Figure 4.5, where panel (b) corresponds to a ρ_{ISM} = 10^{-22} g cm^{-3} and panel (d) to a ρ_{ISM} = 10^{-21} g cm^{-3} (both with a stellar wind speed of 3000 km s^{-1}),

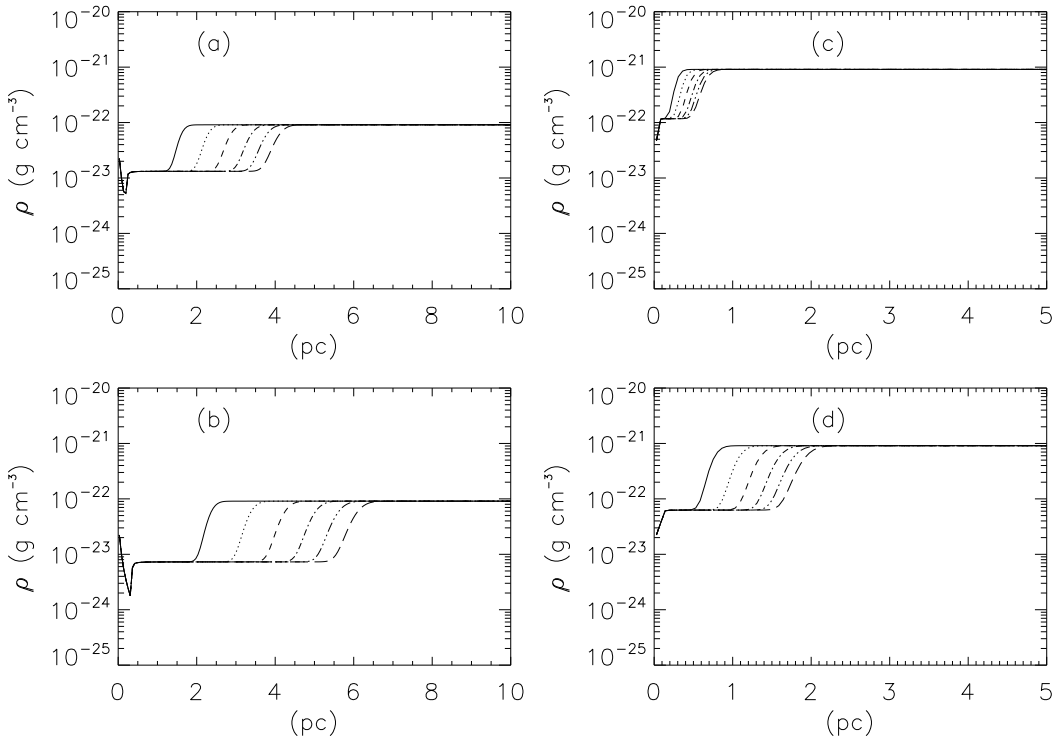

Figure 4.6: Same as Figure 4.5, but with a mass-loss rate of 5×10^{-6} $M_\odot$ y^{-1}.

it follows that the AP radius increases from $\sim$ 3.4 pc when ρ_{ISM} = 10^{-21} g cm^{-3} to $\sim$ 6.8 pc when ρ_{ISM} = 10^{-22} g cm^{-3} is assumed in the model. This is for a simulation time of 500 $\times$ 10^3 y and corresponds to an increase of a factor of $\sim$ 2.0. The TS increases from $\sim$ 0.1 pc to $\sim$ 0.6 pc, corresponding to an increase of a factor of $\sim$ 6.0. For 900 $\times$ 10^3 y, the AP increases from $\sim$ 4.1 pc to $\sim$ 8.6 pc, an increase of a factor of $\sim$ 2.1, and the TS increases from $\sim$ 0.1 pc to $\sim$ 0.6 pc, corresponding to an increase of a factor of $\sim$ 6.0, when ρ_{ISM} is decreased by a factor of 10.

Next, a comparison is done between different panels in Figure 4.5 and Figure 4.6. The only difference between these figures is that Figure 4.6 has an assumed mass-loss rate of 5×10^{-6} $M_\odot$ y^{-1}, whereas Figure 4.5 has an assumed mass-loss rate of 10^{-5} $M_\odot$ y^{-1}. Comparing panel (b) (bottom left panel) in Figure 4.5 and panel (b) in Figure 4.6 it follows that for the ρ_{ISM} = 10^{-22} g cm^{-3} scenario the cavity blown out by the stellar wind with speed 3000 km s^{-1} increases from $\sim$ 4.5 pc to $\sim$ 6.2 pc when the mass-loss rate is increased. This corresponds to an increase of a factor of $\sim$ 1.3 after a simulation time of 500 $\times$ 10^3 y. The same follows for the TS increasing from $\sim$ 0.4 pc to $\sim$ 0.6 pc, which corresponds to an increase of a factor of $\sim$ 1.5. For a simulation time of 900 $\times$ 10^3 y, the AP increases from $\sim$ 5.8 pc to $\sim$ 7.8 pc, corresponding to an increase of a factor of $\sim$ 1.3, and the TS increases from $\sim$ 0.4 pc to $\sim$ 0.6 pc, which corresponds to an increase of a factor of $\sim$ 1.5, when the mass-loss rate is increased by a factor of 2.

Lastly, comparing panel (d) (bottom right panel) in Figure 4.5 and panel (d) in Figure 4.6, where

ρ_{ISM} = 10^{-21} g cm^{-3} and the stellar wind speed is 3000 km s^{-1} it follows that changing the mass-loss rate from 5 $\times$ 10^{-6} M$_\odot$ y^{-1} to 10^{-5} M$_\odot$ y^{-1}, the cavity blown out by the stellar wind increases from $\sim$ 1.5 pc to $\sim$ 3.0 pc. This corresponds to an increase of a factor of $\sim$ 2.0, after a simulation time of 500 $\times$ 10^3 y. The TS increases from $\sim$ 0.08 pc to $\sim$ 0.1 pc, an increase of a factor of $\sim$ 1.3. For a simulation time of 900 $\times$ 10^3 y, the AP increases from $\sim$ 1.9 pc to $\sim$ 3.9 pc, corresponding to an increase of a factor of $\sim$ 2.0. The TS increases from $\sim$ 0.08 pc to $\sim$ 0.1 pc, resulting in an increase of a factor of $\sim$ 1.3, when the mass-loss rate is increased by a factor of 2.

From the quantitative analysis done above it follows that for the case of evolution into a MC (where both the ISM density and mass-loss rate were kept fixed), the factor increase of the AP for the increase of the stellar wind speed from 2000 km s^{-1} to 3000 km s^{-1}, for both the simulation times reported on, is a factor of $\sim$ 1.5. As for the TS, the increase is a factor of $\sim$ 2.0. For the second investigation, the stellar wind speed and mass-loss rate were kept fixed. The factor increase of the AP for a decrease of ρ_{ISM} from ρ_{ISM} = 10^{-21} g cm^{-3} to ρ_{ISM} = 10^{-22} g cm^{-3}, for both the two simulation times considered, is a factor of $\sim$ 2.0. As for the TS distance, the factor increase is $\sim$ 6.0, for both the mass-loss rates, for both simulation times considered. For the third investigation, where the stellar wind speed and ISM density are kept fixed, the factor increase of the AP for a mass-loss rate of 5 $\times$ 10^{-6} M$_\odot$ y^{-1} to a mass-loss rate of 10^{-5} M$_\odot$ y^{-1} for both the ISM densities and for a stellar wind speed of 3000 km s^{-1}, is a factor of $\sim$ 2.0. As for the TS, the factor increase is a factor of $\sim$ 1.3. This is the case for both the simulation times considered, namely 500 $\times$ 10^3 y and 900 $\times$ 10^3 y respectively.

4.3 Evolution of stellar wind structures

The evolution of the AP and TS radius as a function of time is now shown in more detail by plotting the radii of these structures against time. Again the evolution into an ambient ISM and a more dense region (e.g. molecular clouds) are treated separately.

4.3.1 Evolution into the ambient ISM

In the following figures, all lines in the top panel of a particular figure show both the TS and AP radius as functions of time, while the lines in the bottom panel show the ratio between the AP and TS radii. Different scenarios are shown corresponding to different parameters indicated by different colours and line-styles. In the top panel, the top increasing lines correspond to the AP, while the bottom lines correspond to the TS (because of the smaller radius).

In Figure 4.7, different computed scenarios are shown corresponding to a stellar wind speed of 1000 km s^{-1} (red solid line), a stellar wind speed of 2000 km s^{-1} (green long dashed line), and a stellar wind speed of 3000 km s^{-1} (blue short dashed line). All correspond to a stellar mass-loss rate of 5 $\times$ 10^{-6} M$_\odot$ y^{-1} and ρ_{ISM} = 10^{-24} g cm^{-3}, as shown by models 10-12 in Table

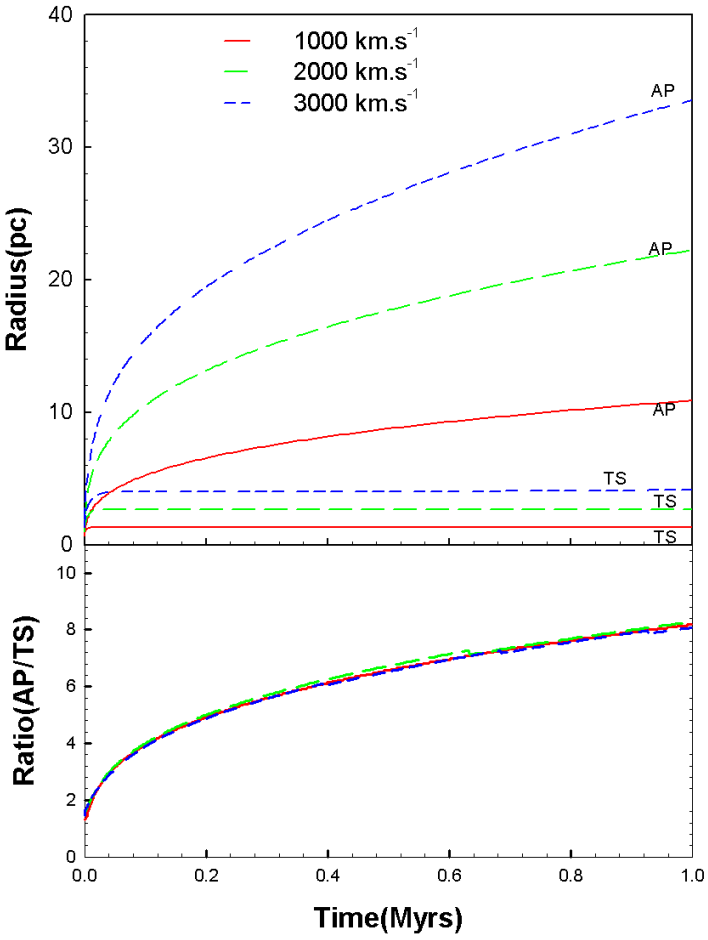

Figure 4.7: The top panel shows the computed time profiles of the TS and AP distance of the different stellar winds corresponding models 10-12 (see Table 4.1 and panels a, b and c in Figure 4.3). A mass-loss rate of 5×10^{-6} $M_{\odot}$ y^{-1}, and ISM density of 10^{-24} g cm^{-3} are assumed. The legends denote different stellar wind speeds. The bottom panel shows the ratio of the AP and the TS radii.

4.1 and panels (a), (b) and (c) in Figure 4.3. The bottom figure shows the ratio between the AP distance and the TS distance, for the three different stellar wind speed scenarios (denoted by the same colours).

From Figure 4.7 it follows that both the TS and the AP expand further into the ISM with an increase in stellar wind speed from e.g. 1000 km s^{-1} to 2000 km s^{-1} and finally to 3000 km s^{-1}. For all scenarios, the AP expands more rapidly in the early stages of evolution. By increasing the stellar wind speed from e.g. 1000 km s^{-1} to 3000 km s^{-1}, the AP expands further resulting in a larger cavity after a simulation time of a million years. The TS, for all three scenarios, increases for the first $\sim 50 \times 10^3$ y before becoming constant as a function of time.

In the bottom panel of Figure 4.7 it follows that the ratio of the AP and TS radii for ρ_{ISM} = 10^{-24} g cm^{-3} and a mass-loss rate of 10^{-5} $M_{\odot}$ y^{-1} increases steadily for all three the stellar wind speed scenarios. Because the TS becomes constant as a function of time after $\sim 50 \times 10^3$

y, this ratio increases with an amount equal to the expansion rate of the AP. Note that for all three scenarios the ratios are similar, indicating that the AP can be expressed in terms of the TS (or vice versa) with a proportionality constant (see e.g. *Müller et al.*, 2006), which may change over time.

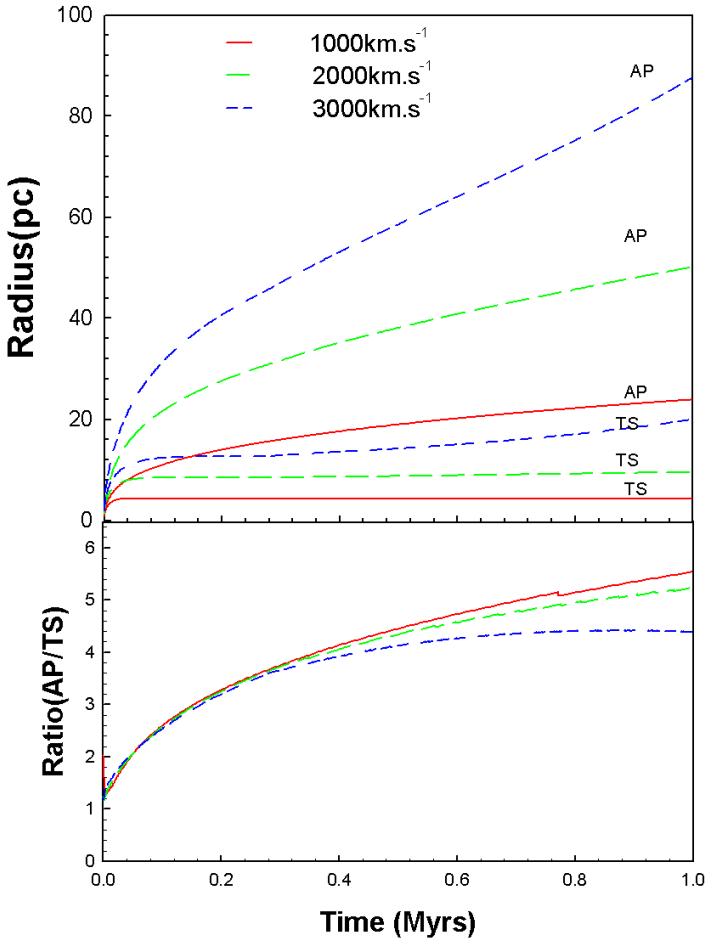

Figure 4.8: Similar to Figure 4.7, except for a ρ_{ISM} = 10^{-25} g cm^{-3}.

Next, the ISM density (ρ_{ISM}) is changed and results are shown in Figure 4.8 and Figure 4.9, where Figure 4.8 corresponds to ρ_{ISM} = 10^{-25} g cm^{-3} and Figure 4.9 to ρ_{ISM} = 10^{-23} g cm^{-3} assumed in the model. The mass-loss rate is fixed to a value of 5 $\times$ 10^{-6} M$_{\odot}$ y^{-1} as in Figure 4.7. Panels (d), (e) and (f) in Figure 4.3 correspond to the profiles shown in Figure 4.8, and panels (g), (h) and (i) in Figure 4.3 correspond to the profiles in Figure 4.9.

Similar results are shown in these figures as in Figure 4.7, except in Figure 4.8 (where ρ_{ISM} = 10^{-25} g cm^{-3}) the TS is still expanding towards the end of the simulation time. For both ρ_{ISM} = 10^{-23} g cm^{-3} (Figure 4.9) and ρ_{ISM} = 10^{-24} g cm^{-3} (Figure 4.7) the TS is already constant as a function of time at $\sim$ 50 $\times 10^3$ years.

The ratios shown in the bottom panel of Figure 4.8 differ from those shown in Figure 4.7. The

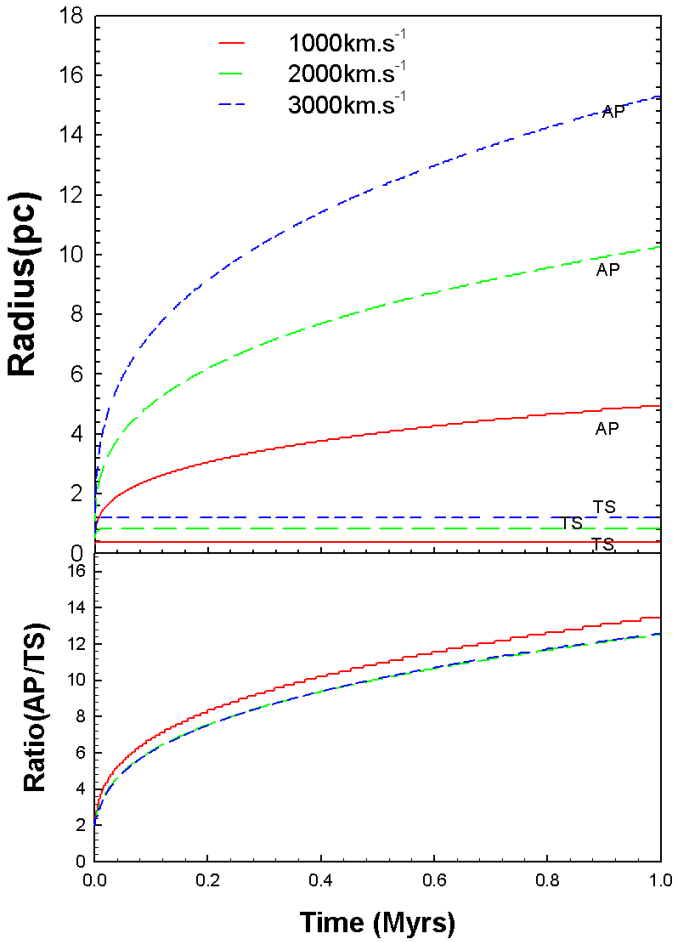

Figure 4.9: Similar to Figure 4.7, except for a ρ_{ISM} = 10^{-23} g cm^{-3}.

ratio of the stellar wind of 3000 km s^{-1} becomes smaller compared to those corresponding to stellar winds with outflow speeds of 1000 km s^{-1} and 2000 km s^{-1} respectively. This is because for the stellar wind speed of 3000 km s^{-1} and ρ_{ISM} = 10^{-25} g cm^{-3}, the TS still expands towards the end of the simulation time, thus reducing the ratio for the 3000 km s^{-1} stellar wind scenario (blue short dashed line).

Figure 4.9 shows the same as Figure 4.8, except the time profiles of models 16-18 are shown, corresponding to a mass-loss rate of 5 $\times$ 10^{-6} M$_{\odot}$ y^{-1} and ρ_{ISM} = 10^{-23} g cm^{-3}. However, because of the high ISM density, ρ_{ISM} = 10^{-23} g cm^{-3}, the AP only expands up to about $\sim$ 14 pc for stellar wind speed of 3000 km s^{-1}, compared to the $\sim$ 35 pc of the AP of Figure 4.7. The ratios of the TS radius to that of the AP radius also change between the different scenarios of Figure 4.9. The ratio for a stellar wind speed of 1000 km s^{-1} is the highest. This is because of the higher ISM density compared to e.g. Figure 4.8 where the computed TS radius is smaller compared to the other two.

Figure 4.10 shows the computed time profiles, which correspond to panels (a), (b) and (c) of

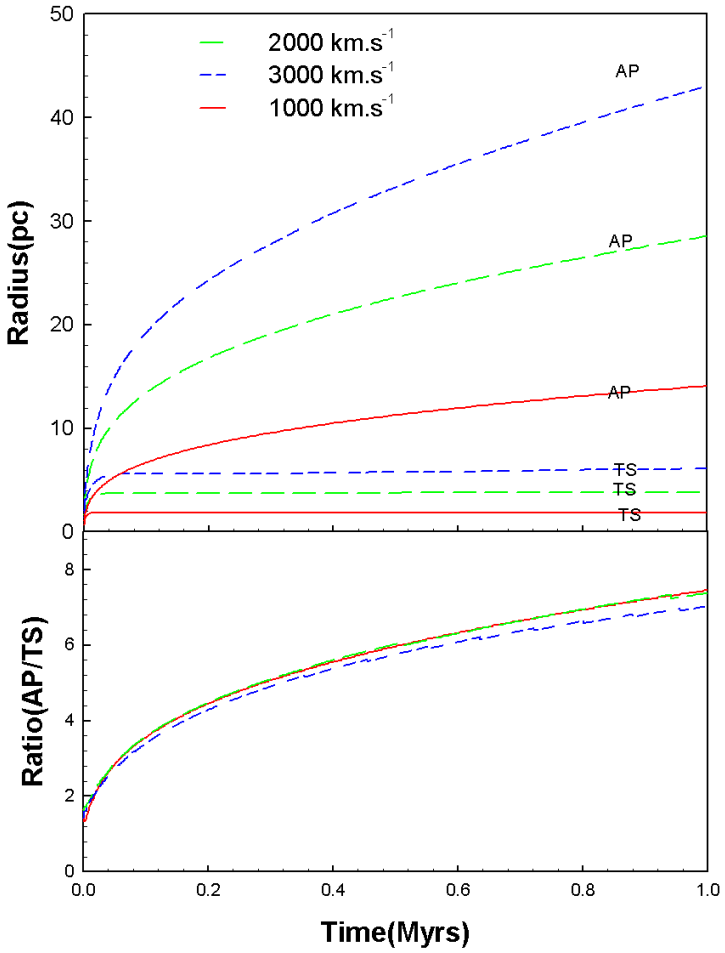

Figure 4.10: Similar to Figure 4.7, except for a mass-loss rate of 10^{-5} $M_{\odot}$ y^{-1}.

Figure 4.2, where mass-loss rates of 10^{-5} $M_{\odot}$ y^{-1} and ρ_{ISM} = 10^{-24} g cm^{-3} are assumed in the model. The ratio of the AP and TS of the stellar wind with speed 3000 km s^{-1} is less than the other two stellar wind speed scenarios. This is due to the fact that for a mass-loss rate of 10^{-5} $M_{\odot}$ y^{-1} and stellar wind speed of 3000 km s^{-1}, the TS moves out faster and further, compared to the other two stellar wind speed scenarios. However, again these lines almost coincide with each other indicating that the TS can be expressed in terms of the AP although the proportionality factor will vary with time.

The time profiles corresponding to a mass-loss rate of 10^{-5} $M_{\odot}$ y^{-1} and ρ_{ISM} = 10^{-25} g cm^{-3} are shown in Figure 4.11, which correspond to panels (d), (e) and (f) of Figure 4.2. For these, the mass-loss rate is the highest and ρ_{ISM} the lowest of all the scenarios. This will result in the largest cavities. Note that for panel (f) in Figure 4.2, the AP moves out of the grid size before the end of the simulation time, and is therefore only shown up to this time. Shown here is that for these scenarios, the ratio is also dependent on the outflow speed assumed in the model.

Figure 4.12 shows the computed time profiles for the case where ρ_{ISM} = 10^{-25} g cm^{-3} and the

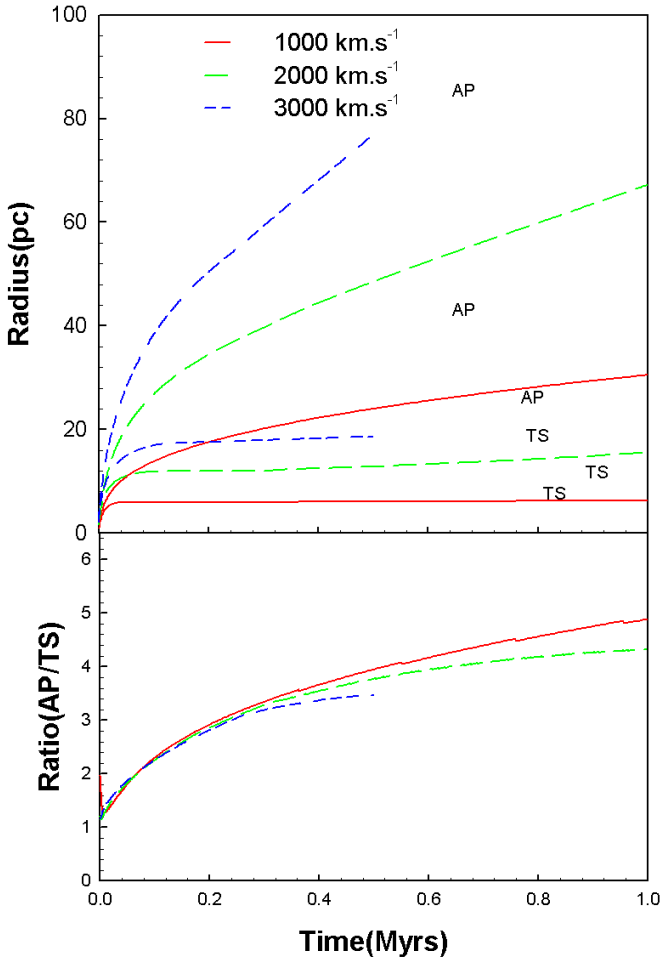

Figure 4.11: Similar to Figure 4.10, except for a ρ_{ISM} = 10^{-25} g cm^{-3}. Note that for the 3000 km s^{-1} scenario the AP radius moves out of our integration volume and therefore, only values up to 500 $\times$ 10^3 y are shown.

mass-loss rate is 10^{-6} M$_\odot$ y^{-1}, corresponding to panels (d), (e) and (f) in Figure 4.4. In this case, the TS is already constant as a function of time after $\sim$ 50 $\times$ 10^3 y. Also, the initial expansion of the AP is much slower for this assumed mass-loss rate compared to the cases where the mass-loss rates are higher, e.g. 10^{-5} M$_\odot$ y^{-1} (Figure 4.11) and 5 $\times$ 10^{-6} M$_\odot$ y^{-1} (Figure 4.8). Shown here is again that the ratios are almost similar irrespective of outflow speed.

Figure 4.13 shows the computed time profiles for the case where the ISM density is 10^{-23} g cm^{-3} and the mass-loss rate is 10^{-6} M$_\odot$ y^{-1}, corresponding to panels (g), (h) and (i) in Figure 4.4. For this case, the TS is also constant as a function of time after $\sim$ 50 $\times$ 10^3 y. The AP also expands to the end of the simulation time. Shown here is that for this particular set of parameters, the ratio between the AP and TS radii is dependent on the outflow speed.

We can summarize, for Figures 4.7 to 4.13, that if the AP of a stellar wind with a speed of 2000 km s^{-1} is compared to the AP of a stellar wind with a speed of 1000 km s^{-1} (having the same ISM density and mass-loss rate), the result is that the AP radius for the 1000 km s^{-1} wind

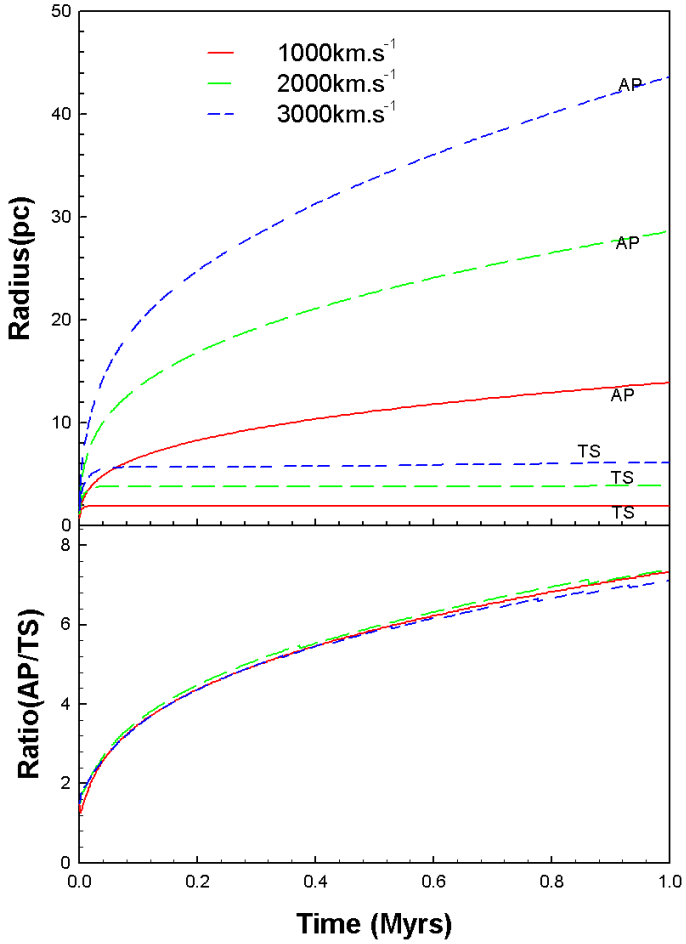

Figure 4.12: Similar to Figure 4.11, except for a mass-loss rate of 10^{-6} $M_{\odot}$ y^{-1}.

scenario is $\sim$ 50% of that of the 2000 km s^{-1} wind scenario after a simulation time of 1 My. If the same is done for the 3000 km s^{-1} and 1000 km s^{-1} stellar wind scenarios, the result is that the AP radius for the 1000 km s^{-1} stellar wind is $\sim$ 33% of that corresponding to the 3000 km s^{-1} wind after 1 My. Doing the same with the 2000 km s^{-1} and 3000 km s^{-1} scenario, the 2000 km s^{-1} stellar wind result in an AP radius, which is $\sim$ 66% of that corresponding to the 3000 km s^{-1} stellar wind after 1 My. This is the case for all the different mass-loss rates and ISM densities assumed in Figure 4.7 to Figure 4.13 and after a simulation time of 1 My.

For a constant stellar wind speed and mass-loss rate, the effect of different ISM densities can also be shown. Comparing the AP radius for a ρ_{ISM} = 10^{-23} g cm^{-3} scenario to that of a ρ_{ISM} = 10^{-24} g cm^{-3} scenario, one finds that the AP radius for ρ_{ISM} = 10^{-23} g cm^{-3} is $\sim$ 46% that of the AP radius for a ρ_{ISM} = 10^{-24} g cm^{-3}. If the same is done for a ρ_{ISM} = 10^{-24} g cm^{-3} and a ρ_{ISM} = 10^{-25} g cm^{-3} scenario, the computed AP radius for a ρ_{ISM} = 10^{-24} g cm^{-3} is $\sim$ 42% of that of the AP radius for a ρ_{ISM} = 10^{-25} g cm^{-3} scenario. Also, if one takes the ratio between the AP radius, for a ρ_{ISM} = 10^{-23} g cm^{-3} and a ρ_{ISM} = 10^{-25} g cm^{-3} scenario it is found that

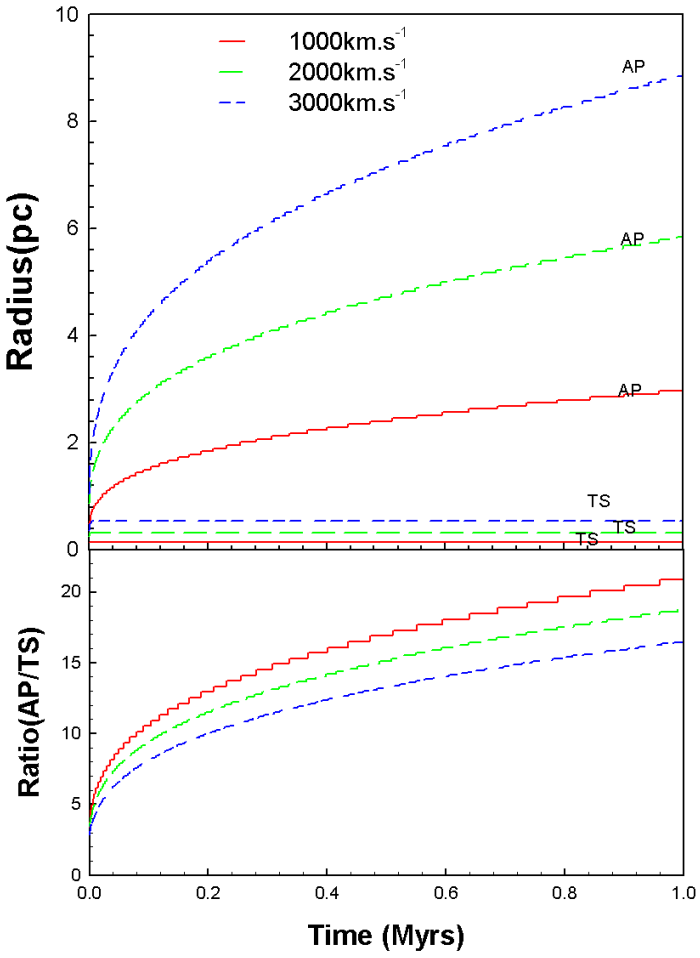

Figure 4.13: Similar to Figure 4.12, except for a ρ_{ISM} = 10^{-23} g cm^{-3}.

the AP radius for a ρ_{ISM} = 10^{-23} g cm^{-3} scenario is $\sim$ 21% of that of the AP radius for ρ_{ISM} = 10^{-25} g cm^{-3}. This is the case for a simulation time of 1 My.

The same can be done by varying the stellar mass-loss rate. Comparing the computed AP radius corresponding to a stellar mass-loss rate of 10^{-6} M$_\odot$ y^{-1} to that of a stellar mass-loss rate of 5 $\times$ 10^{-6} M$_\odot$ y^{-1}, one finds that the AP radius corresponding to a stellar mass-loss rate of 10^{-6} M$_\odot$ y^{-1} is $\sim$ 60% that of the AP for a stellar mass-loss rate of 5 $\times$ 10^{-6} M$_\odot$ y^{-1}. Comparing a mass-loss rate scenario of 5 $\times$ 10^{-6} M$_\odot$ y^{-1} to that of 10^{-5} M$_\odot$ y^{-1}, it follows that the AP of the stellar mass-loss rate of 5 $\times$ 10^{-6} M$_\odot$ y^{-1} is $\sim$ 78% that of the AP for a stellar mass-loss rate of 10^{-5} M$_\odot$ y^{-1}. The AP for a stellar mass-loss rate of 10^{-6} M$_\odot$ y^{-1} is $\sim$ 46% that of a stellar mass-loss rate of 10^{-5} M$_\odot$ y^{-1}. This is for a simulation time of 1 My.

4.3.2 Evolution inside a molecular cloud

The time evolution of the TS and AP radius inside different high density media is now considered. Computations are shown corresponding to different scenarios, namely different outflow speeds of 2000 km s^{-1} and 3000 km s^{-1}, ISM densities of ρ_{ISM} = 10^{-22} g cm^{-3} and ρ_{ISM} = 10^{-21} g cm^{-3} and mass-loss rates of 5 $\times$ 10^{-6} $M_\odot$ y^{-1} and 10^{-5} $M_\odot$ y^{-1} respectively.

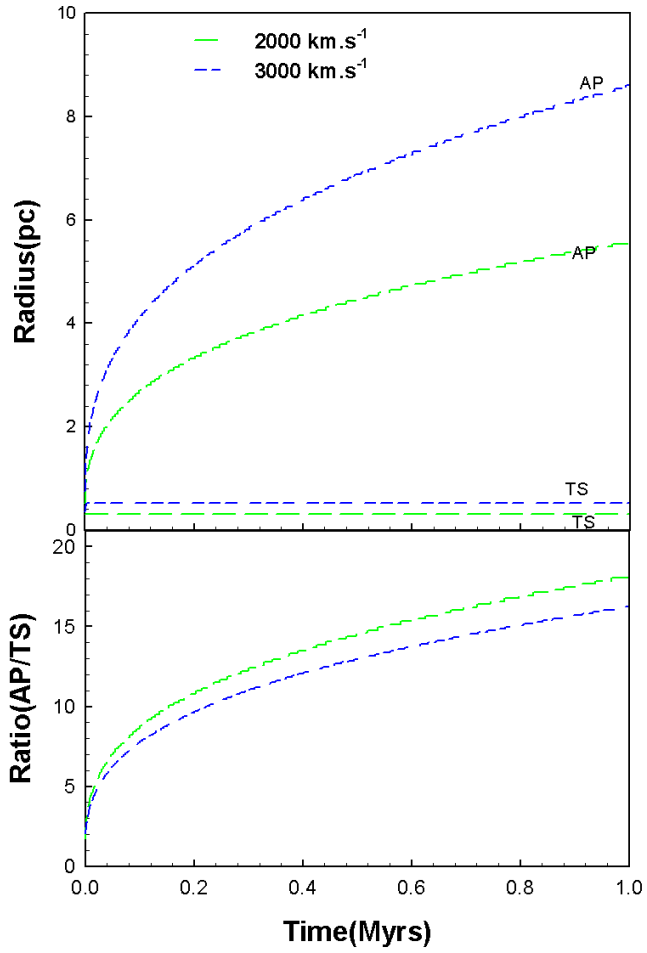

Figure 4.14: Top panel: The computed time profiles of the stellar winds of models 1-2 (see Table 4.2 and panels a and b from Figure 4.5 in section 4.2). A mass-loss rate of 10^{-5} $M_\odot$ y^{-1}, and ρ_{ISM} = 10^{-22} g cm^{-3} are assumed in the model. The legends denote different stellar wind speeds. The bottom panel shows the ratio of the AP and TS radii.

The top panel of Figure 4.14 shows the computed time profiles of the AP and TS radii evolving into a molecular cloud with ρ_{ISM} = 10^{-22} g cm^{-3}. The green (long dash) line corresponds to a stellar wind speed of 2000 km s^{-1} and the blue (short dash) line corresponds to a stellar wind speed of 3000 km s^{-1}. Both have mass-loss rates of 10^{-5} $M_\odot$ y^{-1}. As also shown in the previous figures, both the green and the blue lines show considerable expansion of the AP in the early stages of evolution, after which the rate of expansion of the AP steadily decreases. As for the previous figures, the TS expands early on and becomes constant as a function of time.

The bottom panel shows the ratio between the TS and AP as before.

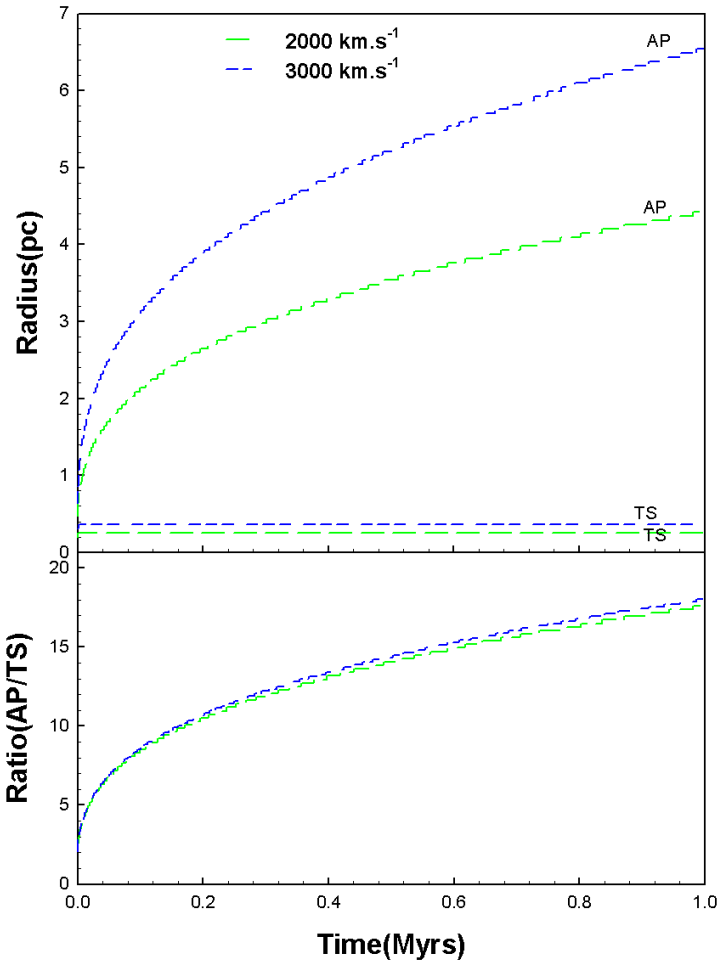

Figure 4.15: Similar to Figure 4.5, except for a mass-loss rate of 5×10^{-6} $M_\odot$ y^{-1}, and $\rho_{ISM} = 10^{-22}$ g cm^{-3}.

Figure 4.15, Figure 4.16 and Figure 4.17 show the same as shown in Figure 4.14. However, Figure 4.15 corresponds to a mass-loss rate of 5×10^{-6} $M_\odot$ y^{-1} and $\rho_{ISM} = 10^{-22}$ g cm^{-3}. Figure 4.16 corresponds to the same mass-loss rate as Figure 4.14, namely 10^{-5} $M_\odot$ y^{-1}, but $\rho_{ISM} = 10^{-21}$ g cm^{-3}. Figure 4.17 corresponds to a mass-loss rate of 5×10^{-6} $M_\odot$ y^{-1} and $\rho_{ISM} = 10^{-21}$ g cm^{-3}. Panel (c) in Figure 4.5 corresponds to the green long dashed line in Figure 4.16 and panel (d) in Figure 4.5 corresponds to the blue short dashed line in Figure 4.16. Panel (a) in Figure 4.5 corresponds to the green long dashed line in Figure 4.14 and panel (b) in Figure 4.5 corresponds to the blue short dashed line in Figure 4.14. The green long dashed line in Figure 4.15 corresponds to panel (a) in Figure 4.6 and the blue short dashed line corresponds to panel (b) in Figure 4.6. The green long dashed line in Figure 4.17 corresponds to panel (c) in Figure 4.6 and the blue short dashed line corresponds to panel (d) in Figure 4.6.

As before, the AP and TS radii move inward (or outward) as the density in the cloud is increased (or decreased). From Figure 4.14 and Figure 4.16 (which both have a mass-loss rate of

10^{-5} $M_\odot$ y^{-1}) it follows that the cavity blown out by the stellar wind with a speed of 2000 km s^{-1} and ρ_{ISM} = 10^{-21} g cm^{-3} (green long dash line in Figure 4.16 and panel c in Figure 4.5), is $\sim$ 1.4 pc, after a simulation time of 500 $\times$ 10^3 y. When assuming ρ_{ISM} = 10^{-22} g cm^{-3} (green long dashed line in Figure 4.14 and panel a in Figure 4.5), the cavity blown out by the stellar wind is $\sim$ 4.3 pc for the same simulation time. This corresponds to an increase of a factor of $\sim$ 3.0 when the ISM density is decreased by a factor of 10. For a stellar wind of 3000 km s^{-1}, and ρ_{ISM} = 10^{-21} g cm^{-3} (blue short dashed line in Figure 4.16 and panel d in Figure 4.5), the cavity blown out by the stellar wind after a simulation time of 500 $\times$ 10^3 y is $\sim$ 3.3 pc, whereas the cavity blown out by the stellar wind for ρ_{ISM} = 10^{-22} g cm^{-3} (blue short dashed line in Figure 4.14 and panel b in Figure 4.5) is $\sim$ 6.8 pc. This corresponds to an increase of a factor of $\sim$ 2.1.

As for the simulation time of 1 My, the cavity blown out by the stellar wind of 2000 km s^{-1}, with ρ_{ISM} = 10^{-21} g cm^{-3} and a mass-loss rate of 10^{-5} $M_\odot$ y^{-1} is $\sim$ 1.7 pc, whereas the AP radius corresponding to ρ_{ISM} = 10^{-22} g cm^{-3} is $\sim$ 5.3 pc. This corresponds to an increase of a factor of $\sim$ 3.1. For the case of a stellar wind speed of 3000 km s^{-1}, the cavity blown out by the stellar wind is $\sim$ 4.1 pc, with ρ_{ISM} = 10^{-21} g cm^{-3}, whereas for ρ_{ISM} = 10^{-22} g cm^{-3}, the cavity blown out by the stellar wind is $\sim$ 8.4 pc. This corresponds to an increase of a factor of $\sim$ 2.1. These are similar to the values above for 500 $\times$ 10^3 y.

In both Figure 4.15 and Figure 4.17 the mass-loss rate is assumed to be 5 $\times$ 10^{-6} $M_\odot$ y^{-1} in the model. The cavity blown out by the stellar wind of 2000 km s^{-1} and ρ_{ISM} = 10^{-21} g cm^{-3} after a simulation time of 500 $\times$ 10^3 y (green long dashed line in Figure 4.17 and panel c in Figure 4.6) is $\sim$ 0.7 pc. As for the stellar wind with ρ_{ISM} = 10^{-22} g cm^{-3} (green long dashed line in Figure 4.15 and panel a in Figure 4.6), the cavity blown out is $\sim$ 3.4 pc. This corresponds to an increase of a factor of $\sim$ 4.8. As for a stellar wind speed of 3000 km s^{-1} (blue short dashed line in Figure 4.17 and panel d in Figure 4.6), the cavity blown out is $\sim$ 1.7 pc, for ρ_{ISM} = 10^{-21} g cm^{-3}, whereas for ρ_{ISM} = 10^{-22} g cm^{-3} (blue short dashed line in Figure 4.15 and panel b in Figure 4.6), the cavity blown out is $\sim$ 5.1 pc, which corresponds to an increase of a factor of $\sim$ 3.0, for the same simulation time.

The cavity blown out by the stellar wind after a simulation time of 1 My, for a stellar wind speed of 2000 km s^{-1}, with ρ_{ISM} = 10^{-21} g cm^{-3} (green long dashed line in Figure 4.17 and panel c in Figure 4.6) is $\sim$ 0.8 pc, whereas for ρ_{ISM} = 10^{-22} g cm^{-3} (green long dashed line in Figure 4.15 and panel a in Figure 4.6), the cavity blown out is $\sim$ 4 pc. This corresponds to an increase of a factor of $\sim$ 5.0. As for the case of a stellar wind speed of 3000 km s^{-1} and ρ_{ISM} = 10^{-21} g cm^{-3} (blue short dashed line in Figure 4.17 and panel d in Figure 4.6), the cavity blown out is $\sim$ 2.1 pc. For ρ_{ISM} = 10^{-22} g cm^{-3} (blue short dashed line in Figure 4.15 and panel b in Figure 4.6), the cavity blown out is $\sim$ 6.2 pc, corresponding to an increase of a factor of $\sim$ 3.0.

All other combinations of parameters not yet discussed can be inferred from the figures. Instead, it can be concluded that by keeping the ambient density fixed at ρ_{ISM} = 10^{-22} g cm^{-3}, and changing the stellar wind speed from 2000 km s^{-1} to 3000 km s^{-1}, the AP distance for a

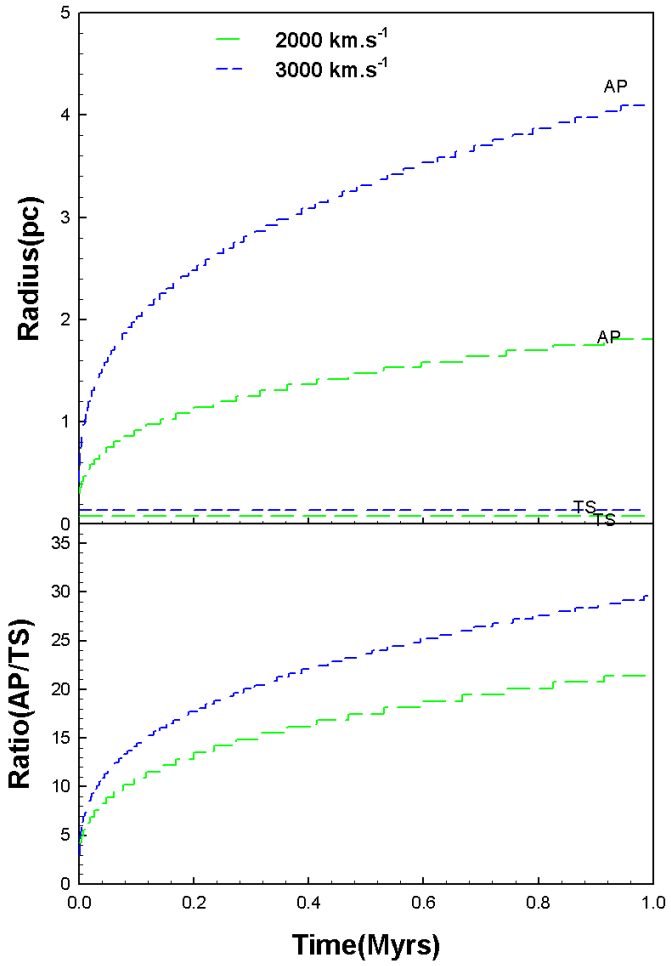

Figure 4.16: Similar to Figure 4.5, except for a mass-loss rate of 10^{-5} $M_{\odot}$ y^{-1}, and ρ_{ISM} = 10^{-21} g cm^{-3}.

stellar wind speed of 2000 km s^{-1} is $\sim$ 66% of that of a stellar wind speed of 3000 km s^{-1}, for both mass-loss rates investigated. However, for ρ_{ISM} = 10^{-21} g cm^{-3}, the AP distance for a stellar wind speed of 2000 km s^{-1} is $\sim$ 40% compared to a stellar wind speed of 3000 km s^{-1}, for both mass-loss rates investigated. Secondly, by keeping the mass-loss rate fixed at 10^{-5} $M_{\odot}$ y^{-1} and changing the ambient density, the AP for ρ_{ISM} = 10^{-21} g cm^{-3} forms at a distance $\sim$ 50% compared to the AP distance for ρ_{ISM} = 10^{-22} g cm^{-3}, for a stellar wind speed of 3000 km s^{-1}. For a stellar wind speed of 2000 km s^{-1} the AP for ρ_{ISM} = 10^{-21} g cm^{-3} forms at a distance $\sim$ 33% compared to the AP distance for ρ_{ISM} = 10^{-22} g cm^{-3}. For a mass-loss rate of 5×10^{-6} $M_{\odot}$ y^{-1} the AP for ρ_{ISM} = 10^{-21} g cm^{-3} forms at a distance of $\sim$ 20% compared to the AP distance for ρ_{ISM} = 10^{-22} g cm^{-3}, for a stellar wind of 2000 km s^{-1}. For a stellar wind of 3000 km s^{-1} the AP for ρ_{ISM} = 10^{-21} g cm^{-3} forms at a distance of $\sim$ 33% compared to the AP distance for ρ_{ISM} = 10^{-22} g cm^{-3}. These results are for both simulation times considered.

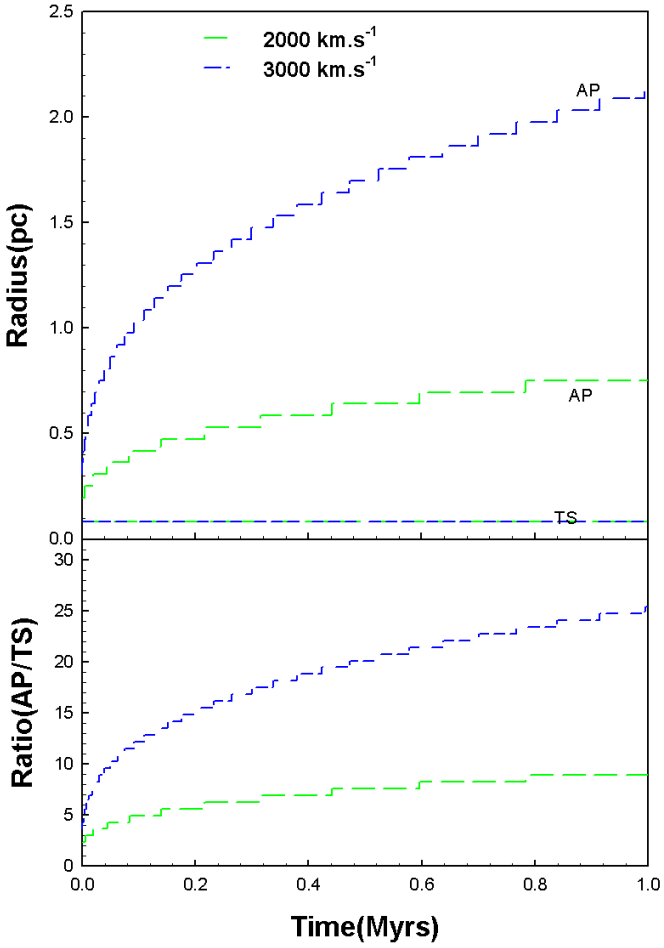

Figure 4.17: Similar to Figure 4.5, except for a mass-loss rate of 5×10^{-6} $M_{\odot}$ y^{-1}, and $\rho_{ISM} = 10^{-21}$ g cm^{-3}.

4.4 Summary and conclusions

In this chapter, stellar wind evolution of O- and B-type stars was simulated. Note that the model used in this work does not include the evolution of the stellar wind for the second (Red super giant, RSG) phase and the third (Wolf-Rayet, WR) phase (see e.g. section 2.4). This means that the results obtained from this model can only be used to discuss the state of the stellar wind cavity evolution up to the end of the main-sequence evolution. This depends on the mass and mass-loss rate of the star and could be $\sim$ 1-10 My, which is at the end of the simulation times presented in this work. For longer simulation times, these other two phases need to be taken into account.

The outflow speed for the RSG phase is much lower compared to the speed on the main-sequence, with the speed being in the range of 15 - 75 km s^{-1}, and it lasts for about 2×10^5 years (*Garcia-Segura et al.*, 1996a,b) after the main-sequence phase. However, for the WR phase, which follows the RSG phase, it is believed that the stellar mass-loss rate is higher than for the

main-sequence evolution in the range of 10^{-4} - 10^{-5} $M_\odot$ yr^{-1} (e.g. *Oey and Massey*, 1994), and with wind speeds of up to $\sim$ 4000 km s^{-1}. The RSG phase that creates a higher density bubble inside the low density main-sequence bubble may also contain the WR bubble at the end of the star's life. If in the case that the WR phase evolves further than the bubble created by the main-sequence evolution, the difference would not be great because the time period of the WR phase is negligible compared to that of the main-sequence phase.

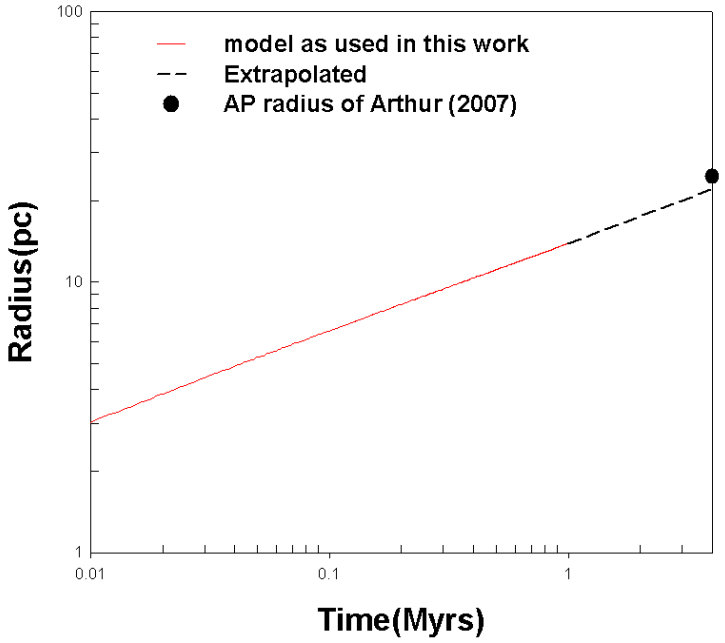

Figure 4.18: The time profile of the AP radius of model 22, on a log-log scale. Note, ρ_{ISM} = 10^{-25} g cm^{-3} in the model and a mass-loss rate of 10^{-6} $M_\odot$ y^{-1} and stellar wind speed of 1000 km s^{-1} are also assumed. The red line shows the AP radius as a function of time up to 1 My. The black line shows extrapolated values up to 4 My. The black circle shows the result of *Arthur* (2007).

To establish if this model results in calculations compatible with other stellar models, a comparison with those from *Arthur* (2007), as shown in Figure 4.1. Comparing results to Figure 4.1, it is found that for almost a similar set of parameters, the profile shown by the red solid line in Figure 4.12 is comparable with Figure 4.1. The two profiles do not compare at first sight, because the profile from *Arthur* (2007) was simulated over a longer time period. However, by extrapolating the AP radius of the red solid line in Figure 4.12 to a time period of (4×10^6 y), it is found that this profile nearly equals the profile obtained by the model used by *Arthur* (2007). This is shown in Figure 4.18, where *Arthur* (2007) calculated an AP distance of $\sim$ 25 pc after a simulation time of 4×10^6 y, the model in this work results in an AP distance of $\sim$ 22 pc by extrapolating the data to a simulation time of 4×10^6 y, as shown in Figure 4.18. This results in a difference of $\sim$ 10 % for a set of parameters not the same, but close to that of *Arthur* (2007). The red line in Figure 4.18 shows the calculations corresponding to model 22 in Table 4.1, with mass-loss rate of 10^{-6} $M_\odot$ y^{-1}, ISM density ρ_{ISM} = 10^{-25} g cm^{-3} and stellar wind speed of v =

1000 km s^{-1} and the dot the result of *Arthur* (2007).

The main aim of this chapter was to calculate and present the AP and TS distances as a function of time. We can summarize for Figures 4.7 to 4.13 that if the AP of a stellar wind with a speed of 2000 km s^{-1} was compared to the AP of a stellar wind with speed of 1000 km s^{-1} (having the same ISM density and mass-loss rate), the result was that the AP radius for the 1000 km s^{-1} wind scenario is $\sim$ 50% of that of the 2000 km s^{-1} wind scenario after a simulation time of 1 My. If the same was done for the 3000 km s^{-1} and 1000 km s^{-1} stellar wind scenarios, the result is that the AP radius for the 1000 km s^{-1} stellar wind is $\sim$ 33% of that of the 3000 km s^{-1} wind after 1 My. Doing the same with the 2000 km s^{-1} and 3000 km s^{-1} scenarios, the AP of the 2000 km s^{-1} stellar wind is $\sim$ 66% of that of the AP radius corresponding to a 3000 km s^{-1} stellar wind after 1 My. This was the case for all the different mass-loss rates and ISM densities considered in Figure 4.7 to Figure 4.13 and after a simulation time of 1 My.

The same followed by varying the stellar mass-loss rate. Comparing the computed AP radius corresponding to a stellar mass-loss rate of 10^{-6} $M_\odot$ y^{-1} to that of a stellar mass-loss rate of 5 $\times$ 10^{-6} $M_\odot$ y^{-1}, it followed that the AP radius corresponding to a stellar mass-loss rate of 10^{-6} $M_\odot$ y^{-1} is $\sim$ 60% that of the AP for a stellar mass-loss rate of 5 $\times$ 10^{-6} $M_\odot$ y^{-1}. Comparing a mass-loss rate scenario of 5 $\times$ 10^{-6} $M_\odot$ y^{-1} to that of 10^{-5} $M_\odot$ y^{-1}, it followed that the AP radius of the stellar mass-loss rate of 5 $\times$ 10^{-6} $M_\odot$ y^{-1} is $\sim$ 78% that of the AP radius for a stellar mass-loss rate of 10^{-5} $M_\odot$ y^{-1}. The AP radius for a stellar mass-loss rate of 10^{-6} $M_\odot$ y^{-1} is $\sim$ 46% that of a stellar mass-loss rate of 10^{-5} $M_\odot$ y^{-1}. This is the case for all parameter combinations and after a simulation time of 1 My.

For the case of the stellar wind evolving into a denser region in the ISM (e.g. molecular clouds), this investigation shows that by keeping the ambient density fixed at ρ_{ISM} = 10^{-22} g cm^{-3}, and changing the stellar wind speed from 2000 km s^{-1} to 3000 km s^{-1}, the AP radius for a stellar wind speed of 2000 km s^{-1} is $\sim$ 66 % compared to the AP radius for a stellar wind speed of 3000 km s^{-1}, for both mass-loss rates investigated. However, for ρ_{ISM} = 10^{-21} g cm^{-3}, the AP radius for a stellar wind speed of 2000 km s^{-1} is $\sim$ 40 % compared to the AP radius for a stellar wind speed of 3000 km s^{-1}, again for both mass-loss rates investigated. Secondly, by keeping the mass-loss rate fixed at 10^{-5} $M_\odot$ y^{-1} and changing the ambient density from ρ_{ISM} = 10^{-22} g cm^{-3} to ρ_{ISM} = 10^{-21} g cm^{-3}, the AP radius for ρ_{ISM} = 10^{-21} g cm^{-3} is $\sim$ 50 % compared to the AP radius for ρ_{ISM} = 10^{-22} g cm^{-3}, for a stellar wind speed of 3000 km s^{-1}. For a stellar wind speed of 2000 km s^{-1}, the AP radius for ρ_{ISM} = 10^{-21} g cm^{-3} is $\sim$ 33 % compared to the AP radius for ρ_{ISM} = 10^{-22} g cm^{-3}, when the density is decreased. For a mass-loss rate of 5 $\times$ 10^{-6} $M_\odot$ y^{-1} the AP radius for ρ_{ISM} = 10^{-21} g cm^{-3} is $\sim$ 20 % compared to the AP radius for ρ_{ISM} = 10^{-22} g cm^{-3}, for a stellar wind of 2000 km s^{-1}. Whereas for a stellar wind of 3000 km s^{-1} the AP radius for ρ_{ISM} = 10^{-21} g cm^{-3} is $\sim$ 33 % compared to the AP radius for ρ_{ISM} = 10^{-22} g cm^{-3}. These results were for both simulation times considered.

Lastly, Table 4.3 shows the computed AP distances obtained from this chapter, for the different parameters assumed. These are of importance in Chapter **6** where SNR evolution in these

cavities is considered. Note that not all combinations were investigated.

Table 4.3: Results for the AP distance in pc after a simulation time of 1 My.

$\dot{M}$ ($M_\odot$ y^{-1})	ρ_{ISM} (g cm^{-3})	v = 1000 km s^{-1}	v = 2000 km s^{-1}	v = 3000 km s^{-1}
10^{-5}	10^{-25}	28.0	68.0	
10^{-5}	10^{-24}	13.0	28.0	43.0
10^{-5}	10^{-23}	6.0	12.0	19.0
10^{-5}	10^{-22}	-	5.4	8.6
10^{-5}	10^{-21}	-	1.7	4.1
5×10^{-6}	10^{-25}	21.0	44.0	87.0
5×10^{-6}	10^{-24}	10.0	22.0	33.0
5×10^{-6}	10^{-23}	4.8	10.0	15.0
5×10^{-6}	10^{-22}	-	4.3	6.4
5×10^{-6}	10^{-21}	-	0.7	2.1
10^{-6}	10^{-25}	13.0	27.0	43.0
10^{-6}	10^{-24}	6.0	13.0	19.0
10^{-6}	10^{-23}	3.0	5.6	9.0

Chapter 5

Stellar winds II

5.1 Introduction

In this chapter, another important parameter in the evolution of stellar winds is introduced, which will result in different computed cavities compared to those calculated in the previous chapter. For example, in regions where supernova explosions are the main source of the structure and composition of the surrounding interstellar medium (ISM), the motion of the stars is nowhere near being stationary relative to that of the ISM (see Figure 5.1). The relative motion of stars in the vicinity of super massive black holes, for example, can reach values up to $\sim$ 1400 km s^{-1} (e.g. *Ghez et al.*, 1999), while for the Sun, the relative motion is $\sim$ 25 km s^{-1} (e.g. *Frisch*, 2007). This relative motion can be simulated in the model by keeping the star stationary and blowing the ISM wind over the stellar wind with different speeds (e.g. *Scherer and Ferreira*, 2005).

As in the previous chapter, the density profiles and time evolution of the astropause (AP) and termination shock (TS) will be shown and discussed. However, for the case of relative motion these profiles will be shown for both the nose and the tail region of the stellar wind. The nose region is defined as where the outflow of the stellar wind is in the opposite direction of the ISM "wind", while for the tail region, the outflow is along to ISM "wind" and a bullet-shaped structure is expected.

5.2 Density profiles for the case of relative motion

In this section, the density profiles of the stellar winds of massive stars are shown, as in Chapter **4**, but here relative motion is also included. Again the evolution into the ambient ISM and also the evolution into a more dense molecular cloud surrounding the star are treated separately. For the relative motion, three scenarios are chosen, namely speeds of 25 km s^{-1}, 100 km s^{-1} and 250 km s^{-1}. Where 25 km s^{-1} corresponds to the Sun, 250 km s^{-1} a factor of 10 faster and 100 km s^{-1} somewhere in between. These values represent most of the speeds of stars listed in the Hipparcos Catalogue (http://www.rssd.esa.int/SA-general/projects/Hipparcos).

Figure 5.1: This figure shows the structure of a stellar wind bubble around a young hot star in the bottom left corner. It shows a clear bullet-shape structure, indicating relative motion between the star and the ISM. From http://hubblesite.org/gallery/album/pr2004026a/. Picture was taken in 2002 with Hubble's Wide Field Planetary Camera 2.

5.2.1 Density profiles for stellar wind evolution into the ambient ISM

Table 5.1: Parameter for stellar wind-ISM interaction for the ambient ISM

Model	$\dot{M}$ **(M$_\odot$ y^{-1})**	v (km s^{-1})	v_{rel} (km s^{-1})	ρ_{ISM} (g cm^{-3})
1	10^{-6}	2000	25	10^{-25}
2	10^{-6}	2000	100	10^{-25}
3	10^{-6}	2000	250	10^{-25}
4	10^{-6}	2000	25	10^{-24}
5	10^{-6}	2000	100	10^{-24}
6	10^{-6}	2000	250	10^{-24}
7	10^{-5}	2000	25	10^{-25}
8	10^{-5}	2000	100	10^{-25}
9	10^{-5}	2000	250	10^{-25}
10	10^{-5}	2000	25	10^{-24}
11	10^{-5}	2000	100	10^{-24}
12	10^{-5}	2000	250	10^{-24}

Table 5.1 shows a combination of different parameters that result in different computed scenarios to be compared with each other in order to illustrate the effect of relative motion of a star in the ambient ISM. Column 1 shows the different scenarios as models 1-12, column 2 shows the different mass-loss rates in units of M$_\odot$ y^{-1}, column 3 shows the stellar wind speeds in units of km s^{-1}, column 4 shows the relative speed also in units of km s^{-1} and column 5 shows the ambient density in units of g cm^{-3}. Different to the previous chapter is that the outflow speed is not varied here, but kept constant at 2000 km s^{-1}.

Shown in Figure 5.2 are different computed density profiles that were computed by changing

the ISM density, relative speed and the stellar wind mass-loss rate, while keeping the stellar wind speed fixed at 2000 km s^{-1}. Three different relative speeds are assumed, namely 25 km s^{-1} (column 1), 100 km s^{-1} (column 2) and 250 km s^{-1} (column 3). In the first row, mass-loss rates of 10^{-6} $M_\odot$ y^{-1} and ρ_{ISM} = 10^{-25} g cm^{-3} (models 1-3 in Table 5.1) are assumed in the model. From the second row ρ_{ISM} = 10^{-24} g cm^{-3} is assumed with the same mass-loss rate of 10^{-6} $M_\odot$ y^{-1} (see models 4-6 in Table 5.1). The third row shows the computed profiles for mass-loss rates of 10^{-5} $M_\odot$ yr^{-1} and ρ_{ISM} = 10^{-25} g cm^{-3} (models 7-9 in Table 5.1) and lastly the fourth row corresponds to the same mass-loss rate of 10^{-5} $M_\odot$ yr^{-1} in the model, but with ρ_{ISM} = 10^{-24} g cm^{-3} (models 10-12 in Table 5.1). The nose region is shown by the right side of the density profiles (0 to 100 pc) and the tail region is shown by the left side of the density profiles (0 to -100 pc).

From the density profiles shown in Figure 5.2 it follows that the relative motion of the star inside its surrounding ISM plays an important role in the evolution of the stellar wind. For example, as shown by the first row of Figure 5.2, it is clear how the relative motion between the ISM and the star results in different computed profiles in the nose and tail regions. Firstly, for the nose region the different panels in the first row show that by increasing the relative motion from 25 km s^{-1} (column 1) to 250 km s^{-1} (column 3), the AP is compressed (decreases), while the transition between stellar and ISM material in the tail direction is elongated (increases). Secondly, Figure 5.2 shows that as the relative motion is increased, the transition region between the stellar wind and the ISM in the tail region becomes less distinct, as can be seen from e.g. panels (a) and (c). Where panel (a) shows a distinct AP for a 25 km s^{-1} relative speed in the tail direction, for a relative speed of 250 km s^{-1} (panel c) there is no sudden increase in the density profiles, making it difficult to define a distinct AP.

For this reason, what is called the boundary for the tail region (the AP) must be redefined. In this work, such a position is defined as where the density is 50 % of that of the ISM density. This assumption is necessary because of the difficulty to define a definite AP in the tail from the density profiles only. This value is chosen to make sure that only stellar material is considered. For panels (b) and (i), for example, this assumption may not necessarily correspond to the actual transition between stellar and undisturbed ISM material, but for panels (g) and (j), for example, this assumption is more accurate. Therefore, whenever the term boundary or AP is used for the tail region, note that this reference does not necessarily correspond to what actually can be called the transition between stellar and ISM material, but rather the position where the density is 50 % that of the ISM.

In panel (a) in Figure 5.2 it follows that, after a time period of 900 $\times$ 10^3 y, the AP in the nose direction is at a distance of $\sim$ 25 pc for a relative speed of 25 km s^{-1} and at a distance of $\sim$ 30 pc in the tail direction. Thus, for a relative speed of 25 km s^{-1}, what is called the AP in the tail region, is larger than the AP in the nose region by a factor of $\sim$ 1.4. For a relative speed of 100 km s^{-1}, for the same time period, the AP in the nose direction is at a distance of $\sim$ 18 pc and at a distance of $\sim$ 30 pc in the tail direction. Thus, for a relative speed of a 100 km s^{-1}

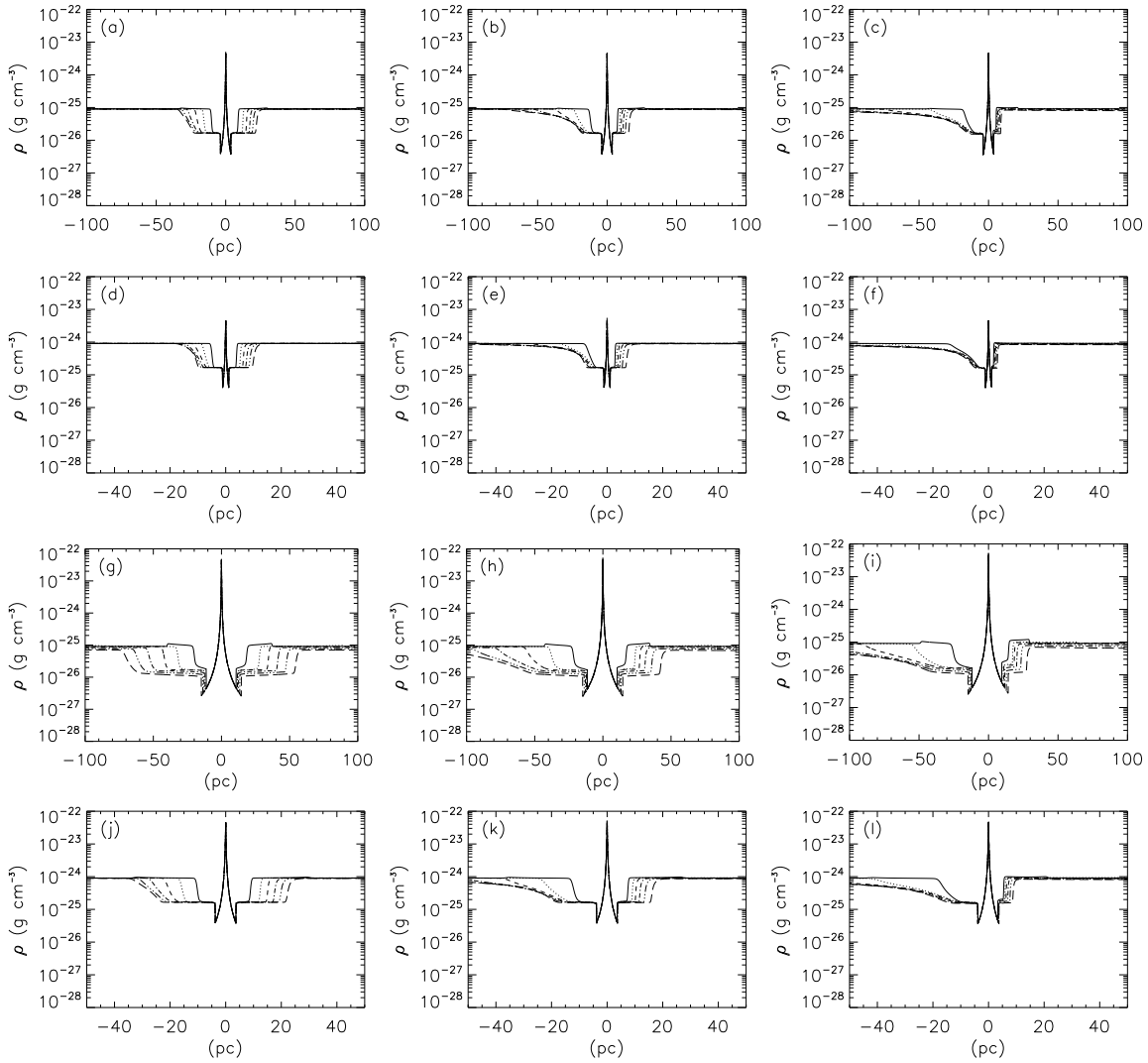

Figure 5.2: Computed density profiles of a star with relative motion compared to that of the ISM. Computations are shown in both the nose and the tail directions respectively. The first row corresponds to a mass-loss rate of 10^{-6} $M_\odot$ y^{-1} and ρ_{ISM} = 10^{-25} g cm^{-3} assumed in the model. The second row corresponds to a mass-loss rate of 10^{-6} $M_\odot$ y^{-1} and ρ_{ISM} = 10^{-24} g cm^{-3}. The third row corresponds to a mass-loss rate of 10^{-5} $M_\odot$ y^{-1} and ρ_{ISM} = 10^{-25} g cm^{-3}. The last row corresponds to a mass-loss rate of 10^{-5} $M_\odot$ y^{-1} and ρ_{ISM} = 10^{-24} g cm^{-3} assumed in the model. The different columns denote different relative speeds, where column 1 corresponds to a relative speed of 25 km s^{-1}, column 2 to 100 km s^{-1} and column 3 to a relative speed of 250 km s^{-1} assumed in the model. The different lines shown in each panel correspond to 50, 150, 300, 500, 700 and 900 $\times$ 10^3 y respectively. For all panels, a stellar wind speed of 2000 km s^{-1} is assumed.

what is called the AP in the tail region is greater than the AP in the nose region by a factor of $\sim$ 1.66. For a relative speed of 250 km s^{-1}, the AP in the nose direction is at a distance of $\sim$ 6 pc and at a distance of $\sim$ 30 pc in the tail direction, indicating that the AP in the tail region is greater than the AP in the nose region by a factor of $\sim$ 5.0. Thus, the relative motion between the stellar wind and the ISM has a significant influence on the evolution of the stellar wind.

The same trend is also seen in the other rows of Figure 5.2. Compared to row 1 (models 1-3), the cavities (AP distances) are smaller (row 2, models 4-6), larger (row 3, models 7-9) or the same (row 4, models 10-12) depending on the mass-loss rate and ISM density. The cavities in

row 2 are smaller because the ISM density is higher compared to row 1, and the cavities in row 3 are larger compared to row 1 because the mass-loss rate is higher. The AP distance in row 1 and row 4 is the same because in row 1 the ISM density is a factor of 10 lower compared to row 4, but for row 4 the mass-loss rate is a factor of 10 higher compared to row 1. This indicates that one has to be careful making conclusions because two different sets of parameters result in similar computed profiles.

Next, comparisons will be made between AP in the nose region, assuming the same relative speed, but varying the ISM densities and mass-loss rates. Firstly, row 1 is compared with row 2, where row 1 shows results for ρ_{ISM} = 10^{-25} g cm^{-3} and a mass-loss rate of 10^{-6} M$_\odot$ y^{-1}, while row 2 shows results assuming ρ_{ISM} = 10^{-24} g cm^{-3} and a mass-loss rate of 10^{-6} M$_\odot$ y^{-1}. For a relative speed of 25 km s^{-1}, the AP in the nose region, with an ISM density of 10^{-24} g cm^{-3}, is at a distance of $\sim$ 10 pc (panel d), whereas the AP in the nose direction with ρ_{ISM} = 10^{-25} g cm^{-3} is at a distance of $\sim$ 25 pc (panel a). Thus, for ρ_{ISM} = 10^{-25} g cm^{-3}, the AP is greater than the AP for ρ_{ISM} = 10^{-24} g cm^{-3} by a factor $\sim$ 2.5 in the nose region.

For the tail region, the AP (as defined above) assuming a relative speed of 25 km s^{-1} for ρ_{ISM} = 10^{-24} g cm^{-3} is at a distance of $\sim$ 12 pc (panel d in Figure 5.2), whereas the AP in the tail for ρ_{ISM} = 10^{-25} g cm^{-3} is at a distance of $\sim$ 30 pc (panel a in Figure 5.2). Thus, for ρ_{ISM} = 10^{-25} g cm^{-3}, the AP radius is larger than the AP radius for ρ_{ISM} = 10^{-24} g cm^{-3} also by a factor $\sim$ 2.5, similar to the nose.

Next, the nose and the tail regions for the same ISM density, but different mass-loss rates are compared, e.g. row 1 with row 3. Row 1 shows results assuming a mass-loss rate of 10^{-6} M$_\odot$ y^{-1} and row 3 shows results assuming a mass-loss rate of 10^{-5} M$_\odot$ y^{-1}. First concentrate only on column 1 where ρ_{ISM} = 10^{-25} g cm^{-3} and a relative speed of 25 km s^{-1} assumed in the model. The AP in the nose region of panel (a) is at a distance of $\sim$ 25 pc, whereas the AP in the nose region of panel (g) is at a distance of $\sim$ 55 pc. Thus, for a mass-loss rate of 10^{-5} M$_\odot$ y^{-1}, the AP is greater than the AP for a mass-loss rate of 10^{-6} M$_\odot$ y^{-1} by a factor $\sim$ 2.2 in the nose region. As for the tail region, the AP is at a distance of $\sim$ 30 pc (panel a) for a mass-loss rate of 10^{-6} M$_\odot$ y^{-1}, whereas the AP is at a distance of $\sim$ 68 pc (panel g) for a mass-loss rate of 10^{-5} M$_\odot$ y^{-1}. Thus, for a mass-loss rate of 10^{-5} M$_\odot$ y^{-1}, the AP is greater than the AP for a mass-loss rate of 10^{-6} M$_\odot$ y^{-1} by a factor $\sim$ 2.2.

Next, values in the nose region are compared for ρ_{ISM} = 10^{-24} g cm^{-3} and a mass-loss rate of 10^{-5} M$_\odot$ y^{-1} (row 4), but different relative speeds. The AP is at a distance of $\sim$ 25 pc (panel j) for a relative speed of 25 km s^{-1}, whereas the AP is at a distance of $\sim$ 10 pc (panel l) for a relative speed of 250 km s^{-1}. Thus, for a relative speed of 25 km s^{-1} , the AP radius in the nose direction is larger than the AP for a relative speed of 250 km s^{-1} by a factor of $\sim$ 2.5. These factor differences are in the same order as those above, indicating that the relative speed is also an important parameter in calculating stellar wind evolution.

5.2.2 Density profiles for stellar wind evolution of an embedded star

Table 5.2: Parameter for stellar wind-ISM interaction for embedded stars

Model	$\dot{M}$ ($M_\odot$ y^{-1})	V_{SW} (km s^{-1})	V_{Rel}(km s^{-1})	ρ_{ISM} (g cm^{-3})
1	10^{-5}	2000	25	10^{-22}
2	10^{-5}	2000	100	10^{-22}
3	10^{-5}	2000	250	10^{-22}
4	10^{-5}	2000	25	10^{-21}
5	10^{-5}	2000	100	10^{-21}
6	10^{-5}	2000	250	10^{-21}
7	5×10^{-6}	2000	25	10^{-22}
8	5×10^{-6}	2000	100	10^{-22}
9	5×10^{-6}	2000	250	10^{-22}
10	5×10^{-6}	2000	25	10^{-21}
11	5×10^{-6}	2000	100	10^{-21}
12	5×10^{-6}	2000	250	10^{-21}

Table 5.2 shows the same as Table 5.1, the only difference is that the ambient density for these scenarios is taken as 10^{-22} g cm^{-3} and 10^{-21} g cm^{-3} respectively.

Shown in Figure 5.3 are different sets of computed density profiles in the case where the star is embedded inside a medium with high densities, e.g. a molecular cloud. The first row shows the computed density profiles assuming a mass-loss rate of 10^{-5} $M_\odot$ y^{-1} and cloud density of 10^{-22} g cm^{-3} (see models 1-3 in Table 5.2), the second row corresponds to the same parameters except that the density of the cloud is taken as 10^{-21} g cm^{-3} (models 4-6 in Table 5.2). For the third row, a mass-loss rate of 5×10^{-6} $M_\odot$ y^{-1} and ρ_{ISM} = 10^{-22} g cm^{-3} are assumed (models 7-9). Lastly, for row 4 a mass-loss rate of 5×10^{-6} $M_\odot$ y^{-1} and ρ_{ISM} = 10^{-21} g cm^{-3} (models 10-12) is assumed. For all these a stellar wind speed of 2000 km s^{-1} is assumed. Column 1 corresponds to a relative speed of 25 km s^{-1}, column 2 to 100 km s^{-1} and column 3 to 250 km s^{-1} as assumed in the model.

The profiles in Figure 5.3 show the same structure as the profiles in Figure 5.2. However, in Figure 5.2, the ambient densities are assumed to be ρ_{ISM} = 10^{-25} g cm^{-3} and ρ_{ISM} = 10^{-24} g cm^{-3} respectively, while in Figure 5.3 the ambient densities are assumed to be ρ_{ISM} = 10^{-22} g cm^{-3} and ρ_{ISM} = 10^{-21} g cm^{-3}. In the case of high ISM density, the TS and AP form closer to the star, as can be seen by comparing these figures. Also seen from these figures, especially from column 3, is that for these higher densities the AP and TS are not clearly visible due to smaller values, although the range of the x-axis was decreased compared to Figure 5.2.

From Figure 5.3, row 1 follows that, after a time period of 900 $\times$ 10^3 y, the AP in the nose direction is at a distance of $\sim$ 5 pc (panel a in Figure 5.3) for a relative speed of 25 km s^{-1} and at a distance of $\sim$ 5.5 pc in the tail direction. Thus, for a relative speed of 25 km s^{-1} the AP, in the tail region, is greater than the AP in the nose region by a factor of $\sim$ 1.1. Taking the relative speed as 100 km s^{-1}, for the same time period, the AP in the nose direction is at a distance of $\sim$ 3.5 pc (panel b in 5.3) and at a distance of $\sim$ 5 pc in what is defined as the tail direction. Thus, for a relative speed of a 100 km s^{-1}, the AP in the tail region is greater than the AP in the nose

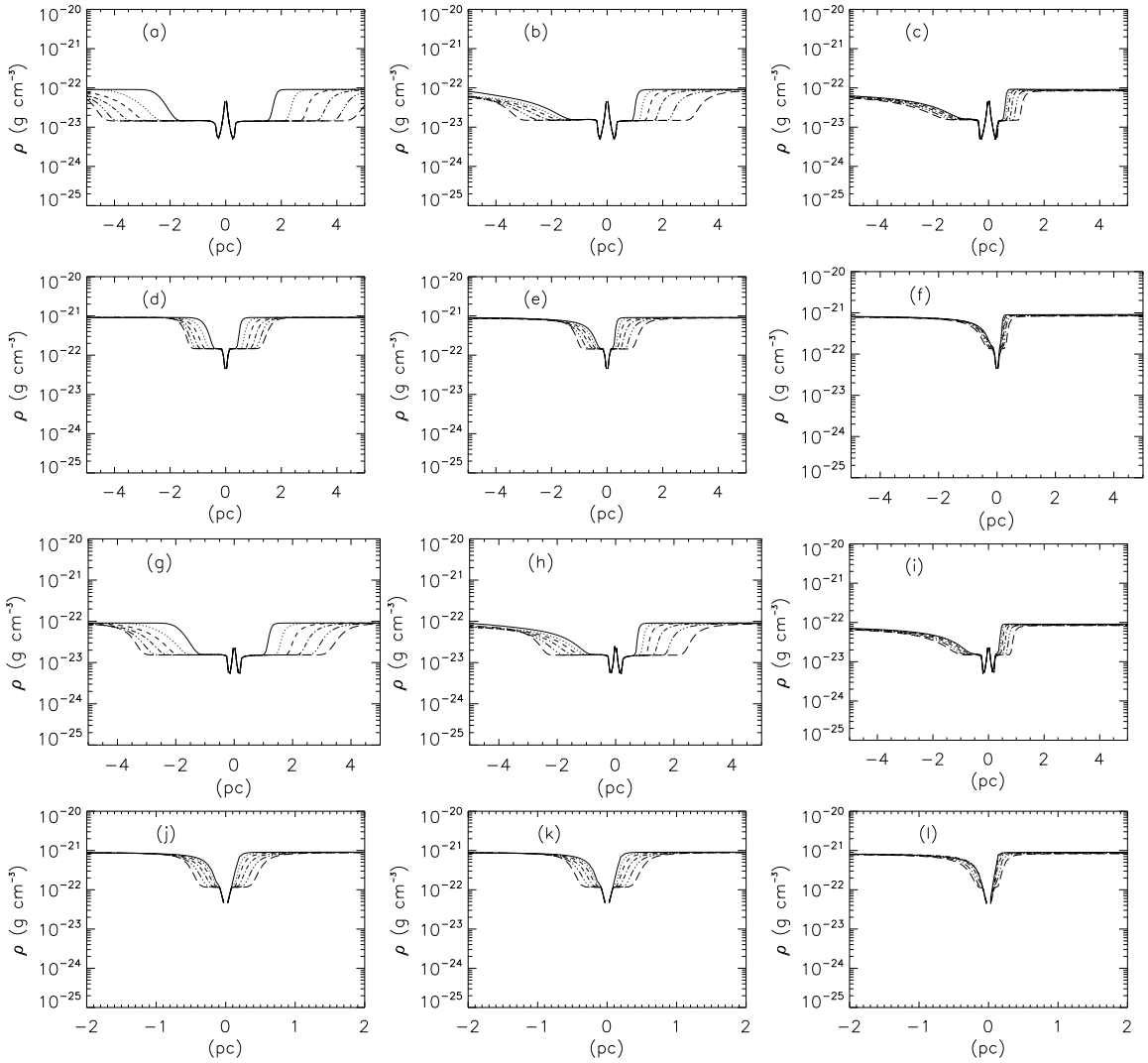

Figure 5.3: Same as Figure 5.2, except that the first row corresponds to model calculations assuming a mass-loss rate of 10^{-5} $M_\odot$ y^{-1} and $\rho_{ISM} = 10^{-22}$ g cm^{-3}. The second row corresponds to a mass-loss rate of 10^{-5} $M_\odot$ y^{-1} and $\rho_{ISM} = 10^{-21}$ g cm^{-3}. The third row corresponds to a mass-loss rate of 5×10^{-6} $M_\odot$ y^{-1} and $\rho_{ISM} = 10^{-22}$ g cm^{-3} in the model. The last row corresponds to a mass-loss rate of 5×10^{-6} $M_\odot$ y^{-1} and $\rho_{ISM} = 10^{-21}$ g cm^{-3}. Note that the range on the x-scale differs compared to Figure 5.2.

region by a factor of ~ 1.5. For a relative speed of 250 km s^{-1} assumed in the model, the AP in the nose direction is at a distance of ~ 1.5 pc (panel c in Figure 5.3) and at a distance of ~ 6 pc in the tail direction, showing that the AP in the tail region (as defined earlier) is greater than the AP in the nose region by a factor of ~ 4. From this figure one can also conclude that by increasing the relative motion between the stellar wind and the ISM, there will be significant changes in the evolution of the stellar wind into the ISM.

Next, values in the nose region are compared for $\rho_{ISM} = 10^{-22}$ g cm^{-3} and a mass-loss rate of 5×10^{-5} $M_\odot$ y^{-1} (row 3), but different relative speeds. The AP is at a distance of ~ 4 pc (panel g in Figure 5.3) for a relative speed of 25 km s^{-1}, whereas the AP is at a distance of ~ 2.8 pc (panel h in Figure 5.3) for a relative speed of 100 km s^{-1}, and at a AP distance of ~ 1 pc (panel

i in Figure 5.3) for a relative speed of 250 km s^{-1}. Thus, for a relative speed of 25 km s^{-1} , the AP is larger compared to the AP for a relative speed of 250 km s^{-1} by a factor of ~ 4.

These cavities shown in Figure 5.3 are much smaller compared to the cavities in Figure 5.2, because the ambient ISM density is much higher. The cavities also differ (become smaller) as the ambient ISM density is increased from 10^{-22} g cm^{-3} (row 1) to 10^{-21} g cm^{-3} (row 2). The same happens if the ambient ISM density is kept the same, but the mass-loss rate is decreased from 10^{-5} $M_\odot$ y^{-1} (row 1) to 5×10^{-6} $M_\odot$ y^{-1} (row 3), and becomes even smaller when the ambient ISM density is changed from 10^{-22} g cm^{-3} (row 3) to 10^{-21} g cm^{-3} (row 4) for a mass-loss rate of 5×10^{-6} $M_\odot$ y^{-1}.

5.3 Evolution of stellar wind structures

Just as before time profiles are shown next, which show the evolution of the termination shock (TS) and boundary (AP) as a function of time. The only difference is that these profiles include relative motion of the ISM, which was not included in the previous chapter.

5.3.1 Evolution into the ambient ISM

Shown by Figure 5.4 are the time profiles showing the evolution of the AP and TS as a function of time for the nose region (left panel) and tail region (right panel). These time profiles show the same as those shown in the previous chapter, but note that in these figures the different scenarios shown correspond to different relative speeds. The blue (short dashed) line corresponds to AP and TS distances assuming a relative speed of 25 km s^{-1}, the green (long dashed) line corresponds to a relative speed of 100 km s^{-1} and lastly the red (solid) line corresponds to a relative speed of 250 km s^{-1}. The top panels show the position of these structures and the bottom panels the ratio.

Figure 5.4 shows the AP and TS radii for the case of a mass-loss rate of 10^{-6} $M_\odot$ y^{-1} and ρ_{ISM} = 10^{-25} g cm^{-3}. Results are shown for three different relative speeds, corresponding to row 1 in Figure 5.2. The same is shown in Figure 5.5, where the mass-loss rate is the same as assumed in the model to produce Figure 5.4, but ρ_{ISM} = 10^{-24} g cm^{-3}. These correspond to row 2 in Figure 5.2.

From Figure 5.5 (row 2 in Figure 5.2) it follows that, after a time period of 1 My, the AP in the nose direction (left panel) is at a distance of $\sim$ 25 pc for a relative speed of 25 km s^{-1} and at a distance of $\sim$ 16 pc for a relative speed of 100 km s^{-1}. Thus, for a relative speed of 25 km s^{-1}, the AP is larger than the AP for a relative speed of 100 km s^{-1} by a factor of ~ 1.5. For a relative speed of 250 km s^{-1}, for the same time period, the AP in the nose direction is at a distance of $\sim$ 6 pc . Thus, the AP in the nose region for a relative speed of a 25 km s^{-1} is greater than the AP for a relative speed of 250 km s^{-1} by a factor of ~ 4.

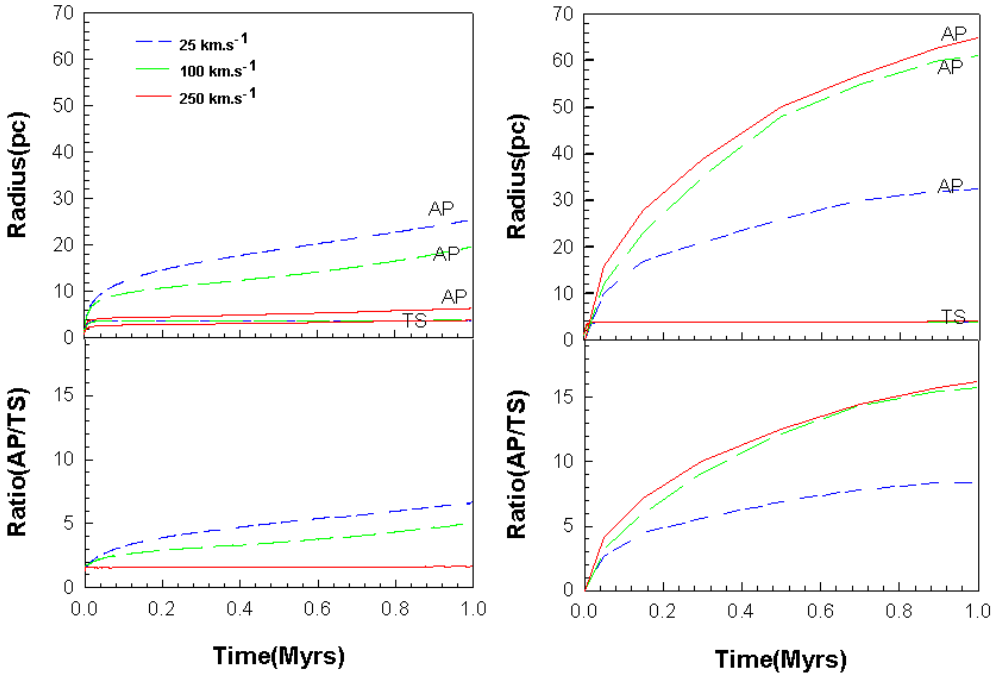

Figure 5.4: The time profiles of the AP and TS radii with relative motion with respect to the ambient ISM. The left panel shows the time profile of the stellar wind in the nose direction and the right panel shows the time profile in the tail direction. The mass-loss rate is 10^{-6} $M_{\odot}$ y^{-1} and ρ_{ISM} = 10^{-25} g cm^{-3}. The blue line (short dashed) correspond to a relative speed of 25 km s^{-1}, the green line (long dashed) correspond to a relative speed of 100 km s^{-1} and the red (solid) line correspond to a relative speed of 250 km s^{-1}. All of these stellar winds have outflow speed of 2000 km s^{-1}.

By comparing Figure 5.4 with Figure 5.5 (left panel) follows that increasing the ISM density will result in the AP forming closer to the star (in the nose direction). The AP for the scenario with a mass-loss rate of 10^{-6} $M_{\odot}$ y^{-1} and ρ_{ISM} = 10^{-24} g cm^{-3} (Figure 5.5) forms at a distance of $\sim$ 13 pc with relative speed of 25 km s^{-1}. As for the case with a ρ_{ISM} = 10^{-25} g cm^{-3} (Figure 5.4) with the same mass-loss rate, the AP forms at a distance of $\sim$ 25 pc with a relative speed of 25 km s^{-1}. This corresponds to an increase of a factor of $\sim$ 2, for a relative speed of 25 km s^{-1}. If a relative speed of 100 km s^{-1} is assumed, the AP distance for ρ_{ISM} = 10^{-24} g cm^{-3} is $\sim$ 8 pc, whereas for ρ_{ISM} = 10^{-25} g cm^{-3} the AP distance is $\sim$ 18 pc. This corresponds to an increase of a factor of $\sim$ 2.2. As for the case of a relative speed of 250 km s^{-1}, the AP distance for ρ_{ISM} = 10^{-24} g cm^{-3} is $\sim$ 2 pc and for ρ_{ISM} = 10^{-25} g cm^{-3} it is $\sim$ 5 pc. This corresponds to an increase of a factor of $\sim$ 2.5 if the ISM density is decreased from ρ_{ISM} = 10^{-24} g cm^{-3} to ρ_{ISM} = 10^{-25} g cm^{-3}. This shows that the factor with which the AP increases, by decreasing the ISM density, increases as the relative speed is increased.

For the tail region (right panels), these profiles differ because the outflow is along the flow of the ISM. The AP, as it was defined earlier, for the case of relative speed of 25 km s^{-1} (blue short dashed line), expands further with time compared to the nose direction. If the relative speed is increased to 100 km s^{-1} (green long dashed line), the AP expands even further. Increasing

the relative speed even more to 250 km s^{-1} results in the AP expanding even further than before. The influence of the relative speed between the star and ISM can be seen by comparing e.g. Figure 5.4 to Figure 4.12 in Chapter **4**, where no relative speed is assumed but the same parameters are used in the blue curve of Figure 4.12.

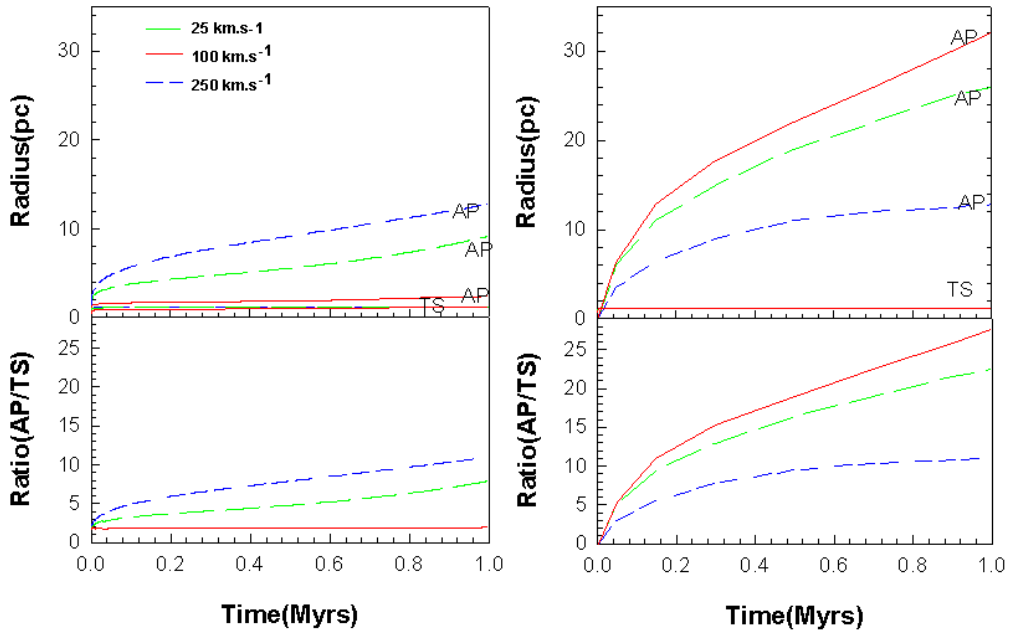

Figure 5.5: Same as Figure 5.4, but with mass-loss rate of 10^{-6} $M_\odot$ y^{-1} and ρ_{ISM} = 10^{-24} g cm^{-3}.

As for the case of a higher mass-loss rate of 10^{-5} $M_\odot$ y^{-1}, the left panels of Figure 5.6 (corresponding to row 3 in Figure 5.2) and Figure 5.7 (corresponding to row 4 in Figure 5.2) show that by increasing the ISM density, the AP also forms closer to the star in the nose and tail direction. However, comparing Figures 5.4 to 5.7 shows that, when increasing the mass-loss rate of the stellar wind, the AP forms at larger distances, due to the increase in stellar wind pressure. Also, comparing different panels in the same row from Figure 5.2, by increasing the relative motion from 25 km s^{-1} to 100 km s^{-1} to 250 km s^{-1}, the AP forms closer and closer to the star in the nose direction. This happens because as the speed of the ISM wind relative to that of the stellar wind increases, the pressure of the ISM that is exerted on the stellar wind increases causing the AP distance to increase (or decrease) as the relative speed of the ISM wind is decreased (or increased).

Shown by the right panels of Figure 5.6 and Figure 5.7 (both with a mass-loss rate of 10^{-5} $M_\odot$ y^{-1} assumed in the model) is that the time profile in the tail direction for ρ_{ISM} = 10^{-25} g cm^{-3} (Figure 5.6) expands faster compared to the case when ρ_{ISM} = 10^{-24} g cm^{-3} (Figure 5.7), where the AP in the tail region for ρ_{ISM} = 10^{-25} g cm^{-3} is at a distance of $\sim$ 66 pc, whereas for ρ_{ISM} = 10^{-24} g cm^{-3} the AP is at a distance of $\sim$ 30 pc, resulting in a factor of $\sim$ 2.2 difference. The same applies for the change in stellar mass-loss rate and keeping ρ_{ISM} = 10^{-25} g cm^{-3}. This

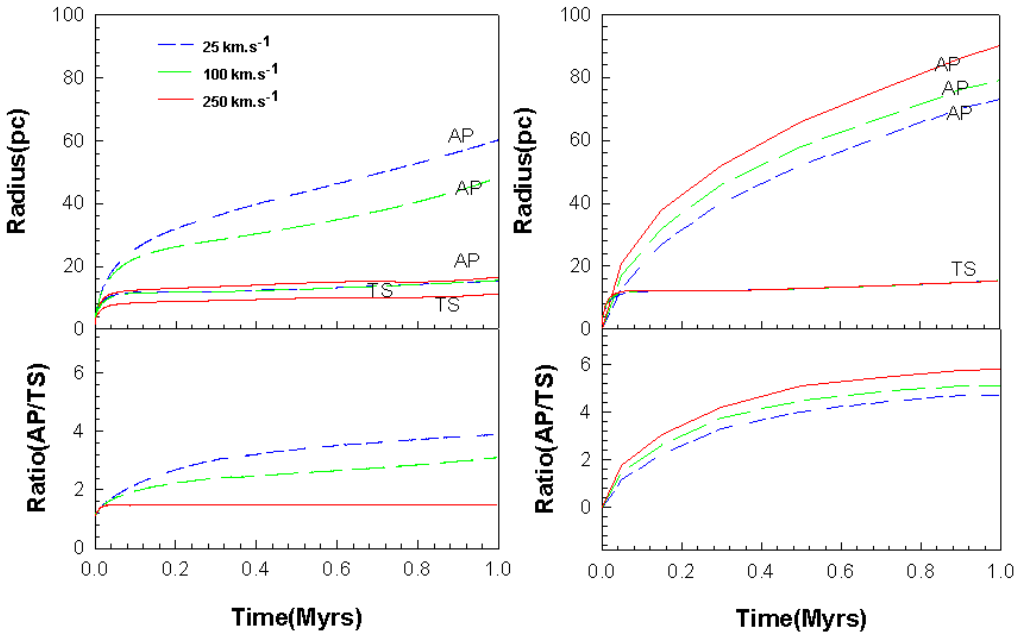

Figure 5.6: Same as Figure 5.4, except with a mass-loss rate of 10^{-5} $M_{\odot}$ y^{-1} and $\rho_{ISM} = 10^{-25}$ g cm^{-3}.

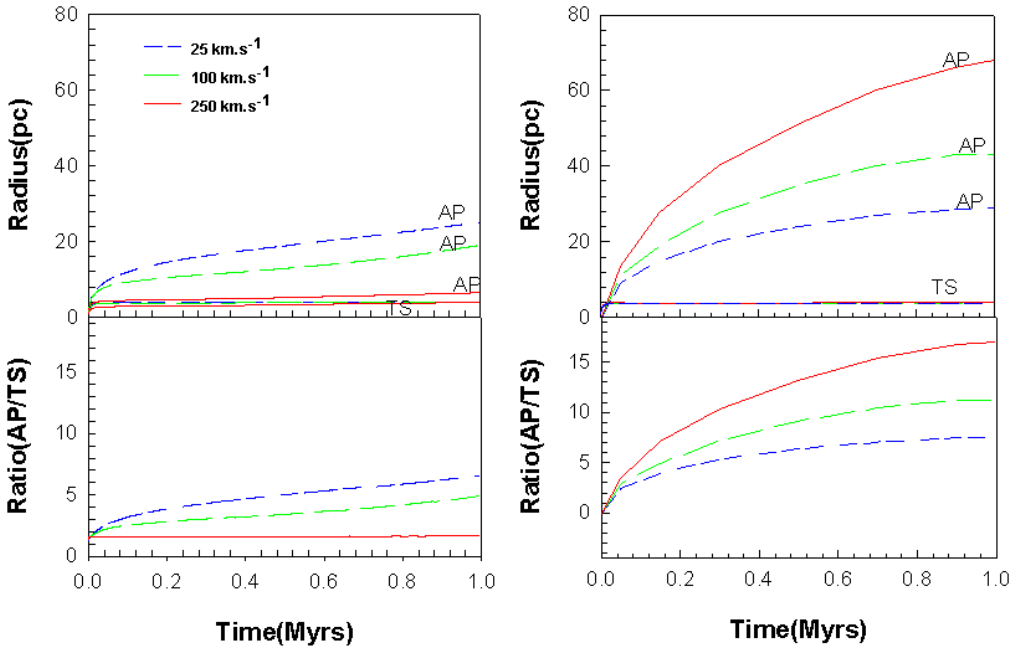

Figure 5.7: Same as Figure 5.4, except with a mass-loss rate of 10^{-5} $M_{\odot}$ y^{-1} and $\rho_{ISM} = 10^{-24}$ g cm^{-3}.

can be seen when comparing Figure 5.4 and Figure 5.6 the higher the mass-loss rate the further the AP in the tail region expands, for a given simulation time.

Just as before, by keeping the mass-loss rate the same (10^{-5} $M_{\odot}$ y^{-1}) and changing ρ_{ISM} from

10^{-25} g cm^{-3} (row 3 in Figure 5.2) to 10^{-24} g cm^{-3} (row 4 in Figure 5.2), the distance of the AP in the nose direction for ρ_{ISM} = 10^{-24} g cm^{-3} increases by a factor of $\sim$ 2.5, when the density is decreased to ρ_{ISM} = 10^{-25} g cm^{-3}. The same applies for the case of a mass-loss rate of 10^{-6} M$_\odot$ y^{-1}, where the distance of the AP in the nose direction for the case of ρ_{ISM} = 10^{-24} g cm^{-3} increases by a factor of $\sim$ 2.2, when the density is decreased to ρ_{ISM} = 10^{-25} g cm^{-3}. These results are the same for all these different relative speeds investigated.

Next, the mass-loss rate is changed and the ISM density is kept fixed. The difference between the AP for a mass-loss rate of 10^{-6} M$_\odot$ y^{-1} and 10^{-5} M$_\odot$ y^{-1} for both ρ_{ISM} = 10^{-25} (row 1 and row 3) and ρ_{ISM} = 10^{-24} g cm^{-3} (row 2 and row 4), shows that the distance of the AP radius in the nose direction for a mass-loss rate of 10^{-5} M$_\odot$ y^{-1} is a factor of $\sim$ 2.2 larger compared to that of the AP distance for a mass-loss rate of 10^{-6} M$_\odot$ y^{-1} for a relative speed of 25 km s^{-1}. If the relative speed is increased to 100 km s^{-1}, the factor increases to a value of $\sim$ 2.5, while for a relative speed of 250 km s^{-1}, the factor increases to a value of $\sim$ 3.

Using the distances obtained from Figures 5.4 to 5.7, it can be summarized as to how the relative speed influences the position of the AP. First, by comparing the difference between a stationary stellar wind and a stellar wind with a relative speed of 25 km s^{-1}, the result is that the AP of a stellar wind with a relative speed of 25 km s^{-1} forms at a distance that is a factor $\sim$ 0.9 the distance for the case for no relative speed in the nose direction after 1 My. This applies for models 1, 4, 7 and 10 from Table 5.1. For the case of a relative speed of 100 km s^{-1}, the AP radius is a factor of $\sim$ 0.7 the distance compared to the AP radius of a stellar wind with no relative speed (see models 2, 5, 8 and 11 in Table 5.1). As for the case of a relative speed of 250 km s^{-1}, the AP radius is a factor of $\sim$ 0.25 compared to the AP radius for the case for no relative speed in the nose direction (see models 3, 6, 9 and 12 in Table 5.1). This indicates that this parameter is important in the stellar wind evolution.

5.3.2 Evolution inside a molecular cloud

Shown in Figures 5.8 to 5.11 are time profiles corresponding to the evolution of stellar wind for a star embedded within a dense molecular cloud, which also includes relative motion. The left panel shows the profiles in the nose region and the right panel shows the profiles in the tail region. The same relative speeds are assumed for these scenarios as done for the previous section, namely 25 km s^{-1}, 100 km s^{-1} and 250 km s^{-1}. However, for these scenarios the stellar wind expands into a molecular cloud with the ambient ISM density assumed to be 10^{-22} and 10^{-21} g cm^{-3} respectively. The AP in the nose direction forms closer to the star, because of the high density of the cloud within which the star is embedded. The same applies for the time profiles in the tail region (right panel).

From these figures it follows that the time profiles for these scenarios expand slower compared to the figures from the previous section. The AP radius expands the fastest and farthest with a mass-loss rate of 10^{-5} M$_\odot$ y^{-1}, ISM density 10^{-22} g cm^{-3} and stellar wind speed of 2000 km

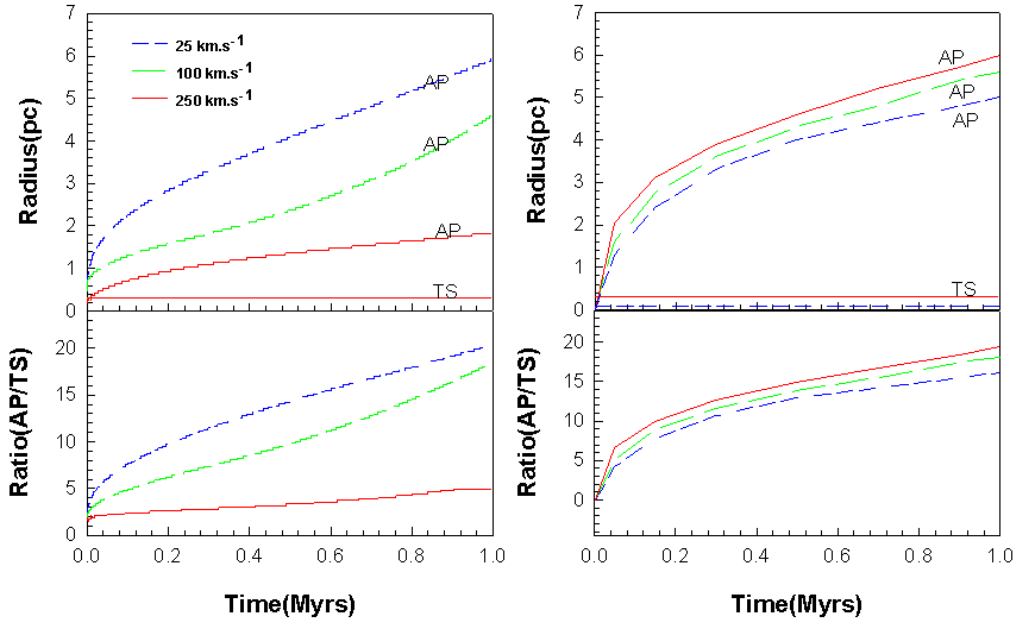

Figure 5.8: Same as Figure 5.4, except with a mass-loss rate of 10^{-5} $M_{\odot}$ y^{-1} and ρ_{ISM} = 10^{-22} g cm^{-3}.

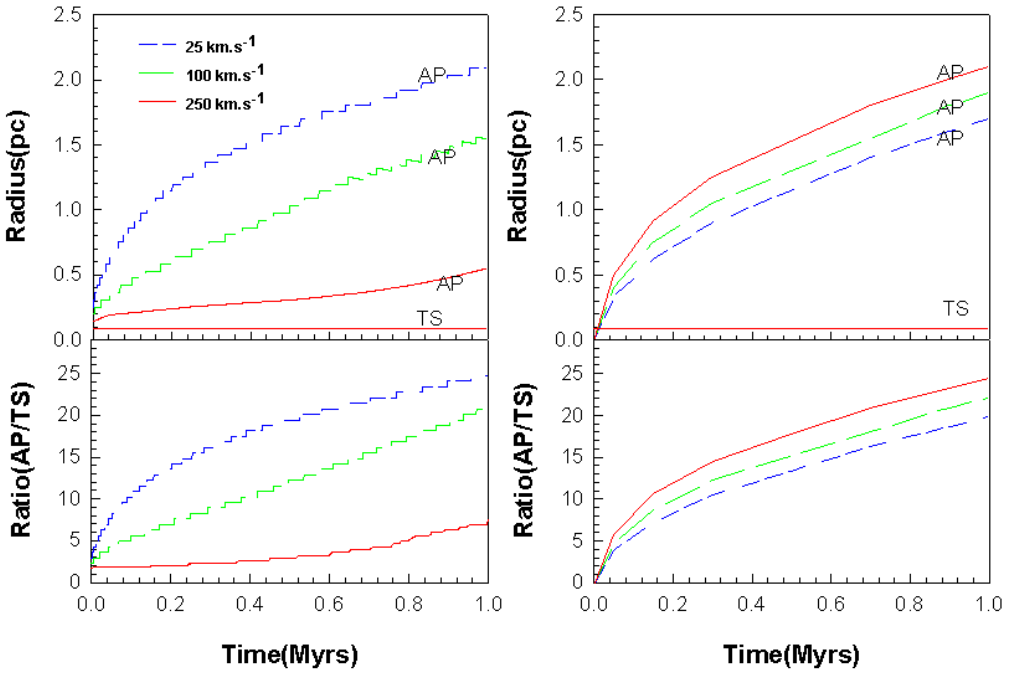

Figure 5.9: Same as Figure 5.4, except a mass-loss rate of $10^{-5} M_{\odot}$ yr^{-1} and ρ_{ISM} = 10^{-21} g cm^{-3}.

s^{-1} as shown by Figure 5.8 and row 1 from Figure 5.3. As the mass-loss rate is decreased and the ISM density is increased, the time profiles expand slower with the slowest and smallest cavity corresponding to where the mass-loss rate is 5 $\times$ 10^{-6} $M_{\odot}$ y^{-1} and the ISM density is

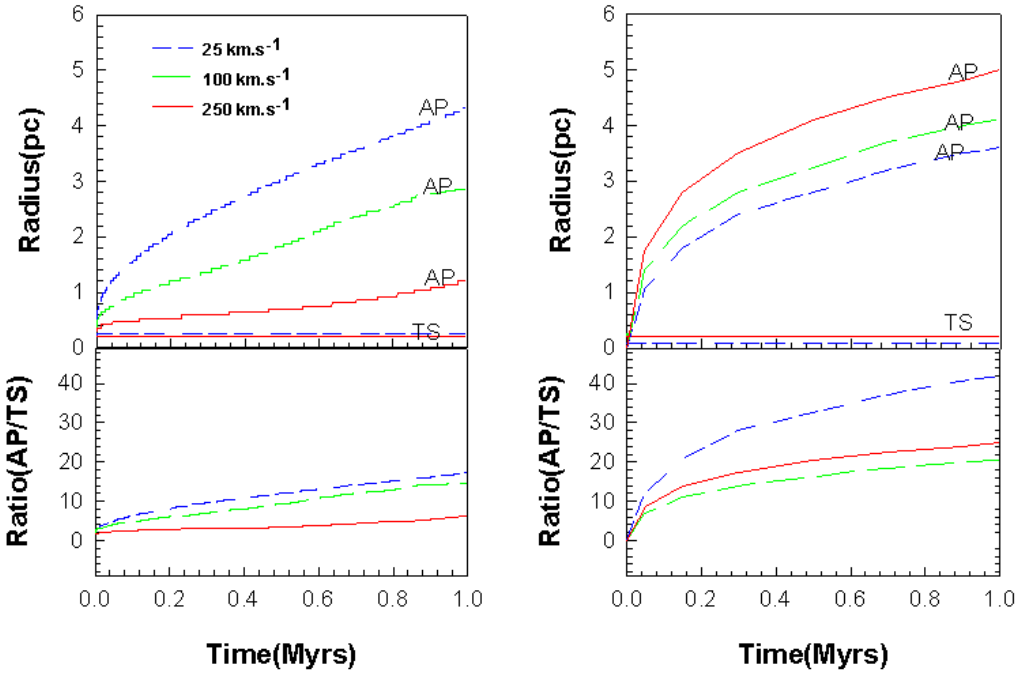

Figure 5.10: Same as Figure 5.4, except with a mass-loss rate of $5 \times 10^{-6} M_{\odot}$ yr^{-1} and $\rho_{ISM} = 10^{-22}$ g cm^{-3}.

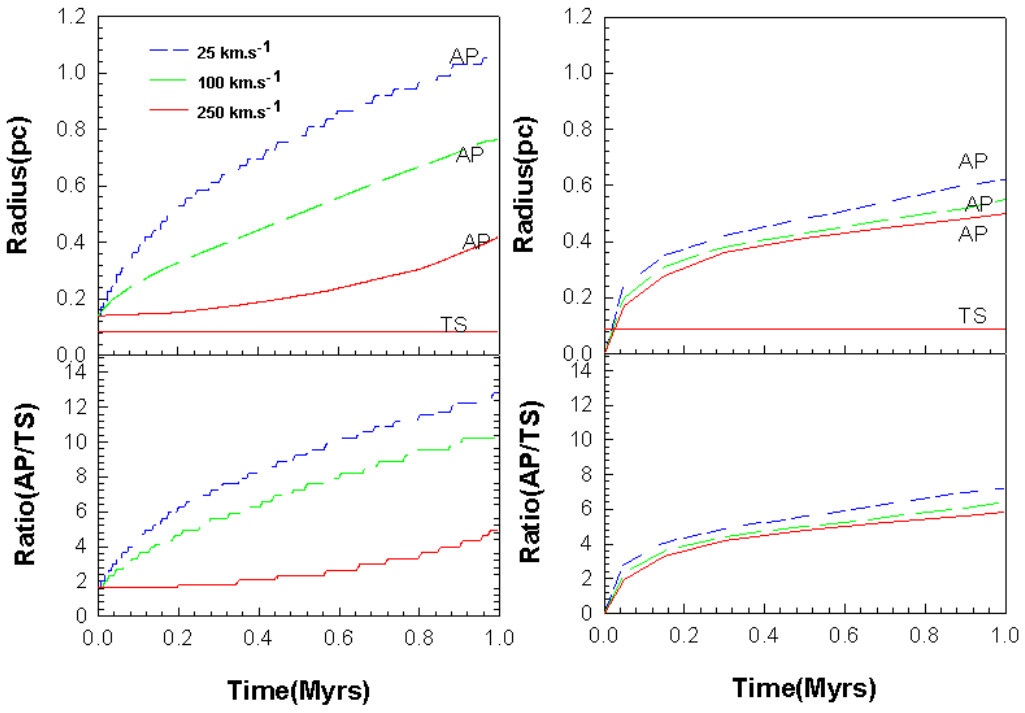

Figure 5.11: Same as Figure 5.4, except with a mass-loss rate of $5 \times 10^{-6} M_{\odot}$ yr^{-1} and $\rho_{ISM} = 10^{-21}$ g cm^{-3}.

10^{-21} g cm^{-3}, as shown by Figure 5.11 and row 4 from Figure 5.3.

As done for the previous section, the quantitative analysis can be done for the different AP radii in the nose direction due to different relative speeds. For the scenario of a relative speed of 25 km s^{-1}, the result is that the AP radius for a stellar wind with a relative speed of 25 km s^{-1} forms at a distance that is a factor ~ 0.9 the AP radius for the case for no relative speed in the nose direction. This applies for models 1, 4, 7 and 10 from Table 5.2. For the case of a relative speed of 100 km s^{-1}, the AP radius is a factor of ~ 0.7 the AP radius with no relative speed (see models 2, 5, 8 and 11 in Table 5.2) in the model. For the case of a relative speed of 250 km s^{-1} the AP radius is a factor of ~ 0.25 compared to the AP radius for no relative speed assumed in the models (see models 3, 6, 9 and 12 in Table 5.2). This again indicates that this parameter is important in stellar wind evolution.

5.4 Summary and conclusions

In this chapter, the main focus was to establish to what extent the relative motion between the stellar wind and ISM has an effect on the structure of the cavity blown by its stellar wind. Again both the cases of evolution into the ambient medium and into a molecular cloud were considered. The results show that as the relative speed is increased, the stellar wind cavity (AP radius) becomes smaller in the nose direction and larger in the tail direction. The nose direction is defined as the direction opposite to the flow of the ISM material and the tail along the flow of the ISM material.

For a relatively low relative speed of 25 km s^{-1}, the ratio of the AP between the nose and the tail is ~ 1.4 for all the scenarios considered. For an assumed relative speed of 100 km s^{-1} in the model, the ratio of the AP between the nose and tail is between 1.6 and 2.0, while for an assumed relative speed of 250 km s^{-1}, the ratio of the AP between the nose and tail is between 4.0 and 5.0, depending on parameters like ISM density and mass-loss rate. Again, AP and TS radii were compared by varying different parameters like ISM density, outflow speeds and mass-loss rate. These will not be summarized here.

From Figures 5.4 to 5.7 and Figure 5.8 to Figure 5.11 it can be summarized that for all mass-loss rates and ρ_{ISM} values the following is applicable. The AP radius in the nose direction for a stellar wind with a relative speed of 25 km s^{-1} is a factor of ~ 0.9 compared to the AP radius of a stellar wind with no relative speed. For a stellar wind with a relative speed of 100 km s^{-1}, the factor is ~ 0.7 compared to a stellar wind with no relative speed, and lastly the AP radius of a stellar wind with a relative speed of 250 km s^{-1} is a factor of ~ 0.25 compared to the AP radius of a stellar wind with no relative speed.

Chapter 6

Supernova remnant evolution in stellar wind bubbles

6.1 Introduction

A supernova explosion of a massive star will result in an expanding supernova remnant (SNR) with speed v typically in the range 10^8 to 10^9 cm s^{-1}, depending on the ejection energy E_{ej} and ejecta mass M_{ej} of the original star. The expansion of an SNR is decelerated due to mass-loading by the swept-up interstellar medium (ISM). During the initial stages, the ejecta mass is larger than the swept-up mass and the SNR is in the free expansion phase. See *Woltjer* (1972) for a description of the different stages of SNR evolution. When the swept-up mass becomes sufficiently larger than the ejecta mass $\sim$ (1.61 times larger *McKee and Truelove*, 1995), the SNR is in the Sedov (*Sedov*, 1959) phase. During this phase, a reverse shock (RS) will form because of the low pressure of the ejected material that has been adiabatically expanding. The RS will then be driven back into the interior of the SNR (e.g. *Ardavan*, 1973; *McKee*, 1974), and in the process will heat the material interior of shell. The remnant is still bounded by a strong blast wave, called the forward shock (FS).

Ferreira and de Jager (2008) studied SNR evolution in both a uniform and a non-uniform ISM background. They showed how different parameters, such as E_{ej}, M_{ej}, ISM density ρ_{ISM} (See also e.g. *Dwarkadas and Chevalier*, 1998; *Truelove and McKee*, 1999; *Tang and Wang*, 2005) and the adiabatic index γ (e.g. *Decourchelle et al.*, 2000; *Ellison et al.*, 2004) influence the evolution of an SNR in a uniform medium. They derived an analytical expression giving the return time t_R of the RS to the origin in terms of these parameters. In that study, they used a hydrodynamic model similar to the model used in this work. They also included a kinematic calculation (solving the induction equation) of the interstellar magnetic field (*LeVeque*, 2002; *Fahr et al.*, 2000; *Scherer and Ferreira*, 2005; *Ferreira and Scherer*, 2006).

In the work of *Ferreira and de Jager* (2008), the existence of a pulsar wind nebulae (PWN) inside an SNR was neglected. As shown by *van der Swaluw et al.* (2001); *Blondin et al.* (2001); *Bucciantini et al.* (2003) and *Del Zanna et al.* (2004), this relativistic wind may alter t_R making the calcula-

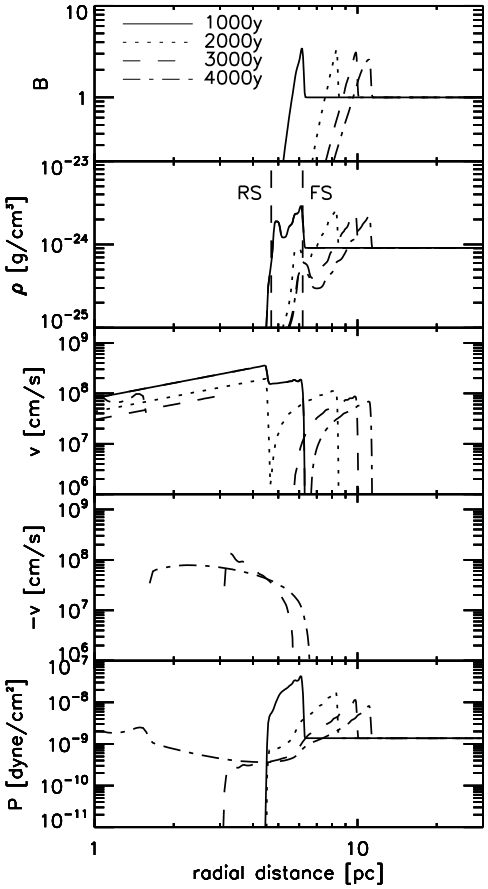

Figure 6.1: The evolution of a typical SNR in the undisturbed ISM computed using parameters as described in the text. Results are shown from 1000 to 4000 years as indicated. Shown in the top panel is the ISM magnetic field B (perpendicular to the flow), which is compressed by a factor $s \approx 4$. Shown in the second panel is the density ρ. From the origin one can see the reverse shock (RS), the contact discontinuity between the ejected and shocked ISM and the blast wave, and the forward shock (FS), which propagates into the undisturbed ISM. The positions of the RS and FS are indicated by the vertical dashed lines. In the bottom panels the speed v is shown on a logarithmic scale, and therefore $-v$ is shown just below it. Shown here is that at some time the RS starts to move inward, and the speed reverses sign meaning that the flow is now inwards toward the center. In the last panel, the pressure P is shown. Note that in these calculations no initial stellar wind was assumed. From *Ferreira and de Jager* (2008).

tions of *Ferreira and de Jager* (2008) only valid for SNR without any PWN or with a PWN having a relatively small luminosity. Also not included in their calculations was the contribution from a late phase stellar wind. As will be shown in this chapter, depending on different model parameters, such a wind is important. The effect of such a circumstellar wind and how this may modify conditions in the ambient medium and subsequently the simulations describing the evolution of an SNR is the topic of this chapter.

6.2 Model and parameters

The model is already described in Chapter **3**. For the initial and boundary conditions of the SNR (See also *Blondin and Ellison*, 2001; *van der Swaluw et al.*, 2001; *Bucciantini et al.*, 2003; *Del*

Zanna et al., 2004), a spherical region is assumed with radius r_{ej} and a high constant density ρ_{ej} with a radially increasing velocity profile

$$v = \frac{r}{t} = v_{ej} r / r_{ej}. \tag{6.1}$$

In this work it is assumed that $r_{ej} = 0.1$ pc while the density is

$$\rho_{ej} = \frac{3 M_{ej}}{4 \pi r_{ej}^3}, \tag{6.2}$$

with M_{ej} the ejecta mass. For the velocity

$$v_{ej} = \sqrt{\frac{10}{3} \frac{E_{ej}}{M_{ej}}}. \tag{6.3}$$

Figure 6.1 (from *Ferreira and de Jager*, 2008) shows a typical example of an SNR evolving in the undisturbed ISM at different stages of evolution computed using $E_{ej} = 10^{51}$ erg, $M_{ej} = 3 M_\odot = 6 \times 10^{33}$ g, and for the background ISM $\rho_{ISM} = 10^{-24}$ g cm^{-3} (See also *van der Swaluw et al.*, 2001). Shown in the top panel is the ISM magnetic field B (assumed to be perpendicular to the flow), which is compressed by the FS by a factor s. From the Rankine-Hugoniot conditions one can show that for non-relativistic speeds it follows that γ= 5/3 and $s \approx 4$, which is the factor shown in Figure 6.1.

Note that to compute the compressed ISM magnetic field, the induction equation

$$\frac{\partial \mathbf{B}}{\partial t} + \nabla \times (\mathbf{v} \times \mathbf{B}) = 0 \tag{6.4}$$

was solved using a similar scheme as for the fluid part. Note that this is not a full magneto-hydrodynamic (MHD) solution because the field is calculated kinematically from the flow (*Scherer and Ferreira*, 2005; *Ferreira and Scherer*, 2006) and no backreaction on the fluid is considered. The only field that is computed is the field of the ISM, which is compressed as the ISM is swept-up by the forward shock of the SNR.

Shown in the second panel from the top is the density ρ. From the origin one can see the RS, the contact discontinuity between the ejected and shocked ISM and the FS propagating in the undisturbed ISM. Shown here is that for these parameters the swept-up material is comparable to the ejected mass after around 1000 years. As time increases, the swept-up mass becomes considerably larger than the ejecta mass and the SNR enters the Sedov phase where the FS radius now scales as $t^{2/5}$. Note that, depending on parameters, the transition between these phases may be just as long as the phase itself (See e.g. *Cioffi et al.*, 1988; *Dohm-Palmer and Jones*, 1996).

In the bottom three panels the speed v and pressure P are shown. Note that because v is shown on a logarithmic scale, $-v$ is also shown. This is important to show when the flow changes direction and points inward. Shown in these three panels is that at some time the RS starts to move inward because of the low pressure of the ejected material, which has been

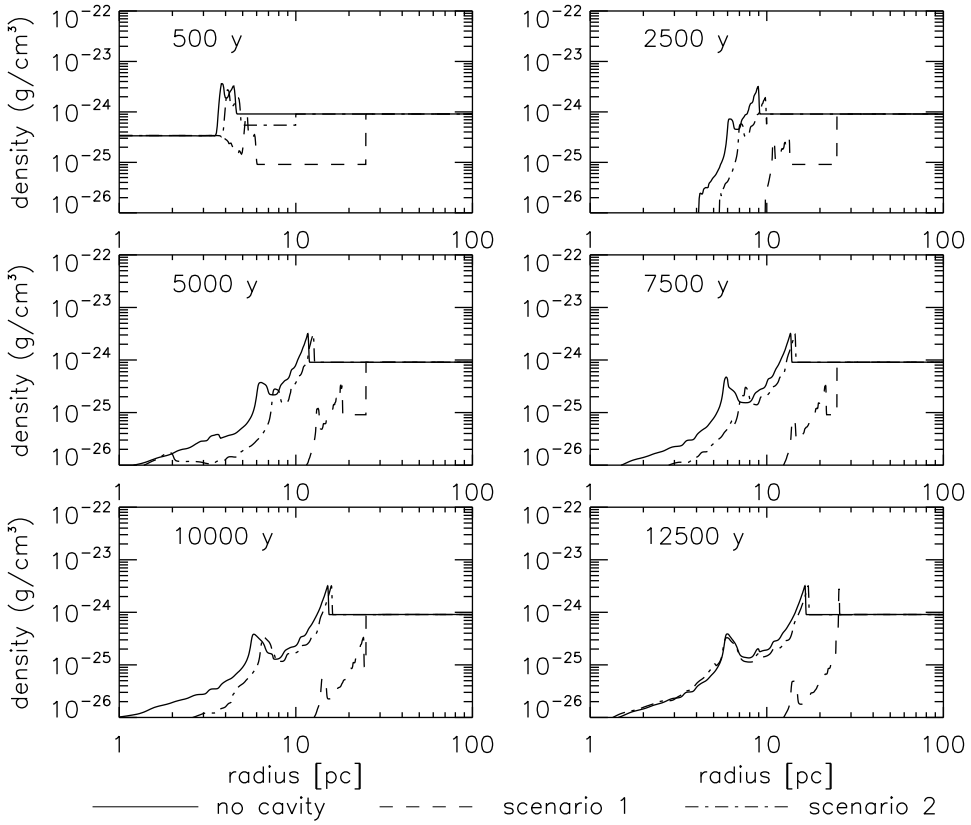

Figure 6.2: Density profiles ρ are shown for the different computed scenarios. The solid line corresponds to the case when the effect of a stellar wind is neglected and no initial cavity is present. This is called the no cavity scenario and the SNR will evolve into undisturbed ISM. Scenario 1, shown by the dashed line, corresponds to an SNR evolving into a cavity blown out by a stellar wind corresponding to a star with mass-loss rate of 10^{-5} $M_\odot$ y^{-1} and outflow speed of 2000 km s^{-1}. This results in a cavity of a radius of $\sim$ 25 pc after 1 My and a factor of $\sim$ 10 difference in density between the ISM and the post-shocked material. Scenario 2, shown by the dashed-dotted line, the mass-loss rate of the original star is 10^{-5} $M_\odot$ y^{-1} and outflow speed of 1000 km s^{-1}. The stellar wind cavity for this scenario has a radius of $\sim$ 10 pc and the difference in density between the undisturbed ISM and the post-shocked density is $\sim$ 1.66. For both scenarios the undisturbed ISM density is 10^{-24} g cm^{-3}. The different panels correspond to different points in time after the supernova explosion.

adiabatically expanding. At this stage, the speed reverses sign meaning that the flow is now towards the center. As shown for 4000 years, the RS has reached the origin and visible in the bottom panel is that when the RS propagates into the ejecta, the latter is heated.

6.3 SNR evolution in a uniform medium

As mentioned above, *Ferreira and de Jager* (2008) investigated the time for the RS to return to the origin t_R. Note that although the rotational energy released by a pulsar (which may be found inside an SNR) is much smaller compared to the mechanical energy released in the SNR, the possible existence of a relativistic wind from a pulsar wind nebula (PWN) inside an SNR may alter the return time of the RS to the origin (*van der Swaluw et al.*, 2001; *Blondin et al.*, 2001; *Bucciantini et al.*, 2003; *Del Zanna et al.*, 2004). Initially, the pressure in the pulsar bubble is

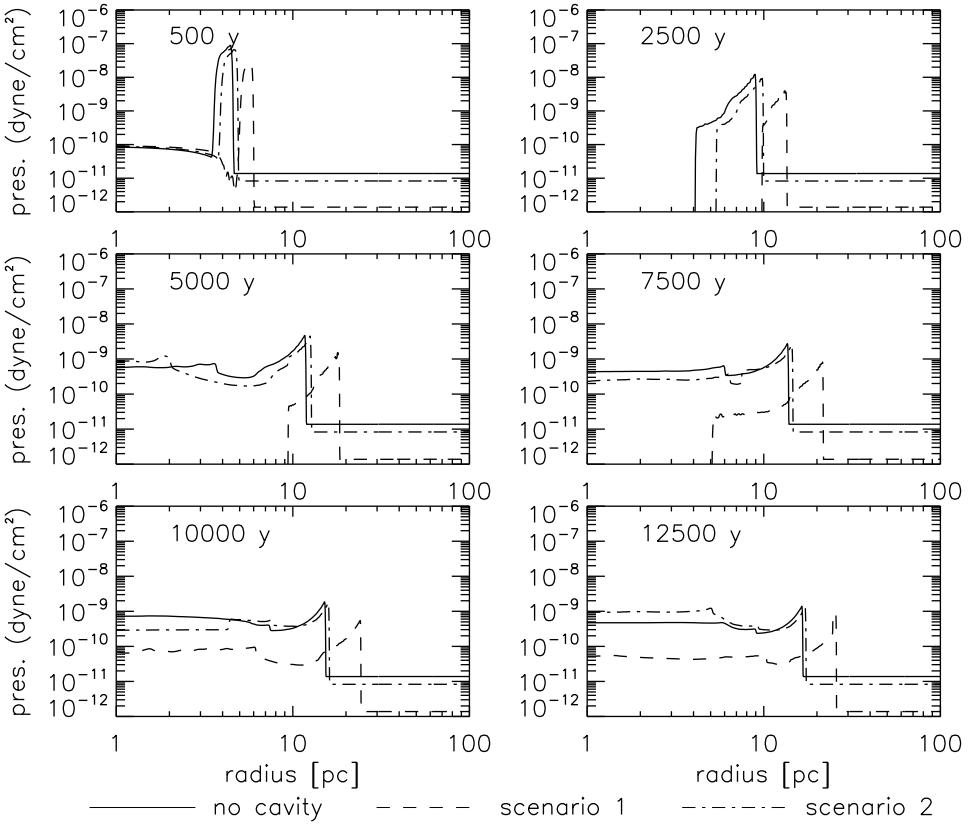

Figure 6.3: Similar to Figure 6.2, except here the pressure profiles are shown.

negligible compared to the SNR and the PWN has no effect on the dynamics of the infalling reverse shock (e.g. *Blondin et al.*, 2001). However, as the pulsar bubble is compressed, the pressure rises and at some stage becomes comparable to the pressure behind the RS leading to an unstable phase. In the work of *Ferreira and de Jager* (2008), they neglect the effect of such a PWN making their expression of t_R valid for SNRs with no PWN inside, or where the luminosity of the PWN is relatively small.

These authors found, as expected, that the FS radius is largely dependent on the ISM density. Larger densities, e.g. $\rho_{ISM} = 10^{-23}$ g cm^{-3}, lead to a much smaller blast wave radius compared to lesser densities, e.g. $\rho_{ISM} = 10^{-27}$ g cm^{-3} for the same simulation time. The ejecta mass M_{ej} does not play a significant role in determining the FS radius, especially for the times shown towards the end of the simulation. This is because after a few hundred years the mass of the swept-up material is comparable with or higher than the ejecta mass. This is not the case for the first few hundred years where this quantity will result in a different initial speed (via Equation 6.3) and may influence the transition time from a free expansion to the adiabatic phase.

Concerning the RS radius, *Ferreira and de Jager* (2008) showed that the time for it to return to the origin is very much dependent on both ρ_{ISM} and M_{ej}. For a larger ρ_{ISM} the SNR evolves sooner into the Sedov phase. This is also the case for a smaller M_{ej}, which will lead to a smaller pressure of the ejecta material. The density of the ISM is an important parameter determining the RS radius and return time because this parameter may vary by many orders of magnitude.

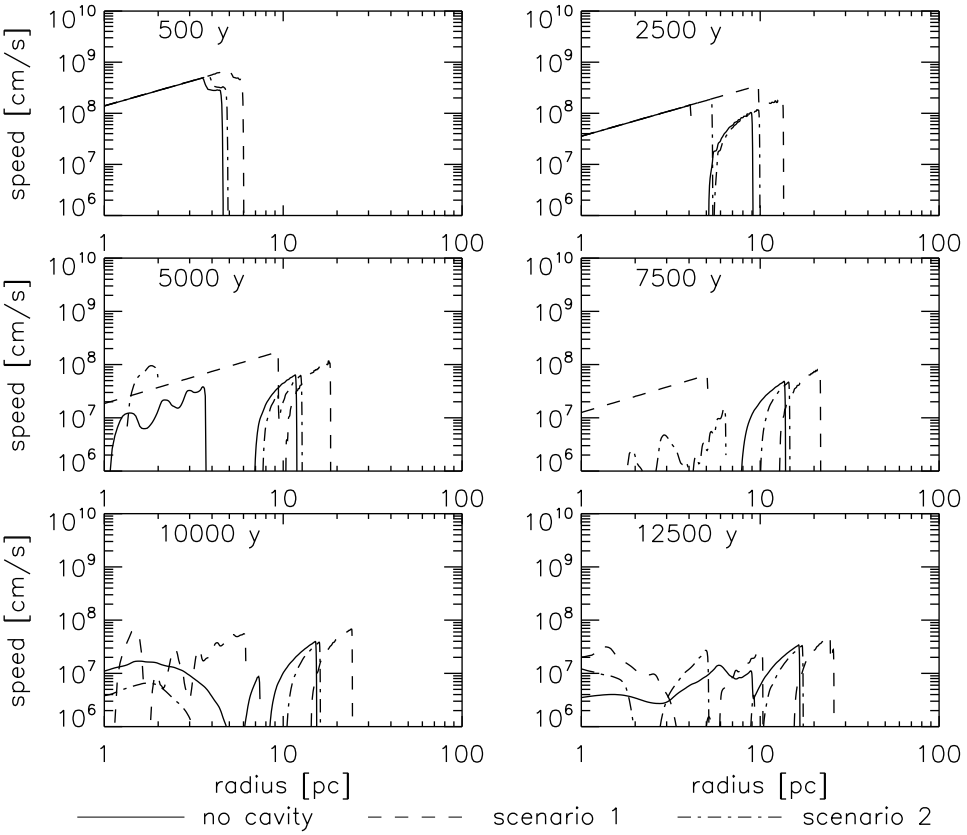

Figure 6.4: Similar to Figure 6.2, except here the velocity profiles are shown.

By varying different parameters, e.g. M_{ej} =1, 2, 3, 5, 7 and 10 $M_{\odot}$ and ρ_{ISM} ranging from 10^{-21} g cm^{-3} to 10^{-27} g cm^{-3}, *Ferreira and de Jager* (2008) found $t_R \propto \rho_{ISM}^{-1/3}$, similar to the results from *Truelove and McKee* (1999) and $t_R \propto M_{ej}^{3/4}$ for all ρ_{ISM} scenarios. Concerning the ejecta mass, they found that when the return time t_R of the RS is calculated, $t_R \propto E_{ej}^{-45/100}$. Note that this dependence on mass and energy is slightly different from the similarity scaling of *Truelove and McKee* (1999), which yielded -0.833 and -0.5 respectively. This might be due to the assumed pressure of the ISM, where *Truelove and McKee* (1999) assumed $P = 0$, while *Ferreira and de Jager* (2008) assumed for the ISM temperature to be 1000 K (See also e.g. *Tang and Wang*, 2005).

Lastly, *Ferreira and de Jager* (2008) also reported on an additional parameter that may influence the shock structure in particular, and that is the adiabatic index γ. The latter may change due to the non-linear interaction of accelerated cosmic rays on SNR shocks (e.g. *Decourchelle et al.*, 2000; *Ellison et al.*, 2004). As these relativistic particles are produced they contribute to the pressure resulting in the shocked plasma becoming more compressible ($\gamma \rightarrow 4/3$). They found $t_R \propto \gamma^{-3/2}$.

Therefore, concluding from *Ferreira and de Jager* (2008),

$$t_R = 4000 \left(\frac{\rho_{ISM}}{\rho_0}\right)^{-1/3} \left(\frac{M_{ej}}{M_0}\right)^{3/4} \left(\frac{E_{ej}}{E_0}\right)^{-45/100} \left(\frac{\gamma}{\gamma_0}\right)^{-3/2} y \tag{6.5}$$

In this equation $\rho_0 = 10^{-24}$ g cm^{-3}, $M_0 = 3M_{\odot}$, $E_0 = 10^{51}$ erg and $\gamma_0 = 5/3$. Assuming these

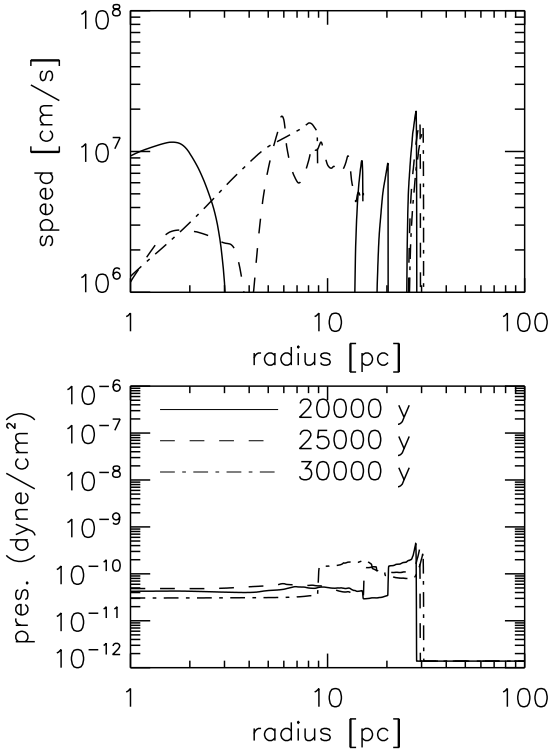

Figure 6.5: This figure focuses on the evolution of the computed system corresponding to scenario 1 in the previous figures. Results are shown as velocity profiles at the top and pressure profiles in the bottom. Computations correspond to different simulation times, e.g. 20000 y which is shown as the solid line, 25000 y shown as the dashed line and 30000 y shown as the dashed-dotted line.

values result in $t_R = 4000$ years.

Next, this work follows on the initial study of *Ferreira and de Jager* (2008) where it will be shown how the presence of an initial stellar wind cavity influences the dynamics of the SNR evolution, e.g. the FS and RS radius and the return time of the RS, therefore limiting the application of Equation 6.5.

6.4 SNR evolution in a cavity

In Chapters **4** and **5**, calculations of stellar wind evolution were presented corresponding to different parameters. It was shown how the stellar wind blows out a cavity in the undisturbed ISM with different astropause (AP) distances depending on these parameters. In this chapter, the effects of such a cavity (astrosphere), blown out by the stellar wind of the original star, on the evolution of supernova remnants are investigated. For this purpose different scenarios, corresponding to different models in Chapter **4**, are selected. Only solutions up to 1 My are considered. Note that throughout this chapter results are also presented when no cavity is assumed as an initial condition in the model. This scenario can be directly compared to the calculations of *Ferreira and de Jager* (2008) who presented SNR simulations in the undisturbed ISM only.

For the first scenario (Scenario 1), a cavity is assumed as an initial condition corresponding to panel (b) in Figure 4.2 where the boundary of the cavity, AP radius, is situated at ~ 25 pc and the difference between the undisturbed ISM density and the post-shocked material is ~ 10. The second scenario (Scenario 2) corresponds to panel (a) in the same figure with a stellar wind boundary of ~ 10 pc and difference in density between the undisturbed ISM and post-shocked flow of a factor of ~ 1.66. These scenarios correspond to stars with stellar winds with a mass-loss rate of 10^{-5} $M_\odot$ yr^{-1} and outflow speeds of 2000 km s^{-1} and 1000 km s^{-1} respectively and after 1 My. For these scenarios, the ISM density is assumed to be 10^{-24} g cm^{-3}. Other scenarios will be presented later. Furthermore, $M_{ej} = 3\ M_\odot$ for the first results of this chapter. This ejecta mass is well below the value typical of stars of interest in this work, but other scenarios where this parameter was increased, are presented later. This particular value is selected to present results comparable to those of *Ferreira and de Jager* (2008).

In Figure 6.2, the density ρ is shown for the two scenarios discussed above (Scenario 1 is shown by the dashed line while Scenario 2 is shown by the dashed-dotted line) and a third scenario is also shown, which corresponds to SNR evolution in the undisturbed ISM. The solid line corresponds to this case where the effect of a stellar wind is neglected and no initial cavity is present. The different panels correspond to different times after the supernova explosion.

First, we start in the top left panel corresponding to 500 years after the initial explosion. From the origin one can see the RS and the outer blast wave, FS, as large jumps in the density profile. Especially evident here, after such a short simulation time, is the difference between the different scenarios due to different initial conditions. For the solid line, the no cavity scenario, the SNR evolves into an undisturbed ISM. This is similar to calculations done by *Ferreira and de Jager* (2008). Comparing the two scenarios, which include the effects of a stellar wind cavity it follows that Scenario 1 has a much higher initial stellar wind speed and therefore a larger cavity. As shown, the SNR corresponding to this scenario will evolve into a much less dense medium up to 25 pc. For scenario 2, the stellar wind speed is smaller leading to a smaller AP radius and density jump. Therefore, already evident here after 500 y for Scenario 1, the outer blast wave is already considerably further ahead compared to the other two scenarios.

Note that for these two scenarios (and all shown later in this chapter), the density within the cavity blown out by the stellar wind decreases as $1/r^2$ up to a shock. See e.g. Figure 4.2 in Chapter **4**. After the shock, the density should increase as the compression ratio and become incompressible due to subsonic nature (a one-fluid scenario is assumed) resulting in the density being constant as a function of increasing distance up to the boundary (AP) where there is a jump again to the value of the undisturbed ISM. For simplicity, no relative motion of the initial star as in Chapter **5** is assumed and therefore no bow-shocks are expected in the undisturbed ISM. From Chapter **4** it follows that most of the computed stellar wind scenarios result in a termination shock distance smaller than ~ 1 pc, and therefore not visible in the figures shown in this chapter.

It follows from Figure 6.2 that as time progresses to 2500 y and beyond, the FS of Scenario

1 is moving further ahead compared to the other two scenarios because it is still within the cavity blown out by its original stellar wind and hence evolves in a much less dense region. For Scenario 2, the effects are not as pronounced (when compared to the solid line) due to its much smaller cavity and smaller density difference between the post-shocked density and the undisturbed ISM density. However, a difference in the FS blast wave radius compared to the case where the SNR evolves in undisturbed ISM is also evident for this scenario. Evident in the bottom two panels is that for Scenario 1, the FS reaches the boundary of its cavity at approximately ~ 10000 y and then progresses into the undisturbed medium. It will be shown later that the interaction of the FS with the discontinuity between the two different media influences the speed in which this blast wave propagates. Next, we will concentrate on the pressure profiles that contain more details concerning the RS of the SNR for the different scenarios.

Figure 6.3 shows results similar to Figure 6.2, except here the pressure profiles are shown. These profiles are especially important to capture the location and dynamics of the reverse shock (RS). In the first two panels (500 y and 2500 y), the location of the FS and RS is clearly visible as large jumps in pressure. At 5000 y both the solid line, corresponding to the SNR evolution in the undisturbed ISM and the dashed-dotted line, corresponding to Scenario 2 with an initial stellar wind of mass-loss rate 10^{-5} $M_{\odot}$ yr^{-1} show only one significant discontinuity in the pressure profile. This is because the RS already returned to the origin for these. However, for Scenario 1, the RS is still visible due to the evolution of the system in a much less dense medium, e.g. a factor of 10. From Equation 6.5 it follows that for this scenario the RS will return to the origin at ~ 8500 y. This is also evident in this figure where for panel 7500 y the RS is still visible for this scenario, but for panel 10000 y not. Therefore, an initial conclusion can be made that the inclusion of a cavity, blown out by the stellar wind, is important to include as an initial condition in simulations when SNR evolution is calculated. This is especially true if the initial cavity is in the order of a few pc.

Figure 6.4 shows results similar to Figures 6.2 and 6.3, except here the velocity profiles are shown. Note that values are shown on a logarithmic scale and gaps therefore indicate negative velocities (meaning flow back toward the center). Starting with the first panel it is evident that, as is already mentioned above, the FS of Scenario 1 propagates with a larger speed compared to the other two scenarios because of the smaller density. From the panels 2500 y and 5000 y, one can see that the speed becomes negative for Scenario 2 as well as for the scenario where no cavity is assumed. This marks the return of the RS to the origin for these two scenarios. After this, the velocity profiles become increasingly disordered due to different waves moving back and forth after the return of the RS to the origin. It is interesting that for Scenario 1 a second peak starts to emerge in the velocity profile around ~ 25 pc at 12500 y. This is after the FS reached the interface between the stellar wind material and the undisturbed ISM. This will be discussed next.

Figure 6.5 focuses on the evolution of the system corresponding to Scenario 1. Results are shown as velocity profiles at the top and pressure profiles in the bottom. Computations cor-

respond to different simulation times, e.g. 20000 y shown as the solid line, 25000 y shown as the dashed line and 30000 y shown as the dashed-dotted line. Interestingly here as the FS hits the discontinuity between the stellar wind and undisturbed ISM around $\sim$ 10000 y and then proceeds to move into the undisturbed ISM, the velocity of the FS decreases. This is shown by the difference in the far-right peaks in the top panel, corresponding to 20000 y, 25000 y and 30000 y respectively. This feature is expected due to momentum conservation. However, more interesting is a reflection wave/shock that originates in the process. From the pressure profiles, shown in the bottom panel, this shock travels back inward towards the origin. This is also evident in the velocity profiles where the speed becomes negative and therefore disappears from the top panel because of the logarithmic scale used. Such a reflection wave/shock can have an influence on e.g. pulsar wind evolution if such a relativistic wind was assumed in these calculations. However, this is beyond the scope of this study. As will be shown later, this interaction also removes energy from the FS and in the process will decelerate the speed of the outblowing blast wave and will influence its evolution with time. This is an aspect illustrated next.

Figure 6.6 shows the evolution of the FS and RS radii as a function of time for the different scenarios discussed above. Shown in the top panels are the FS radius (top lines) and RS radius (bottom lines) for the three scenarios discussed above. The solid line corresponds to the evolution of an SNR in undisturbed ISM, i.e. no cavity. The dashed line corresponds to the evolution of an SNR within a cavity blown out by a stellar wind with mass-loss rate of 10^{-5} M$_{\odot}$ yr^{-1} and outflow speed of 2000 km s^{-1} and the dashed-dotted line to a stellar wind with mass-loss rate of 10^{-5} M$_{\odot}$ yr^{-1} and outflow speed of 1000 km s^{-1}. The top left panels show results corresponding to an ejecta mass M_{ej} = 3 $M_{\odot}$ (used for all calculations above to correspond with the calculations from *Ferreira and de Jager*, 2008), while the right panels correspond to M_{ej} = 8 $M_{\odot}$. The bottom panels show the ratio of different FS radii between the two scenarios with a stellar wind present and the case with no stellar wind present.

First, we concentrate on the RS radii shown as the bottom lines in the top two panels of Figure 6.6. As can be seen these increase due to the RS moving outward and then returning to the origin. As shown by *Ferreira and de Jager* (2008), the RS spends roughly half of its time moving outward and the rest returning towards the origin. Shown in Figure 6.6 is that there are significant differences between the different scenarios shown in this figure. For the two scenarios corresponding to the SNR evolving into a cavity, the return of the RS, t_R, to the origin occurs at a much later stage. This is in accordance with the results of *Ferreira and de Jager* (2008), who suggest a later return time for a decrease in the density in which the SNR evolves in. From their calculations it follows that $t_R \propto (\frac{\rho}{\rho_0})^{-1/3}$ where ρ is the medium in which the SNR propagates and $\rho_0 = 10^{-24}$ g cm^{-3}. Therefore, for Scenario 1, the RS does not return at $\sim$ 4000 y, as would be the case if the SNR evolves into undisturbed ISM of 10^{-24} g cm^{-3}, but rather at $\sim$ 8500 y. For Scenario 2, the difference in return time, compared to the solid line, is less with the RS returning after $\sim$ 5000 y. Although for this scenario the cavity is much smaller compared

to Scenario 1, therefore the assumption of such a cavity as an initial condition in the model is important.

The FS is shown by the increasing lines at the top panel. Shown here is that a cavity resulting from a stellar wind also influences the evolution of this blast wave. The difference between Scenario 1, shown by the dashed line, and the case for no cavity, shown by the solid line, first increases because of the faster blast wave of Scenario 1, but then decreases again. For Scenario 2, smaller differences between its FS radius, shown as the dashed-dotted line, and the solid line exist. This is more quantitatively shown by the bottom panels in Figure 6.6. Shown here is the ratio between the dashed line (scenario 1) and the solid line (no cavity) and is shown as a dashed line. The same follows for scenario 2 with the ratio shown as a dashed-dotted line. Shown here is that for Scenario 1 the ratio increases up to $\sim$ 10000 y until the FS reached the boundary of the cavity. Thereafter, the ratio significantly decreases as the FS moves into a more dense medium. Because the ratio converges to unity, it is an indication that in this process energy was removed (in terms of a reflection wave/shock as discussed above) and the speed suddenly decreases. For Scenario 2 the effect is similar, but not as pronounced. Therefore, the conclusion is that the results of *Ferreira and de Jager* (2008) are still valid if the initial cavity of the stellar wind is relatively small. This must be in the order of 1pc and less because even Scenario 2 shows that, although the FS is not really affected by the presence of such a cavity, the RS will return later e.g. 5000 y compared to 4000 y, a factor of 1.25 for a cavity of 10 pc and a density difference between the post-shocked and undisturbed ISM density of 1.66. This effect will decrease considerably if the initial cavity is smaller.

The right panels in Figure 6.6 show similar results, except here the ejecta mass was increased to M_{ej} = 8 $M_{\odot}$ to be more comparable to the type of stellar winds simulated in the previous chapters. Later on in this chapter this will be even further increased to M_{ej} = 12 $M_{\odot}$. Shown here are very similar results compared to the left panels giving an indication that, at least for the parameters assumed to compute the results in Figure 6.6, varying the ejecta mass does not really change any of the conclusions made above.

Figure 6.7 shows similar results to Figure 6.6, except results are shown corresponding to other stellar wind mass-loss rates and more dense ISM conditions. For the left panels, the stellar wind with a mass-loss rate of 5×10^{-5} M$_{\odot}$ yr^{-1} and outflow speeds of 3000 km s^{-1} and 2000 km s^{-1} are selected corresponding to panels (g) and (h) in Figure 4.2 respectively. For both these scenarios, a cavity is blown in an ISM with density 10^{-23}g cm^{-3}, some 10 times higher as in Figure 6.6. Scenario 1 corresponds again to the larger cavity, this time $\sim$ 18 pc, while Scenario 2 corresponds to a cavity of $\sim$ 10 pc. Both these scenarios have a factor of $\sim$ 10 difference between the ISM and the post-shocked medium. For the right panels, the ISM density was even further increased to 10^{-22}g cm^{-3}. This was done for the assumption that the star was still embedded in a molecular cloud at the time the supernova explosion occurred. For the right panels, Scenario 1 corresponds to a cavity of 6 pc and with a density difference between the post-shocked medium and the undisturbed ISM of a factor of 3, while for scenario 2 the

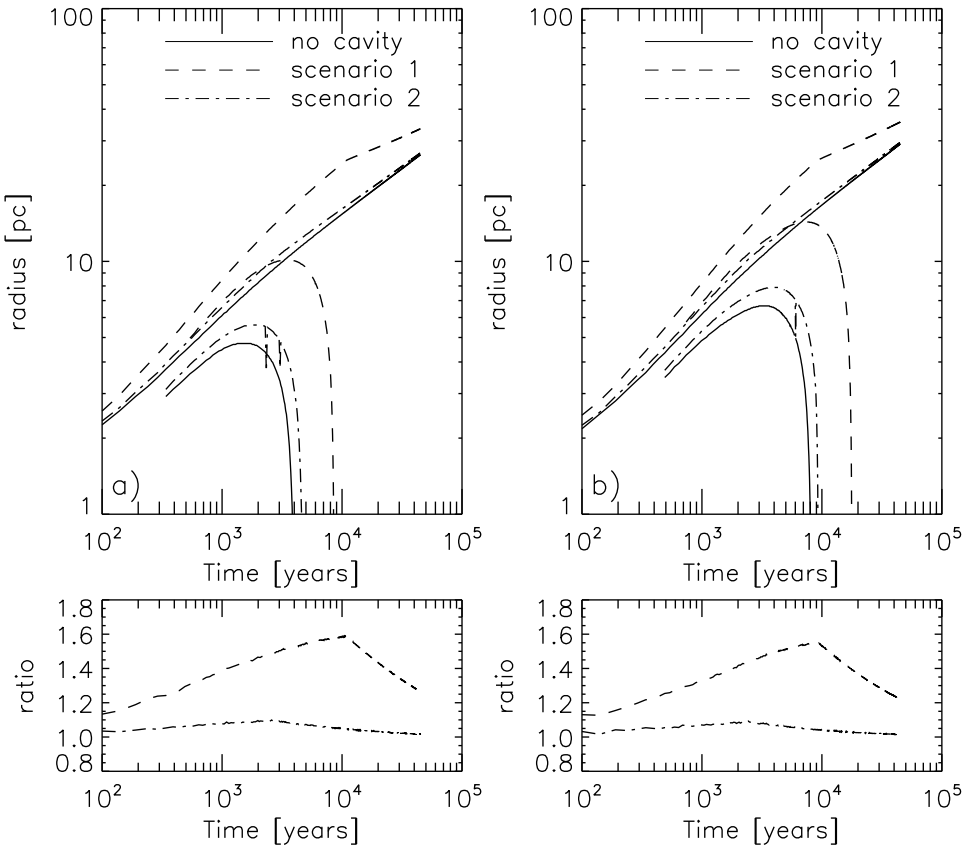

Figure 6.6: The evolution of the FS and RS as a function of time for different computed scenarios. Shown in the top panels are the FS (top lines) and RS (bottom lines). The solid lines correspond to the evolution of an SNR, FS and RS in undisturbed ISM, e.g. no cavity. The dashed lines correspond to the evolution of these shocks within a cavity blown out by a stellar wind with mass-loss rate of 10^{-5} $M_\odot$ y^{-1} and outflow speed of 3000 km s^{-1} and the dashed-dotted lines correspond to a stellar wind with mass-loss rate of 10^{-5} $M_\odot$ y^{-1} and outflow speed of 2000 km s^{-1}. The left shows results corresponding to an ejecta mass M_{ej} = 3 $M_\odot$, while the right panels correspond to M_{ej} = 8 $M_\odot$. The bottom panels show the ratio of the different radii FS where there is a stellar wind present and the case with no stellar wind, e.g. the dashed line would be the ratio of the FS of Scenario 1 in the top left panel (dashed line) and the solid line (e.g. no cavity present).

difference is a factor of 2 and the cavity size is 4 pc.

The conclusion from Figure 6.7, as for Figure 6.6, is that the FS is not considerably influenced by the presence of a cavity if this cavity is $\sim$ 10 pc or smaller. However, the RS is strongly influenced, even for the right panels where the cavities are much smaller compared to the left panels in the particular figures. The reason is that the density is much higher therefore the RS must return to the origin sooner, compared to e.g. the results shown in Figure 6.6 and is therefore sensitive to the existence of such a cavity. Should the density be lower, one would expect even the RS not to be too sensitive to the existence of a cavity if this is sufficiently small. This aspect is illustrated next.

Figure 6.8 shows similar results to Figure 6.7, however, for the left panels the ISM density assumed was 10^{-24} g cm^{-3}, while for the right panels 10^{-22} g cm^{-3}. For all computations the ejecta mass was increased to M_{ej} = 12 $M_\odot$. For both the left and right panels, an artificial cavity

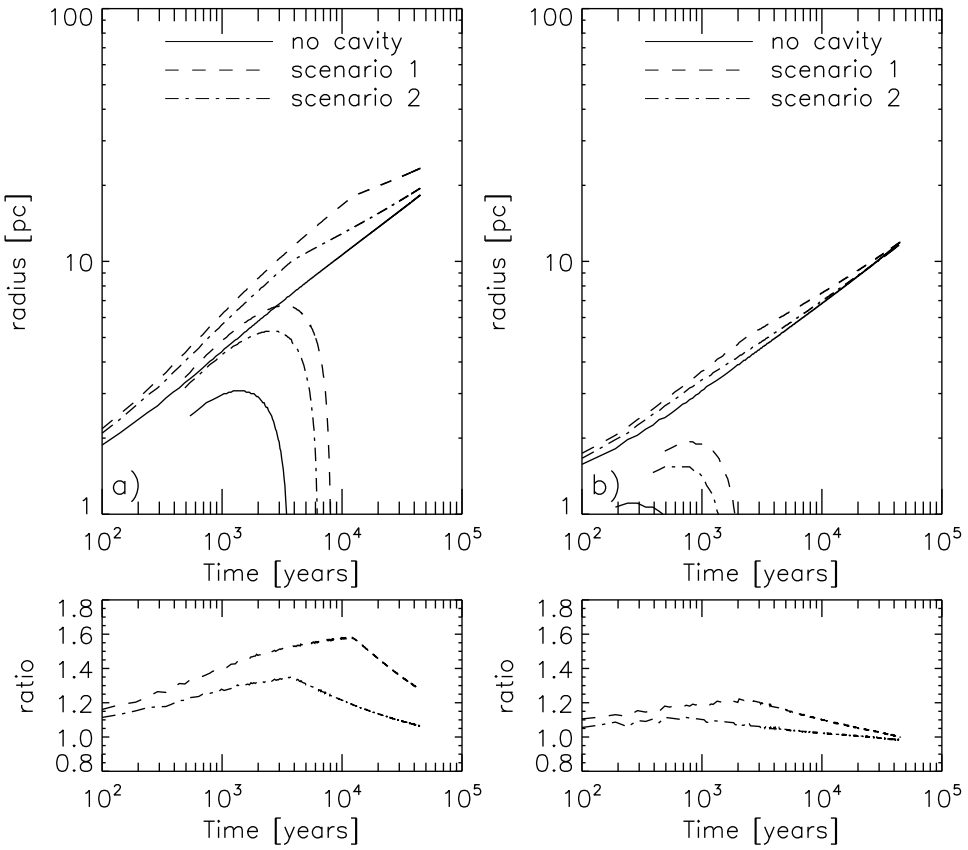

Figure 6.7: Similar to Figure 6.6 except results are shown corresponding to other stellar wind mass-loss rates and more dense ISM conditions. For the left panels the stellar wind with a mass loss rate 5×10^{-5} $M_\odot$ y^{-1} and outflow speeds of 3000 km s^{-1} and 2000 km s^{-1} are selected. For both these scenarios a cavity is blown in an ISM with density 10^{-23} g cm^{-3}. Scenario 1 corresponds again to the larger cavity this time $\sim$ 18 pc while scenario 2 corresponds to a cavity of $\sim$ 10 pc. Both these scenarios have a factor of $\sim$ 10 difference between the ISM and the post-shocked medium. For the right panels, the ISM density was increased to 10^{-22} g cm^{-3}. For these scenarios, artificial cavities were assumed. Scenario 1 corresponds to a cavity of 5 pc and with a density difference between the post-shocked medium and the undisturbed ISM of a factor of 3, while for scenario 2, the difference is a factor of 2 and the cavity size is 3 pc.

was assumed, the same as the right panel in Figure 6.7. Scenario 1 corresponds to a cavity of 5 pc and with a density difference between the post-shocked medium and the undisturbed ISM of a factor of 3, while for scenario 2 the difference is a factor of 2 and the cavity size is 3 pc.

Shown here in the left panels of Figure 6.8 is the sensitivity of both the RS and FS for the two cavity scenarios discussed above. From the left panels it follows that when the ISM density is decreased to 10^{-24} g cm^{-3} compared to 10^{-22} g cm^{-3} as in the right panel of Figure 6.7 it follows that both scenarios are insensitive to the existence of a cavity as an initial condition in the computations. Also, the ejecta mass was increased for these computations to M_{ej} = 12 $M_\odot$. All of this lead to an increase in the expected return time of the RS to the origin. This is in contrast to the scenarios in the right panel of Figure 6.7 where a much denser ISM and smaller M_{ej} were assumed. Therefore, we conclude that the effect of such a cavity on the evolution of an SNR also depends on the medium surrounding the original stellar wind.

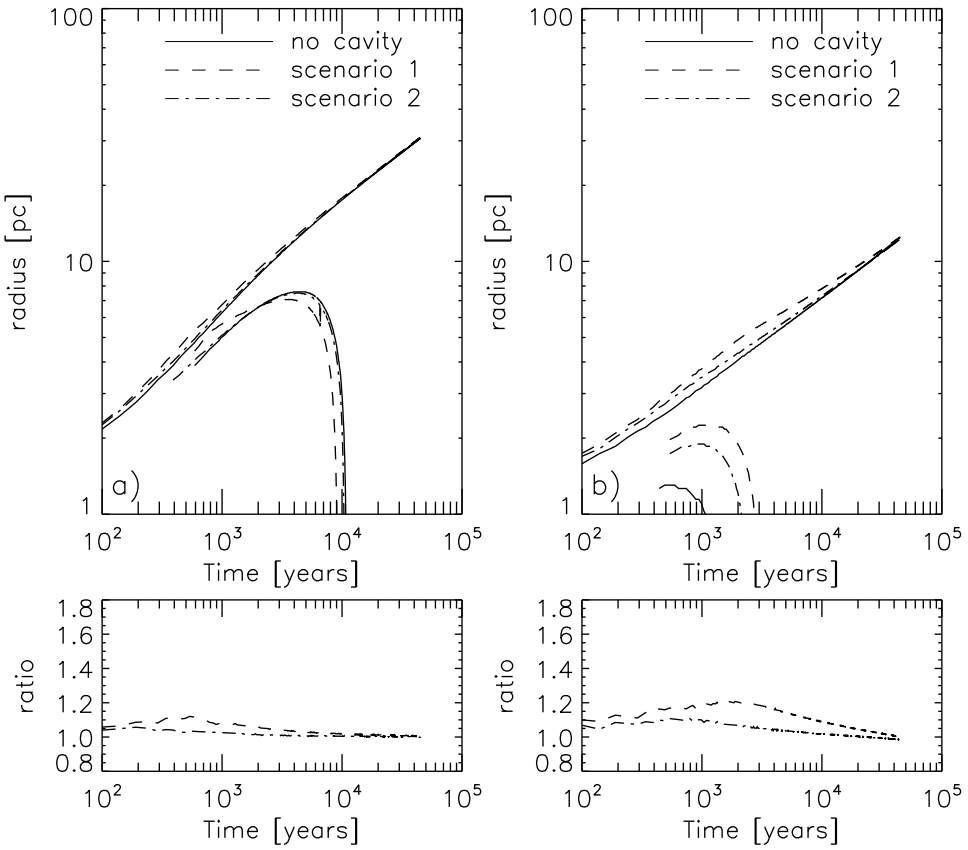

Figure 6.8: Similar to Figure 6.7. For the left panels the ISM density assumed was 10^{-24} g cm^{-3}, while for the right panels 10^{-22} g cm^{-3}. For all computations the ejecta mass was increased to M_{ej} = 12 $M_{\odot}$. For both the left and right panels an artificial cavity was assumed. Scenario 1 corresponds to a cavity of 5 pc and with a density difference between the post-shocked medium and the undisturbed ISM of a factor of 3, while for scenario 2 the difference is a factor of 2 and the cavity size is 3 pc.

The right panels in Figure 6.8 correspond exactly to the right panels in Figure 6.7, except here M_{ej} was increased from M_{ej} = 8 $M_{\odot}$ to M_{ej} = 12 $M_{\odot}$. By comparing these two it follows that increasing this parameter does not in any way change any of the conclusions made thus far.

6.5 Summary and conclusions

In this chapter, the evolution of supernova remnants (SNRs) in cavities blown out by different stellar winds into the ambient interstellar medium (ISM) was investigated. Firstly, a background was given and results of *Ferreira and de Jager* (2008), who studied the evolution of these SNR into the undisturbed ISM, were summarized. These authors investigated how the evolution of the SNR will be influenced by changing the parameters such as ejecta energy, E_{ej}, ejecta mass, M_{ej}, and interstellar medium density ρ_{ISM}. In particular, they concentrated on the forward shock (FS) and reverse shock (RS) radius of the SNR as a function of time. They derived an analytical expression giving the return time of the RS to the origin in terms of E_{ej}, M_{ej} and ρ_{ISM}. This time is very much dependent on both the ρ_{ISM} and the M_{ej} and decreases for both the cases of increasing the ρ_{ISM} and decreasing the M_{ej}. However, all of their studies assumed

the evolution of an SNR into the undisturbed ISM (e.g. no initial cavity due to a stellar wind).

In this chapter, this work was extended by taking into account the existence of a pre-existing stellar wind cavity. By assuming this as an initial condition in the model, SNR evolution simulations were done, and results were compared to the case where no pre-existing cavity was assumed. This was also done for a variety of M_{ej} and ρ_{ISM} values, which correspond to different cavity sizes. Of importance was to determine how the return time of the RS to the origin is influenced by the presence of such a cavity, and how the FS evolution is influenced by this cavity.

Shown in different figures in this chapter was that the evolution of an SNR is influenced by a cavity blown by a stellar wind even if this cavity is in the order of only a few pc. The FS of an SNR evolves faster into a lower density cavity compared to the case of evolution into the undisturbed ISM. These results were shown in Figure 6.2 (density), Figure 6.3 (pressure) and Figure 6.4 (speed). Also shown in Figure 6.5 was how the FS speed is influenced when it reaches the shocked stellar wind/undisturbed ISM interface. The speed of the FS decreases as it moves further and further into the undisturbed ISM, because energy is removed from the FS by means of a reflection wave/shock created at the interface.

Figure 6.6 showed how a cavity influences the evolution of the FS and RS. The blast wave (FS) initially evolves faster in the cavity, and is then decelerated at the boundary of the cavity (AP). This is not the case for the evolution into the undisturbed ISM. As for the RS, it takes longer to sweep up the same amount of material in a lower density cavity than in the undisturbed ISM and the return time to the origin is later.

We Conclude from Figure 6.6 to Figure 6.8, that the FS is not considerably influenced by the presence of a cavity if this cavity is not in the order of at least ~ 10 pc or larger. However, the RS is strongly influenced, even for smaller cavities. The reason is that the density for smaller cavities is much higher, therefore the RS must return to the origin sooner. Should the density be lower, one would expect that even the RS will not be too sensitive to the existence of a cavity if this is sufficiently small (e.g. smaller mass-loss rates).

Therefore, we conclude is that the effect of such a cavity on the evolution of an SNR also depends on the medium surrounding the original stellar wind. However, by keeping the conditions of the cavity and ISM the same and changing the M_{ej} do not change any of the conclusions.

Chapter 7

Summary and conclusions

This work started out with a brief introduction concerning the most well-known stellar wind (astrosphere), namely the heliosphere. A brief overview of the advances of state of the art models that are used to compute this structure was given. Also, results of *Snyman* (2007) were summarized where such a hydrodynamic model was utilized to compute the interaction between the solar wind and local interstellar medium (LISM). This model was applied and extended in this work to calculate the stellar wind evolution of O- and B-type stars.

In Chapter **2**, the main focus was to give a brief background on how and where massive stars are formed. Firstly, a discussion was given on the structure and parameters of the surrounding interstellar medium (ISM). This included a small-and large-scale view of the ISM. It was also showed how the structure of the ISM can be sculptured by the energy and kinematic input of supernova explosions. The density and temperature of the ISM were also discussed, and a description of the interstellar magnetic field found in these regions was also given.

Different kinds of molecular clouds and the structures that can be found inside them were also discussed in Chapter **2**. The conditions inside these clouds, such as density, temperature and their size were also mentioned. Star-formation inside these different clouds, occurring as a cluster of stars, a binary system or a single massive star was also briefly discussed. However, in this work an investigation into the evolution of a single massive star is of interest, because stellar wind evolution from these objects was simulated.

Therefore, an overview was also given in Chapter **2** on how single massive stars form from a hot molecular core (HMC). A proto-stellar object is formed due to gravitational instabilities, and accretes matter from the envelope surrounding it and in the process its mass increases. When the mass of the star reaches a value of ~ 15 $M_{\odot}$ its radiation is initiated. As it reaches the mass of ~ 20 $M_{\odot}$, the force that the radiation exerts on the stellar material becomes larger than the gravitational force, and the stellar material on the surface of the star cannot be held by the gravitational force anymore, and the stellar envelope must be accelerated outward.

In this work, stellar winds corresponding to different mass-loss rates and outflow speeds are calculated. For this purpose, a hydrodynamic model is utilized, which was discussed in Chap-

ter **3**. This model is based on the finite volume method and is fully discussed in e.g. *Snyman* (2007).

In Chapter **4**, stellar wind evolution of O- and B-type stars was simulated using the model discussed in Chapter **3**. Note that the model used in this work does not include the evolution of the stellar wind for the second (Red super giant, RSG) phase or the third (Wolf-Rayet, WR) phase (see e.g. section 2.4). This means that the results obtained from this model can only be used to discuss the state of the stellar wind cavity evolution up to the end of the main-sequence evolution. This depends on the mass and mass-loss rate of the star and could be $\sim$ 1-10 My, which is at the end of the simulation times presented in this work. For longer simulation times these other two phases need to be taken into account.

To establish if this model results in calculations compatible with other stellar models, a comparison was made between results obtained by this model and those calculated by a different model from *Arthur* (2007) as shown in Figure 4.1. Comparing results to Figure 4.1, it was found that for almost a similar set of parameters, the profile shown by the red solid line in Figure 4.12 is comparable to that of Figure 4.1. By extrapolating the AP radius of the red solid line in Figure 4.12 to a time period of (4×10^6 y), it was found that there is a $\sim$ 10 % difference between this model and the results of *Arthur* (2007) for a similar set of parameters.

The main aim of Chapter **4** was to calculate and present the AP and TS distances as a function of time for different outflow speeds, mass-loss rates and ISM densities. Summarizing Figures 4.7 to 4.13 it follows that if the AP radius of a stellar wind with a speed of 2000 km s^{-1} was compared to the AP radius of a stellar wind with a speed of 1000 km s^{-1} (having the same ISM density and mass-loss rate), the result was that the AP radius for the 1000 km s^{-1} wind scenario is $\sim$ 50% of that of the 2000 km s^{-1} wind scenario after a simulation time of 1 My. If the same was done for 3000 km s^{-1} and 1000 km s^{-1} stellar wind scenarios, the result was that the AP radius for the 1000 km s^{-1} stellar wind is $\sim$ 33% of that of the 3000 km s^{-1} wind after 1 My. Doing the same with the 2000 km s^{-1} and 3000 km s^{-1} scenarios, the AP radius of the 2000 km s^{-1} stellar wind is $\sim$ 66% of that of the AP radius corresponding to a 3000 km s^{-1} stellar wind after 1 My. This was the case for all the different mass-loss rates and ISM densities considered and after a simulation time of 1 My.

The same study was done by varying the stellar mass-loss rate. Comparing the computed AP radius corresponding to a stellar mass-loss rate of 10^{-6} $M_\odot$ y^{-1} to that of a stellar mass-loss rate of 5×10^{-6} $M_\odot$ y^{-1}, it followed that the AP radius corresponding to a stellar mass-loss rate of 10^{-6} $M_\odot$ y^{-1} is $\sim$ 60% of that of the AP for a stellar mass-loss rate of 5×10^{-6} $M_\odot$ y^{-1}. Comparing a mass-loss rate scenario of 5×10^{-6} $M_\odot$ y^{-1} to that of 10^{-5} $M_\odot$ y^{-1}, it followed that the AP radius of the stellar mass-loss rate of 5×10^{-6} $M_\odot$ y^{-1} is $\sim$ 78% that of the AP radius for a stellar mass-loss rate of 10^{-5} $M_\odot$ y^{-1}. The AP radius for a stellar mass-loss rate of 10^{-6} $M_\odot$ y^{-1} is $\sim$ 46% that of a stellar mass-loss rate of 10^{-5} $M_\odot$ y^{-1}. This is the case for all parameter combinations considered in this work and after a simulation time of 1 My.

For the case of the stellar wind evolving into a denser region in the ISM (e.g. molecular clouds), this investigation shows that by keeping the ambient density fixed at $\rho_{ISM} = 10^{-22}$ g cm^{-3}, and changing the stellar wind speed from 2000 km s^{-1} to 3000 km s^{-1}, the AP radius for a stellar wind speed of 2000 km s^{-1} is $\sim$ 66% compared to the AP radius for a stellar wind speed of 3000 km s^{-1}, for both mass-loss rates investigated. However, for $\rho_{ISM} = 10^{-21}$ g cm^{-3}, the AP radius for a stellar wind speed of 2000 km s^{-1} is $\sim$ 40% compared to the AP radius for a stellar wind speed of 3000 km s^{-1}, again for both mass-loss rates investigated. Secondly, by keeping the mass-loss rate fixed at 10^{-5} M$_{\odot}$ y^{-1} and changing the ambient density from $\rho_{ISM} = 10^{-22}$ g cm^{-3} to $\rho_{ISM} = 10^{-21}$ g cm^{-3}, the AP radius for $\rho_{ISM} = 10^{-21}$ g cm^{-3} is $\sim$ 50% compared to the AP radius for $\rho_{ISM} = 10^{-22}$ g cm^{-3}, for a stellar wind speed of 3000 km s^{-1}. For a stellar wind speed of 2000 km s^{-1}, the AP radius for $\rho_{ISM} = 10^{-21}$ g cm^{-3} is $\sim$ 33% compared to the AP radius for $\rho_{ISM} = 10^{-22}$ g cm^{-3}, when the density is decreased. For a mass-loss rate of 5 $\times$ 10^{-6} M$_{\odot}$ y^{-1}, the AP radius for $\rho_{ISM} = 10^{-21}$ g cm^{-3} is $\sim$ 20% compared to the AP radius for $\rho_{ISM} = 10^{-22}$ g cm^{-3}, for a stellar wind of 2000 km s^{-1}. Whereas for a stellar wind of 3000 km s^{-1} the AP radius for $\rho_{ISM} = 10^{-21}$ g cm^{-3} is $\sim$ 33% compared to the AP radius for $\rho_{ISM} = 10^{-22}$ g cm^{-3}. These results were for both simulation times considered.

In Chapter **5**, the main focus was to establish to what extent the relative motion between the stellar wind and ISM has an effect on the structure of the cavity blown by its stellar wind. Again, both the cases of evolution into the ambient medium and into a molecular cloud were considered. The results showed that as the relative speed was increased, the stellar wind cavity (AP radius) becomes smaller in the nose direction and larger in the tail direction, the nose direction being the direction opposite to the flow of the ISM material and the tail being along the flow of the ISM material.

For a relatively low relative speed of 25 km s^{-1}, the ratio of the AP between the nose and the tail was $\sim$ 1.4 for all the scenarios considered. For an assumed relative speed of 100 km s^{-1} in the model, the ratio of the AP between the nose and tail was between $\sim$ 1.6 and 2.0, while for an assumed relative speed of 250 km s^{-1}, the ratio of the AP between the nose and tail was between $\sim$ 4.0 and $\sim$ 5.0, depending on parameters like ISM density and mass-loss rate.

From Figures 5.4 to 5.7 and Figure 5.8 to Figure 5.11 it can be summarized that for all mass-loss rates and ρ_{ISM} values the following is applicable: The AP radius in the nose direction for a stellar wind with a relative speed of 25 km s^{-1} was $\sim$ 90% compared to the AP radius of a stellar wind with no relative speed. For a stellar wind with a relative speed of 100 km s^{-1} it was $\sim$ 70% compared to a stellar wind with no relative speed, and lastly the AP radius of a stellar wind with a relative speed of 250 km s^{-1} was $\sim$ 25% compared to the AP radius of a stellar wind with no relative speed.

In Chapter **6**, the evolution of supernova remnants (SNRs) in cavities blown out by different stellar winds into the ambient interstellar medium (ISM) was investigated. Firstly, a background was given and results of *Ferreira and de Jager* (2008), who studied the evolution of these SNR into the undisturbed ISM, were summarized. These authors investigated how the evo-

lution of the SNR is influenced by changing the parameters such as ejecta energy, E_{ej}, ejecta mass, M_{ej}, and interstellar medium density ρ_{ISM}. In particular, they concentrated on the forward shock (FS) and reverse shock (RS) radius of the SNR as a function of time. They derived an analytical expression giving the return time of the RS to the origin in terms of E_{ej}, M_{ej} and ρ_{ISM}. However, for all of their studies they assumed the evolution of an SNR into the undisturbed ISM (e.g. no initial cavity due to a stellar wind).

In this chapter, their work was extended by taking into account the existence of a pre-existing stellar wind cavity. By assuming this as an initial condition in the model, SNR evolution simulations were done and results compared to the case where no pre-existing cavity was assumed. This was also done for a variety of M_{ej} and ρ_{ISM} values, which corresponded to different cavity sizes. Of importance was to determine how the return time of the RS to the origin is influenced by the presence of such a cavity, and how the FS evolution is influenced by this cavity.

Shown in Chapter **6** was that the evolution of an SNR is influenced by a cavity blown by a stellar wind even if this cavity is in the order of a few pc compared to the case where no cavity is assumed. The FS of an SNR evolves faster into a lower density cavity compared to the case of evolution into the undisturbed ISM. Although the FS initially evolves faster in the cavity, it is later decelerated at the boundary of the cavity (AP). This is not the case for the evolution into the undisturbed ISM. As for the RS, it takes longer to sweep up the same amount of material in a lower density cavity than in the undisturbed ISM and the return time to the origin is later.

Our conclusion was that the FS is not considerably influenced by the presence of a cavity if this cavity is not in the order of at least ~ 10 pc or larger. However, the RS is strongly influenced, even for smaller cavities. The reason is that the density for smaller cavities is much higher, therefore the RS must return to the origin sooner. Should the density be lower one would expect that even the RS is not too sensitive to the existence of a cavity if this is sufficiently small (e.g. smaller mass-loss rates).

Therefore, we conclude that the effect of such a cavity on the evolution of an SNR also depends on the medium surrounding the original stellar wind. However, by keeping the conditions of the cavity and ISM the same and changing the M_{ej} do not change any of the conclusions.

Bibliography

Ardavan, H., Dynamical Evolution of an Expanding Gas Cloud, *Astrophysical Journal*, *184*, 435, 1973.

Arthur, S. J., Wind-Blown Bubbles and HII Regions around Massive Stars, in *Revista Mexicana de Astronomia y Astrofisica Conference Series*, *Revista Mexicana de Astronomia y Astrofisica Conference Series*, vol. 30, p. 64, 2007.

Axford, W. I., A. J. Dessler, and B. Gottlieb, Termination of Solar Wind and Solar Magnetic Field., *Astrophysical Journal*, *137*, 1268, 1963.

Axford, W. I., E. Leer, and G. Skadron, The acceleration of cosmic rays by shock waves, in *International Cosmic Ray Conference*, *International Cosmic Ray Conference*, vol. 11, p. 132, 1977.

Ball, B., M. Zhang, H. Rassoul, and T. Linde, Galactic Cosmic-Ray Modulation Using a Solar Minimum MHD Heliosphere: A Stochastic Particle Approach, *Astrophysical Journal*, *634*, 1116, 2005.

Baranov, V. B., and Y. G. Malama, Model of the solar wind interaction with the local interstellar medium - Numerical solution of self-consistent problem, *Journal for Geophysical Research*, *98*, 15,157, 1993.

Beck, R., Interstellar magnetic fields, *IEEE Transactions on Plasma Science*, *14*, 740–747, 1986.

Bell, A. R., The acceleration of cosmic rays in shock fronts. I, *Monthly notices of the Royal Astronomical Society*, *182*, 147, 1978a.

Bell, A. R., The acceleration of cosmic rays in shock fronts. II, *Monthly notices of the Royal Astronomical Society*, *182*, 443, 1978b.

Bernabeu, G., A. Magazzu, and R. Stalio, Stellar wind velocities and luminosities of O stars, *Astronomy and Astrophysics*, *226*, 215, 1989.

Beuermann, K., G. Kanbach, and E. M. Berkhuijsen, Radio structure of the Galaxy - Thick disk and thin disk at 408 MHz, *Astronomy and Astrophysics*, *153*, 17, 1985.

Biermann, L., Kometenschweife und solare Korpuskularstrahlung, *Zeitschrift für Astrophysik*, *29*, 274, 1951.

Blandford, R. D., and J. P. Ostriker, Particle acceleration by astrophysical shocks, *Astrophysical Journal letters*, *221*, L29, 1978.

Blitz, L., Star Forming Giant Molecular Clouds, in *NATO ASIC Proc. 342: The Physics of Star Formation and Early Stellar Evolution*, edited by C. J. Lada & N. D. Kylafis, p. 3, 1991.

Blitz, L., and J. P. Williams, Molecular Clouds, in *NATO ASIC Proc. 540: The Origin of Stars and Planetary Systems*, edited by C. J. Lada & N. D. Kylafis, p. 3, 1999.

Blondin, J. M., and D. C. Ellison, Rayleigh-Taylor Instabilities in Young Supernova Remnants Undergoing Efficient Particle Acceleration, *Astrophysical Journal*, *560*, 244, 2001.

Blondin, J. M., R. A. Chevalier, and D. M. Frierson, Pulsar Wind Nebulae in Evolved Supernova Remnants, *Astrophysical Journal*, *563*, 806, 2001.

Böhm-Vitense, E., *Introduction to stellar astrophysics Volume 2: Stellar Atmospheres*, Cambridge University Press, 1989.

Borrmann, T., and H. Fichtner, On the dynamics of the heliosphere on intermediate and long time-scales, *Advances in Space Research*, *35*, 2091, 2005.

Bowers, R., and T. Deeming, *Astrophysics I: Stars*, Jones and Bartlett Publishers, INC. Boston, 1984.

Bucciantini, N., J. M. Blondin, L. Del Zanna, and E. Amato, Spherically symmetric relativistic MHD simulations of pulsar wind nebulae in supernova remnants, *Astronomy and Astrophysics*, *405*, 617, 2003.

Carroll, B. W., and D. A. Ostlie, *An introduction to modern astrophysics and cosmology, 2nd edn.*, San Francisco: Addison-Westley, 2007.

Cassinelli, J. P., Stellar winds, *Annual reviews of Astronomy and Astrophysics*, *17*, 275, 1979.

Chiosi, C., and E. Nasi, Mass loss from early type stars, *Astronomy and Astrophysics*, *34*, 355, 1974.

Cioffi, D. F., C. F. McKee, and E. Bertschinger, Dynamics of radiative supernova remnants, *Astrophysical Journal*, *334*, 252, 1988.

Davis, L., Jr., and J. L. Greenstein, The Polarization of Starlight by Aligned Dust Grains., *Astrophysical Journal*, *114*, 206, 1951.

de Loore, C., J. P. de Greve, and H. J. G. L. M. Lamers, Evolution of massive stars with mass loss by stellar wind, *Astronomy and Astrophysics*, *61*, 251, 1977.

De Villiers, H., A Near-Infrared study of the southern high mass star forming region RCW 34, Master's thesis, North-West University, Potchefstroom Campus, South Africa, 2009.

Decourchelle, A., D. C. Ellison, and J. Ballet, Thermal X-Ray Emission and Cosmic-Ray Production in Young Supernova Remnants, *Astrophysical Journal letters*, *543*, L57, 2000.

Del Zanna, L., E. Amato, and N. Bucciantini, Axially symmetric relativistic MHD simulations of Pulsar Wind Nebulae in Supernova Remnants. On the origin of torus and jet-like features, *Astronomy and Astrophysics*, *421*, 1063, 2004.

Dohm-Palmer, R. C., and T. W. Jones, Young Supernova Remnants in Nonuniform Media, *Astrophysical Journal*, *471*, 279, 1996.

Dwarkadas, V. V., and R. A. Chevalier, Interaction of Type IA Supernovae with Their Surroundings, *Astrophysical Journal*, *497*, 807, 1998.

Ellison, D. C., A. Decourchelle, and J. Ballet, Hydrodynamic simulation of supernova remnants including efficient particle acceleration, *Astronomy and Astrophysics*, *413*, 189, 2004.

Fahr, H.-J., T. Kausch, and H. Scherer, A 5-fluid hydrodynamic approach to model the solar system-interstellar medium interaction, *Astronomy and Astrophysics*, *357*, 268, 2000.

Falle, S. A. E. G., A numerical calculation of the effect of stellar winds on the interstellar medium, *Astronomy and Astrophysics*, *43*, 323, 1975.

Ferreira, S. E. S., and O. C. de Jager, Supernova remnant evolution in uniform and non-uniform media, *Astronomy and Astrophysics*, *478*, 17, 2008.

Ferreira, S. E. S., and K. Scherer, Modulation of Cosmic-Ray Electrons in the Outer Heliosphere, *Astrophysical Journal*, *616*, 1215, 2004.

Ferreira, S. E. S., and K. Scherer, Time Evolution of Galactic and Anomalous Cosmic-Ray Spectra in a Dynamic Heliosphere, *Astrophysical Journal*, *642*, 1256, 2006.

Ferreira, S. E. S., M. S. Potgieter, and K. Scherer, Modeling of the Heliospheric Interface, Magnetic Field, and Cosmic-Ray Transport, *Astrophysical Journal*, *659*, 1777, 2007a.

Ferreira, S. E. S., M. S. Potgieter, and K. Scherer, Transport and acceleration of anomalous cosmic rays in the inner heliosheath, *Journal of Geophysical Research (Space Physics)*, *112*, 101, 2007b.

Ferrière, K. M., The interstellar environment of our galaxy, *Reviews of Modern Physics*, *73*, 1031, 2001.

Florinski, V., and J. R. Jokipii, Cosmic-Ray Spectra at Spherical Termination Shocks, *Astrophysical Journal*, *591*, 454, 2003.

Florinski, V., G. P. Zank, and N. V. Pogorelov, Galactic cosmic ray transport in the global heliosphere, *Journal of Geophysical Research (Space Physics)*, *108*, 1228, 2003.

Frisch, P. C., The Local Bubble and Interstellar Material Near the Sun, *Space Science Reviews*, *130*, 355, 2007.

Garcia-Segura, G., N. Langer, and M. Mac Low, The hydrodynamic evolution of circumstellar gas around massive stars. II. The impact of the time sequence O star– RSG – WR star., *Astronomy and Astrophysics*, *316*, 133, 1996a.

Garcia-Segura, G., M. Mac Low, and N. Langer, The dynamical evolution of circumstellar gas around massive stars. I. The impact of the time sequence Ostar – LBV – WR star., *Astronomy and Astrophysics*, *305*, 229, 1996b.

Georgelin, Y. M., and Y. P. Georgelin, The spiral structure of our Galaxy determined from H II regions, *Astronomy and Astrophysics*, *49*, 57, 1976.

Ghez, A. M., M. Morris, and E. E. Becklin, High Proper Motion Stars in the Vicinity of SGR A*: Evidence for a Supermassive Black Hole at the Center of Our Galaxy, in *The Central Parsecs of the Galaxy*, *Astronomical Society of the Pacific Conference Series*, vol. 186, edited by H. Falcke, A. Cotera, W. J. Duschl, F. Melia, and M. J. Rieke, p. 18, 1999.

González-Avilés, M., S. Lizano, and A. C. Raga, Evolution of H II Regions inside Hot Molecular Cores, *Astrophysical Journal*, *621*, 359, 2005.

Hall, J. S., Observations of the Polarized Light from Stars, *Science*, *109*, 166, 1949.

Heiles, C., The Local Direction and Curvature of the Galactic Magnetic Field Derived from Starlight Polarization, *The Astrophysical Journal*, *462*, 316, 1996.

Ho, P. T. P., and A. D. Haschick, Formation of OB clusters - VLA observations, *Astrophysical Journal*, *248*, 622, 1981.

Hoare, M. G., S. E. Kurtz, S. Lizano, E. Keto, and P. Hofner, Ultracompact Hii Regions and the Early Lives of Massive Stars, *Protostars and Planets V*, p. 181, 2007.

Holzer, T. E., Interaction of the solar wind with the neutral component of the interstellar gas., *Journal of Geophysical Research (Space Physics)*, *77*, 5407, 1972.

Holzer, T. E., Interaction between the solar wind and the interstellar medium, *Annual Review of Astronomy and Astrophysics*, *27*, 199, 1989.

Holzer, T. E., and W. I. Axford, The Theory of Stellar Winds and Related Flows, *Annual review of Astronomy and Astrophysics*, *8*, 31, 1970.

Izmodenov, V. V., Modulation of galactic cosmic rays in the region of interaction of the local interstellar medium with the solar wind: Hydrodynamic approximation, *Astronomy Letters*, *23*, 221, 1997.

Kausch, T., Ein hydrodynamisches Mehrkomponentenmodell zur Beschreibung der Wechselwirkung zwischen Heliosphäre und interstellarem Medium, Ph.D. thesis, Rheinischen Friedrich-Wilhelms-Universität Bonn, 1998.

Kim, K., and B. Koo, Radio Continuum and Recombination line study of Ultra Compact H II Regions with extended envelopes, *Astrophysical Journal*, *549*, 979, 2001.

Klessen, R. S., T. Peters, R. Banerjee, M. Mac Low, R. Galvan-Madrid, and E. R. Keto, Modeling High-Mass Star Formation and Ultracompact HII Regions, *ArXiv e-prints*, 2010.

Kratter, K. M., C. D. Matzner, and M. R. Krumholz, Global Models for the Evolution of Embedded, Accreting Protostellar Disks, *Astrophysical Journal*, *681*, 375, 2008.

Krieger, A. S., A. F. Timothy, and E. C. Roelof, A Coronal Hole and Its Identification as the Source of a High Velocity Solar Wind Stream, *Solar Physics*, *29*, 505, 1973.

Krumholz, M. R., and C. D. Matzner, The Dynamics of Radiation-pressure-dominated H II Regions, *Astrophysical Journal*, *703*, 1352, 2009.

Krumholz, M. R., R. I. Klein, C. F. McKee, S. S. R. Offner, and A. J. Cunningham, The Formation of Massive Star Systems by Accretion, *Science*, *323*, 754, 2009.

Lada, C. J., and E. A. Lada, Embedded Clusters in Molecular Clouds, *Annual Reviews of Astronomy and Astrophysics*, *41*, 57, 2003.

Lada, C. J., N. D. Kylafis, and C. J. Lada & N. D. Kylafis (Eds.), *The origin of stars and planetary systems*, 1998.

Langner, U. W., and M. S. Potgieter, Effects of the position of the solar wind termination shock and the heliopause on the heliospheric modulation of cosmic rays, *Advances in Space Research*, *35*, 2084, 2005.

Lequeux, F. E., J., and C. Ryter, *The Interstellar Medium*, Springer Berlin Heidelberg: NY. A&A library., 2005.

LeVeque, R., *Finite Volume Methods for Hyperbolic Problems*, Cambridge University Press, 2002.

Lopez, L. A., M. R. Krumholz, A. D. Bolatto, J. X. Prochaska, and E. Ramirez-Ruiz, What Drives the Expansion of Giant HII Regions?: A Study of Stellar Feedback in 30 Doradus, *ArXiv e-prints*, 2010.

Lozinskaya, T. A., Ring nebulae associated with Of stars - Statistics, classification, origin, *Astrophysics and Space Science*, *87*, 313, 1982.

Marsch, E., *Physics of the Inner Heliosphere II*, chap. Kinetic Physics of the Solar Wind Plasma, p. 45, Springerlink, Berlin, 1991.

Mathewson, D. S., and V. L. Ford, Polarization observations of 1800 stars, *Mem. R. Astron. Soc.*, *74*, 139, 1970.

McComas, D. J., H. A. Elliott, J. T. Gosling, and R. M. Skoug, Ulysses observations of very different heliospheric structure during the declining phase of solar activity cycle 23, *Geophysical Research letters*, *33*, L09,102, 2006.

McComas, D. J., et al., Solar wind observations over Ulysses' first full polar orbit, *Journal for Geophysical Research*, *105*, 419, 2000.

McKee, C. F., X-Ray Emission from an Inward-Propagating Shock in Young Supernova Remnants, *Astrophysical Journal*, *188*, 335, 1974.

McKee, C. F., and J. P. Ostriker, A theory of the interstellar medium - Three components regulated by supernova explosions in an inhomogeneous substrate, *Astrophysical Journal*, *218*, 148, 1977.

McKee, C. F., and J. K. Truelove, Explosions in the interstellar medium., *Physics Reports*, *256*, 157, 1995.

Men, H., K. Ferrière, and J. L. Han, Observational constraints on models for the interstellar magnetic field in the Galactic disk, *Astronomy and Astrophysics*, *486*, 819–828, 2008.

Mihalas, D., *Stellar atmospheres, 2nd edn.*, Freeman, W.H. & Co, 1978.

Müller, H., P. C. Frisch, V. Florinski, and G. P. Zank, Heliospheric Response to Different Possible Interstellar Environments, *Astrophysical Journal*, *647*, 1491, 2006.

Myers, P. C., A compilation of interstellar gas properties, *Astrophysical Journal*, *225*, 380, 1978.

Nomura, H., and T. J. Millar, The physical and chemical structure of hot molecular cores, *Astronomy and Astrophysics*, *414*, 409, 2004.

Oey, M. S., and P. Massey, O star giant bubbles in M33, *Astrophysical Journal*, *425*, 635, 1994.

Opher, M., E. C. Stone, and P. C. Liewer, The Effects of a Local Interstellar Magnetic Field on Voyager 1 and 2 Observations, *Astrophysical Journal letters*, *640*, L71, 2006.

Osorio, M., S. Lizano, and P. D'Alessio, Hot Molecular Cores and the Formation of Massive Stars, *Astrophysical Journal*, *525*, 808, 1999.

Parker, E. N., The Stellar-Wind Regions., *Astrophysical Journal*, *134*, 20, 1961.

Pauls, H. L., and G. P. Zank, Interaction of a nonuniform solar wind with the local interstellar medium, *Journal of Geophysical Research*, *101*, 81, 1996.

Pauls, H. L., and G. P. Zank, Interaction of a nonuniform solar wind with the local interstellar medium 2. A two-fluid model, *Journal of Geophysical Research*, *102*, 19,779, 1997.

Pauls, H. L., G. P. Zank, and L. L. Williams, Interaction of the solar wind with the local interstellar medium, *Journal of Geophysical Research*, *100*, 595, 1995.

Pirronello, V., G. Manicò, E. Congiu, G. Vidali, A. Insolia, and R. Caruso, The Galactic Interstellar Medium: an Overview, *Nuclear Physics B Proceedings Supplements*, *165*, 87, 2007.

Pogorelov, N. V., G. P. Zank, and T. Ogino, Three-dimensional Features of the Outer Heliosphere Due to Coupling between the Interstellar and Interplanetary Magnetic Fields. I. Magnetohydrodynamic Model: Interstellar Perspective, *Astrophysical Journal*, *614*, 1007, 2004.

Pogorelov, N. V., G. P. Zank, and T. Ogino, Three-dimensional Features of the Outer Heliosphere due to Coupling between the Interstellar and Interplanetary Magnetic Fields. II. The Presence of Neutral Hydrogen Atoms, *Astrophysical Journal*, *644*, 1299, 2006.

Potgieter, M. S., and U. W. Langner, Modulation of cosmic rays: Perpendicular diffusion and drifts in a heliosphere with a solar wind termination shock, *Advances in Space Research*, *35*, 554, 2005.

Rand, R. J., and A. G. Lyne, New Rotation Measures of Distant Pulsars in the Inner Galaxy and Magnetic Field Reversals, *Monthly notices of the Royal Astronomical Society*, *268*, 497, 1994.

Richardson, J. D., J. C. Kasper, C. Wang, J. W. Belcher, and A. J. Lazarus, Cool heliosheath plasma and deceleration of the upstream solar wind at the termination shock, *Nature*, *454*, 63, 2008.

Scherer, K., and H.-J. Fahr, Remote diagnostic of the solar-cycle-induced heliospheric interface variation using energetic neutral atoms, *Astronomy and Astrophysics*, *404*, L47, 2003.

Scherer, K., and S. E. S. Ferreira, A heliospheric hybrid model: hydrodynamic plasma flow and kinetic cosmic ray transport, *Astrophysics and Space Sciences Transactions*, *1*, 17, 2005.

Schwenn, R., The average solar wind in the inner heliosphere: Structures and slow variations, in *NASA Conference Publication*, *NASA Conference Publication*, vol. 228, p. 489, 1983.

Sedov, L. I., *Similarity and Dimensional Methods in Mechanics*, New York: Academic Press, 1959.

Snyman, J., Modelling the Heliosphere and cosmic ray transport, Master's thesis, North-West University, Potchefstroom Campus, South Africa, 2007.

Stone, E., Voyager 2 Observations of the Solar Wind Termination Shock and Heliosheath, in *37th COSPAR Scientific Assembly*, *COSPAR, Plenary Meeting*, vol. 37, p. 3046, 2008.

Stone, E. C., A. C. Cummings, F. B. McDonald, B. C. Heikkila, N. Lal, and W. R. Webber, Voyager 1 Explores the Termination Shock Region and the Heliosheath Beyond, *Science*, *309*, 2017, 2005.

Suess, S. T., The heliopause, *Reviews of Geophysics*, *28*, 97, 1990.

Tang, S., and Q. D. Wang, Supernova Blast Waves in Low-Density Hot Media: A Mechanism for Spatially Distributed Heating, *Astrophysical Journal*, *628*, 205, 2005.

Troland, T. H., and C. Heiles, Interstellar magnetic field strengths and gas densities Observational and theoretical perspectives, *Astrophysical Journal*, *301*, 339, 1986.

Truelove, J. K., and C. F. McKee, Evolution of Nonradiative Supernova Remnants, *Astrophysical Journal science*, *120*, 299, 1999.

van der Swaluw, E., A. Achterberg, Y. A. Gallant, and G. Tóth, Pulsar wind nebulae in supernova remnants. Spherically symmetric hydrodynamical simulations, *Atronomy and Astrophysics*, *380*, 309, 2001.

van der Tak, F. F. S., Hot Molecular Cores and High Mass Star Formation, in *Star Formation at High Angular Resolution*, *IAU Symposium*, vol. 221, edited by M. G. Burton, R. Jayawardhana, and T. L. Bourke, p. 59, 2004.

Verschuur, G. L., Measurements of Magnetic Fields in Interstellar Clouds of Neutral Hydrogen, *Astrophysical Journal*, *156*, 861, 1969.

Williams, J. P., L. Blitz, and C. F. McKee, The Structure and Evolution of Molecular Clouds: from Clumps to Cores to the IMF, *Protostars and Planets IV*, p. 97, 2000.

Woltjer, L., Supernova Remnants, *Annual Reviews of Astronomy and Astrophysics*, *10*, 129, 1972.

Zank, G. P., H. L. Pauls, L. L. Williams, and D. T. Hall, Interaction of the solar wind with the local interstellar medium: A multifluid approach, *Journal of Geophysical Research*, *101*, 21,639, 1996.

Zirker, J. B., Coronal holes and high-speed wind streams, *Reviews of Geophysics and Space Physics*, *15*, 257, 1977.

Chapter 8

Aknowledgements

I would like to thank the following persons and institutions for support:

- Prof. S. E. S. Ferreira, my supervisor, for his excellent guidance throughout this study. This included frequent research discussions regarding topics relevant, and not so relevant, to this study.
- Prof. O. C. de Jager and Prof. D.J. van der Walt, for useful discussions and handling an array of frequent questions.
- Mrs M. P. Sieberhagen for handling all my administrative queries.
- Friends and colleagues for useful informal research discussions.
- The National Research Foundation and the Unit for Space Physics, NWU, for financial and other support throughout my studies.
- My parents and soon to be parents-in-law for all their support.
- My fiancee, Elré, for her constant love, support and motivation.

Stefanus Petrus van den Heever
Unit for Space Physics, North-West University,
March 2011.